Volume 2, Issue 1, March 2022

CHEMICAL SYNTHESIS

Recent topics on circularly polarized luminescence generated by inorganic materials

Xinling Liu, Ren-Hua Jin*

Open Access
ISSN 2769-5247 (Online)

www.chesynjournal.com

EDITORIAL BOARD

GENERAL INFORMATION

About the Journal

Chemical Synthesis (*CS*) is an international peer-reviewed, open access, online journal. *Chemical Synthesis* is an open access peer-reviewed journal publishing original research involving all areas of the chemical sciences. The journal aims to be the premier resource of seminal and insightful research and showcases for researchers in both academia and industry, providing a platform of inspiration for the future of chemistry. *Chemical Synthesis* intends to serve as the preeminent international chemistry journal and has the ambition to be among the first choices of chemists for publication of their discoveries.

The scope of the journal focuses on the breadth of the chemical synthetic sciences, covering fields from synthetic methodologies, property studies by theoretical calculations or instrumental approaches at molecular and/or nano levels of the obtained products (materials) to the applications in catalysis, energy conversion and storage, biomedicals, pharmaceuticals, environment protection and remediation, etc.

Information for Authors

Manuscripts should be prepared in accordance with Author Instructions.
Please check www.chesynjournal.com/pages/view/author_instructions for details.
All manuscripts should be submitted online at https://oaemesas.com/login?JournalId=cs.

Copyright

Permissions

For information on how to request permissions to reproduce articles/information from this journal, please visit www.chesynjournal.com.

Disclaimer

The information and opinions presented in the journal reflect the views of the authors and not of the journal or its Editorial Board or the Publisher. Publication does not constitute endorsement by the journal. Neither the *CS* nor its publishers nor anyone else involved in creating, producing or delivering the *CS* or the materials contained therein, assumes any liability or responsibility for the accuracy, completeness, or usefulness of any information provided in the *CS*, nor shall they be liable for any direct, indirect, incidental, special, consequential or punitive damages arising out of the use of the *CS*. The *CS*, nor its publishers, nor any other party involved in the preparation of material contained in the *CS* represents or warrants that the information contained herein is in every respect accurate or complete, and they are not responsible for any errors or omissions or for the results obtained from the use of such material. Readers are encouraged to confirm the information contained herein with other sources.

Publisher

OAE Publishing Inc.
245 E Main Street st112, Alhambra, CA 91801, USA
Website: www.oaepublish.com

Contacts

E-mail: editorialoffice@chesynjournal.com
Website: www.chesynjournal.com

Chemical Synthesis

CONTENTS

Volume 2 / Issue 1 / March 2022

Lang *et al. Chem Synth* 2022;2:1
DOI: 10.20517/cs.2021.15

Chemical Synthesis

Review

Open Access

Check for updates

Molecular chemisorption: a new conceptual paradigm for hydrogen storage

Chengguang Lang[1], Yi Jia[1], Xuecheng Yan[1,*], Liuzhang Ouyang[2], Min Zhu[2], Xiangdong Yao[1,3]

[1]School of Environment and Science, Queensland Micro- and Nanotechnology Centre, Griffith University, Nathan Campus, Brisbane 4111, Australia.
[2]Key Lab of Guangdong Province for Advanced Energy Storage Materials, School of Materials Science and Engineering, South China University of Technology, Guangzhou 510641, Guangdong, China.
[3]State Key Laboratory of Inorganic Synthesis and Preparative Chemistry, College of Chemistry, Jilin University, Changchun 130012, Jilin, China.

Correspondence to: Dr. Xuecheng Yan, School of Environment and Science, Queensland Micro- and Nanotechnology Centre, Griffith University, 170 Kessels Road, Nathan Campus, Brisbane 4111, Australia. E-mail: x.yan@griffith.edu.au

How to cite this article: Lang C, Jia Y, Yan X, Ouyang L, Zhu M, Yao X. Molecular chemisorption: a new conceptual paradigm for hydrogen storage. *Chem Synth* 2022;2:1. https://dx.doi.org/10.20517/cs.2021.15

Received: 26 Oct 2021 **First Decision:** 9 Dec 2021 **Revised:** 20 Feb 2022 **Accepted:** 23 Feb 2022 **Published:** 7 Mar 2022

Academic Editors: Bao-Lian Su, Stephane Siffert **Copy Editor:** Xi-Jun Chen **Production Editor:** Xi-Jun Chen

Abstract

Developing efficient hydrogen storage materials and the corresponding methods is the key to successfully realizing the "hydrogen economy". The ideal hydrogen storage materials should be capable of reversibly ab-/desorbing hydrogen under mild temperatures with high hydrogen capacities. To achieve this target, the ideal enthalpy of adsorption is determined to be 15-50 kJ/mol for hydrogen storage. However, the current mainstream methods, including molecular physisorption and atomic chemisorption, possess either too high or too low enthalpy of hydrogen adsorption, which are not suitable for practical application. To this end, hydrogen storage via molecular chemisorption is perceived to regulate the adsorption enthalpy with intermediate binding energy between the molecular physisorption and atomic chemisorption, enabling the revisable hydrogen ad-/desorption possible under ambient temperatures. In this review, we will elaborate the molecular chemisorption as a new conceptual paradigm and materials design to advance future solid-state hydrogen storage.

Keywords: Molecular chemisorption, hydrogen storage, coordination structure, adsorption sites

BACKGROUND

Hydrogen storage plays a critical role in energy transformation from fossil fuels to green energy. To increase the competitiveness of hydrogen as an energy vector, and to unlock its potential as a form of energy storage to smooth intermittent renewable energy production as well as a means of decarbonizing sectors, the storage of hydrogen must be made more efficient, safer, and cheaper, which is essential for future energy security and economic development, whereas it is currently missing in the hydrogen energy supply chain.

Specifically, the hydrogen energy supply chain associated with the "hydrogen economy" is generally composed of hydrogen production, storage/conveyance, and utilization. Up to now, abundant hydrogen sources can be obtained by diverse manufacturing methods, such as hydrocarbon reforming, biomass process, and water splitting. Meanwhile, the mature fuel cell technologies make the commercial application of hydrogen readiness to end-users as well. However, as to hydrogen storage, no practical approach currently exists to fulfill the technical requirements of fuel cells. Firstly, in actual application, hydrogen-powered cars are expected to meet a driving range (> 500 km or 300 miles) on a single fill, which is comparable to conventional combustion cars[1]. This means that about 5-6 kg of hydrogen is required to be stored on-board. Moreover, on-board hydrogen storage is also constrained by safety, weight, efficiency, volume, and cost[2]. So far, despite decades of great efforts, the secure and efficient on-board hydrogen storage method is still the main shackle of converting the world into a "hydrogen economy"[3]. Theoretical innovations and technical breakthroughs are still required to develop secure and efficient hydrogen storage technologies.

DILEMMAS OF CURRENT HYDROGEN STORAGE AND NEW SOLUTION

Currently, the established techniques for hydrogen storage consist of three means: compression, cryogenics, and material-assisted hydrogen storage[4]. Compressing hydrogen into a high-pressure cylinder is a direct and effective method to improve the volumetric energy density of H_2. So far, high-pressure cylinders can be pressurized up to 700 bar. However, despite such high pressures, a 150 L storage tank is required to store 6 kg of hydrogen. Moreover, the fast-filling strategies are still immature[5]. Hydrogen storage via liquefaction can offer a higher volumetric density compared with compressed hydrogen storage. Nevertheless, due to the low boiling point of liquid hydrogen, liquefying hydrogen needs to be operated under very low temperatures, which will consume a large amount of energy. Therefore, hydrogen storage systems via cryogenic and high-pressure methods are technically and financially impracticable and nonideal.

Alternatively, material-assisted solid-state hydrogen storage methods are therefore developed, which can be categorized into physisorption and chemisorption, based on the intrinsic hydrogen adsorption fashions. Hydrogen storage materials via physisorption can achieve higher hydrogen storage capacity on the surface than the bulk concentration due to gas-solid interactions, enabling a high hydrogen storage content[5,6]. Moreover, physiosorbed hydrogen can be readily and reversibly rapid charging/discharging without decomposition of the solid. Basically, materials based on physisorption are dependent on pore size, pore volume, surface area and the hydrogen binding sites decorated in the porous materials. For example, Li *et al.*[7] prepared a polyacrylonitrile-based porous carbon material with its surface area surface up to 3049 m^2g^{-1}. The hydrogen adsorption capacity can be achieved as high as 10.14 wt% at 50 bar. Further, the authors proved that the H_2 adsorption capacity at high pressure is ascribed to supermicropore (0.7-2.0 nm), while the narrow and deep pores (< 0.7 nm) define the H_2 adsorption capacity significantly at atmospheric pressure.

Blankenship *et al.*[8] reported cellulose acetate-derived porous carbons which possess high surface area ($3800 m^2 \cdot g^{-1}$) and pore volume ($1.8 cm^3 \cdot g^{-1}$) that arise almost entirely (> 90%) from micropores. The hydrogen storage test indicated a gravimetric hydrogen uptake of 8.1 wt% at -196 °C and 20 bar. However, at room temperature, the carbons only exhibited 1.2 wt% hydrogen uptake at 30 bar. Obviously, in practical, physisorption-type materials are subject to harsh operating conditions (cryogenic -temperature) due to the weak Van der Walls force. As shown in Figure 1, for classical physisorption materials such as the representatives of carbon nanotube, zeolites, covalent organic frameworks, and classical metal-organic frameworks (MOFs)[9-12], their adsorption enthalpies are determined to be 4-10 kJ/mol, which can only stabilize desired hydrogen capacity under the cryogenic temperature. Room temperature will weaken the interaction between H_2 molecules and adsorbents, leading to a sharp decrease in hydrogen storage capacity. Stabilizing hydrogen via molecular physisorption at room temperature is still a big challenge. Attempts are also made to enhance the interactions to improve the room temperature stability, such as heteroatom (e.g., O) doped carbon-based materials[8]. The density functional theory study indicates that the doped heteroatoms can modify the electronic structures of substrates via the charge-transfer behavior. This modification to the electronic properties of adsorption sites will create extra dipole moments, thus increasing hydrogen uptake[13]. However, the reported improvement of adsorption enthalpy is limited, generally lower than 15 kJ/mol.

In contrast, atomic chemisorption materials, including metal hydrides and chemical hydrides, characteristically possess high thermodynamic stability under room temperature due to the strong bonding between dissociative H atoms and adsorbent atoms. For example, the bonding energy of MgH_2 is as large as 75 kJ/mol[14]. Undoutedly, the cleavage of Mg-H requires a high temperature to stimulate the reaction. It is reported that the decomposition of MgH_2 is initiated while the temperature is increased up to 300 °C. Such a high operating temperature is not suitable for proton exchange membrane fuel cells[11]. Moreover, MgH_2 also suffers from sluggish dynamics. Efforts are also devoted to regulating the thermodynamics of MgH_2, such as nanostructuring, alloying, metastable phase[15,16]. However, their hydrogen storage performance still cannot meet the practical demands. For example, Cao *et al.*[17] reported a $Mg_{85}In_5Al_5Ti_5$ alloy prepared by plasma milling. Compared with pure MgH_2, the measured dehydrogenation enthalpy of $Mg_{85}In_5A_{l5}Ti_5$ alloy decreases to 65.2 kJ/(mol·H_2). However, kinetic properties indicate that a high temperature (over 300 °C) is still required to achieve rapid dehydrogenation kinetics. Chemical hydrides, like $NaBH_4$ and NH_3BH_3, generally possess higher hydrogen capacity[18,19]. However, their drawbacks are severe. Taking $NaBH_4$ as an example, hydrogen release by the thermolysis of $NaBH_4$ is impractical due to the high thermodynamic stability, stepwise decomposition companied with impurity gases and poor dynamics. It reported that the decomposition temperature of $NaBH_4$ was determined to be higher than 500 °C[19-21]. Alternatively, employing hydrolysis as off-board hydrogen storage, $NaBH_4$ still suffers from non-recyclability and non-affordability issues, despite its high hydrogen capacity and controllable hydrogen release. According to the guidelines set by the United States Department of Energy (DOE) for onboard hydrogen storage, by the year 2025, the gravimetric and volumetric storage capacities should meet the target of 5.5 wt% and 40 g/L under near-ambient operation temperatures of -40 to 85 °C[22].

Obviously, neither molecular physisorption nor atomic chemisorption could meet the targets of DOE. The inherent issues of the two hydrogen storage methods are ascribed to the unsuitable adsorption enthalpies of hydrogen. The reported solutions are mainly focused on how to improve weak molecular physisorption, or to decrease the strong atomic chemisorption, so as to form moderate binding energy. However, none of the current materials can meet the practical application requirements. The ideal hydrogen storage materials are reversibly operated under mild temperatures with fast charging/discharging kinetics. In addition, according to the DOE target, the hydrogen storage materials should be capable of adsorbing at least 5.5 wt% of

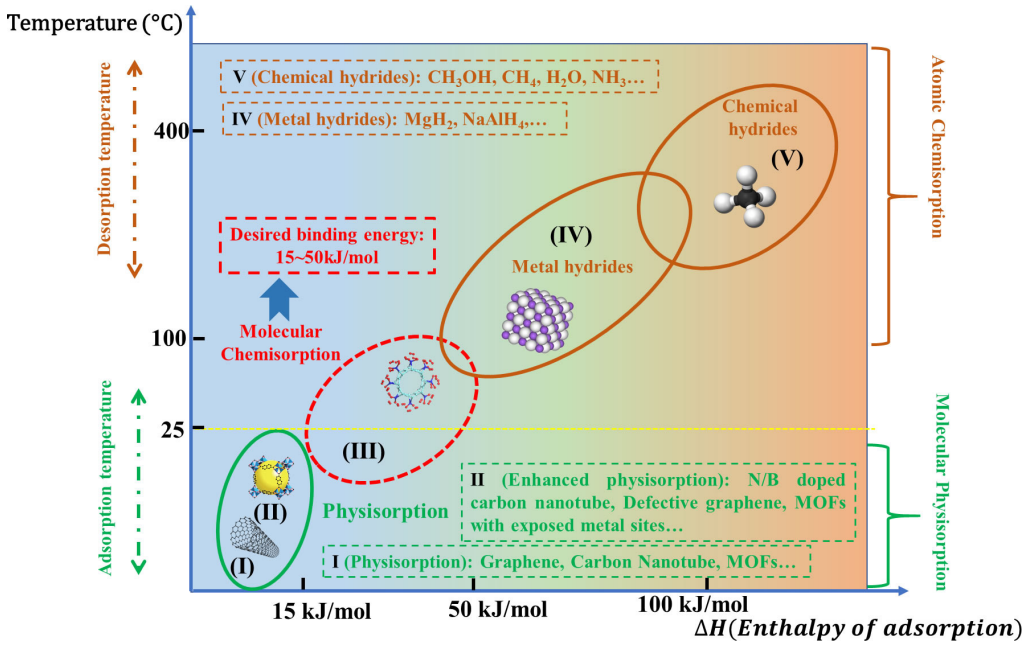

Figure 1. Hydrogen storage methods with respect to enthalpy of adsorption and operating temperature.

hydrogen. This means that hydrogen can be stored in molecular form, but in a weak chemisorption manner, called molecular chemisorption. This fascinating hydrogen storage method simultaneously endows materials the good reversibility as physical adsorption and moderate stability under room temperature as chemical adsorption, which may stand out as a promising hydrogen storage method.

THE MOLECULAR-CHEMISORPTION OF HYDROGEN

The molecular chemisorption process can be classified into weak chemisorption involving the gas-solid interactions on the surface. Hence, the structure of adsorption sites at the surface is vital to uncovering the underlying mechanism of molecular chemisorption, which is the prerequisite to both materials design and hydrogen adsorption behavior. Early in 1984, Kubas *et al.*[23] experimentally discovered a non-dissociative form of hydrogen adsorbed onto a coordinated transition metal (TM) complex, $W(CO)_3(P/Pr_3)_2$. In this TM complex, the W atom is linked with five coordinates, and the hydrogen molecule is chemisorbed without dissociation via side-on coordination binding to the W atom. However, the bond length of hydrogen is stretched by approximately 20% longer than that of free H_2. To explain the dihydrogen binding coordination, the Dewar-Chatt-Duncanson model for TM-olefin complexes[24] is invoked to rationalize the stability of these σ-type complexes, called Kubas-type interaction. Similar to the Dewar-Chatt-Duncanson model with a three-center two-electron (3c-2e) bond (type I shown in Figure 2), the Kubas-type interaction involves σ donation from the filled σ-bonding orbital of H_2 molecule to an unfilled d orbital of a TM. Meanwhile, π back-donation (BD) occurs from a filled d orbital of a TM to the empty σ* anti-bonding orbital of the H_2 molecule, which determines the stability of molecularly chemisorbed H_2 (type II shown in Figure 2).

The non-dissociative molecular chemisorption has ever been mentioned in metal-based hydrogen storage materials. It is known that the hydrogen sorption process upon metal atoms includes: physisorption, dissociation, hydrogen atom diffusion, hydride nucleation and growth. Note that the physisorbed H_2 will enter a molecular chemisorption state after crossing an activation barrier. The molecular chemisorption is generally considered a transition state before the dissociation of hydrogen. Mårtensson *et al.*[25] observed the

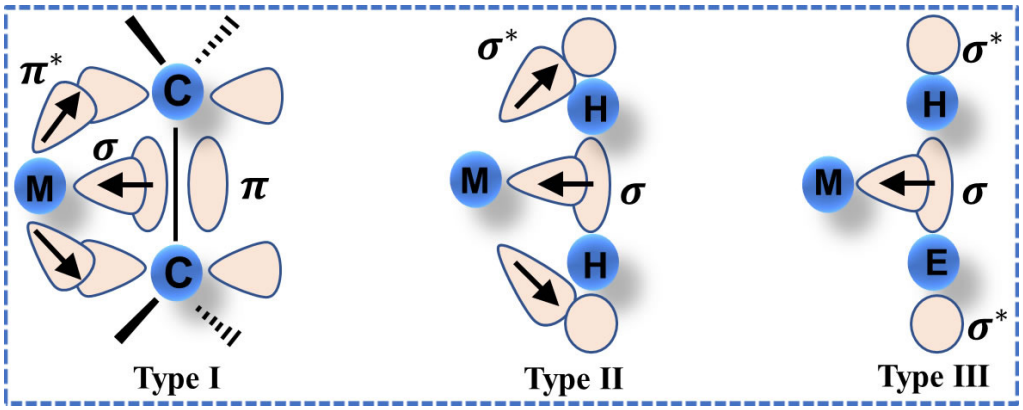

Figure 2. Schematic diagram showing three orbital interactions between the central element and ligand. Type I: TM-olefin complexes. Type II: Kubas-type H_2 complexes. Type III: η^2-σ complexes (E represents H, C, Si, *etc.*).

molecular H_2 chemisorbed at the edge sites of a stepped Ni (100) surface that is covered with a dense layer of atomic hydrogen by use of low-energy electron diffraction and electron energy-loss spectroscopy (EELS) in conjunction. In contrast, no such state is observed on the flat Ni (100) surface. The authors ascribed the molecular chemisorption to Kubas-type interaction. They suggested that nickel atoms with lower coordination at the stepped surface possess residual unfilled d states which could stabilize the chemisorbed H_2, while the dissociative channel is blocked by the saturated atomic adsorbate layer. The results illustrated that the low-coordinated metal atoms possess the capacity of molecular chemisorption.

Recently, Berwanger *et al.*[26] reported the direct observation of chemical binding forces on single Fe atoms to study the chemical reactivity of atom-assembled Fe clusters from 1 to 15 atoms at an atomic scale. This measurement can be achieved via scanning probe microscopy with CO-terminated tips, which can transition from the physisorption to the chemisorption regime and form a weak chemical bond with the individual atoms. It is found that the chemisorption strength increases inversely with the atom's reduced coordination number. The results imply that regulating atomic coordination numbers can enhance the interaction force between H_2 and adsorbent atoms.

The above analysis indicates that the low-coordinated metal atoms possess the capacity of molecular chemisorption. However, this does not mean that molecular chemisorption is Kubas action. According to Kubas interaction, it is the TM atom (owning d-orbital) with an unsaturated coordination state that can chemisorb H_2 in its molecular form. To some extent, Kubas-type interaction is reasonable, which explains the molecular chemisorption of H_2 and its stability, especially for TM atoms. However, the Kubas-type interaction is not a versatile theory or not the unique premise for molecular chemisorption in some cases. The first case is the MOFs with exposed metal sites (coordination-unsaturated). Naturally, MOFs with exposed metal sites possess uniformly distributed metal sites coordinated to organic linkers and sufficient porosity. It is reported that MOFs with exposed metal sites can significantly enhance the enthalpies of adsorption of H_2 compared to classical MOFs with saturated metal sites. For example, the FT-IR spectrometry studies indicate that H_2 can be adsorbed onto the coordinatively-unsaturated nickel (II) sites of MOF-74 with a strong adsorption enthalpy of 13.5 kJ·mol^{-1}[27]. In contrast, this elevated interaction of TM-H_2 is not found in classical MOFs with saturated TMs. However, the hydrogen adsorption mechanism for MOFs with exposed metal sites still involves physisorption that the hydrogen capacities are mostly rely on the surface area and total pore volume of the material, despite improved enthalpy of hydrogen adsorption. Zhou and Yildirim[28] individually investigate the role of exposed TM sites in MOFs by first-

principles calculations as well. Characteristics including charge transfer from TM to H_2, H_2-σ* Mn-d orbital hybridization, and H-H bond elongation, are not observed in the H_2-MOFs (with exposed TM sites) system, indicating that the enhanced heat of adsorption of H_2 is not related to the Kubas-type interaction. Furthermore, the authors reveal that the improved binding energy is contributed by the classical Coulomb interaction arising from the small charge overlap of H_2-σ and TM-d orbitals.

Another example is the adsorbent containing metals without d-electrons. As detailed in Kubas-type interaction, the adsorption site of transition metal should possess at least a vacant d orbit to accept the electrons from H_2 molecule as well as a filled d orbit to back-donate electrons to the anti-bonding orbit of H_2 molecule. Here, one may wonder whether they are capable of adsorbing intact H_2 molecules while the adsorption sites contain d_0 metals or high-oxidation-state main group elements that lack of electrons in the d orbital? According to Kubas, if there is a lack of BD, the Kubas-type H_2 complexes will be unstable. However, in recent research, Wang et al. indicate that metals lacking d orbital electrons still stably adsorb intact H_2 molecules, referred to as η^2-σ complexes in type-III [Figure 2][29]. These findings illustrate that supported alkali metals or alkaline earth metals (absence of d-electron), like Li- or Ca-modified carbon nanotube, possess the potential to be utilized for hydrogen storage. The results further indicate that the BD is not the crucial factor for the stabilization of molecularly chemisorbed H_2.

Furthermore, a strong polarization effect of low-valent TM on hydrogen adsorption is also significant. Based on self-consistent-field molecular-orbital theory, Niu *et al.*[30] reported that hydrogen behaves differently while approaching a neutral metal atom (Ni) and a metal ion (Ni^+). For a neutral metal atom, similar to the metal atoms on surfaces and in bulk, it will transfer an electron to the approaching H_2 molecule to fill the antibonding orbital. This will lead to the bond cleavage of H-H favoring the atomic bonding between individual H atoms and metal atoms. In contrast, the ability of electron donation to a H_2 molecule becomes energetically inefficient for a transition metal ion due to the higher second ionization potential of the metal atom. Instead, a strong polarization effect will occur between the ion and H_2 molecule, which will enable several H_2 molecules to be chemisorbed in their molecular form onto a metal ion.

However, an isolated neutral metal atom or low-valent metal ion is unstable and cannot exist alone in nature. In addition, in a practical hydrogen storage material containing low-valent metal ions, the interactions between metal sites and H_2 molecules may involve multiple contributions to molecular chemisorption. As to the interactions mentioned above, combined with the Kubas-type interaction, it can be concluded that it is the coordinated TM atom, not a neutral metallic atom, that can bind H_2 in the form of a molecule. Moreover, the low-valent TM atoms with unsaturated configuration are vital for molecular chemisorption via orbital interaction, rather than physisorption.

Besides the low-valent and unsaturation state of TM atoms, the local electronic structure of TM atoms also contributes to adsorption energy. Recently, Zhang *et al.*[31] reported a low-coordinate Pt_1 single-atom catalyst for the hydrogenation of nitrobenzene and cyclohexanone. By impregnation-reduction steps, isolated Pt atoms can be stabilized on phosphomolybdic acid (PMA)-modified activated carbon (AC) (Pt-PMA/AC). To investigate the catalytic activity of Pt-PMA/AC in hydrogenation reactions, the authors firstly conducted a H_2-O_2 titration experiment [Figure 3A-C]. It is found that H_2 uptake of Pt-PMA/AC is due to the presence of Pt. In contrast, neither AC nor PMA/AC could adsorb H_2. This explained that the anchored Pt atoms strongly interact with PMA, inducing an electron out-flow. Thus, the Pt single atom enables the Pt-PMA/AC to possess the excellent hydrogen uptake property by its strong adsorption and polarization capacity. Besides the single atom, dual-metal dimers are also found to be capable of strong adsorption capacity. Zhang *et al.*[32] reported an asymmetrically heterogeneous atomic metal (Co and Pt) on

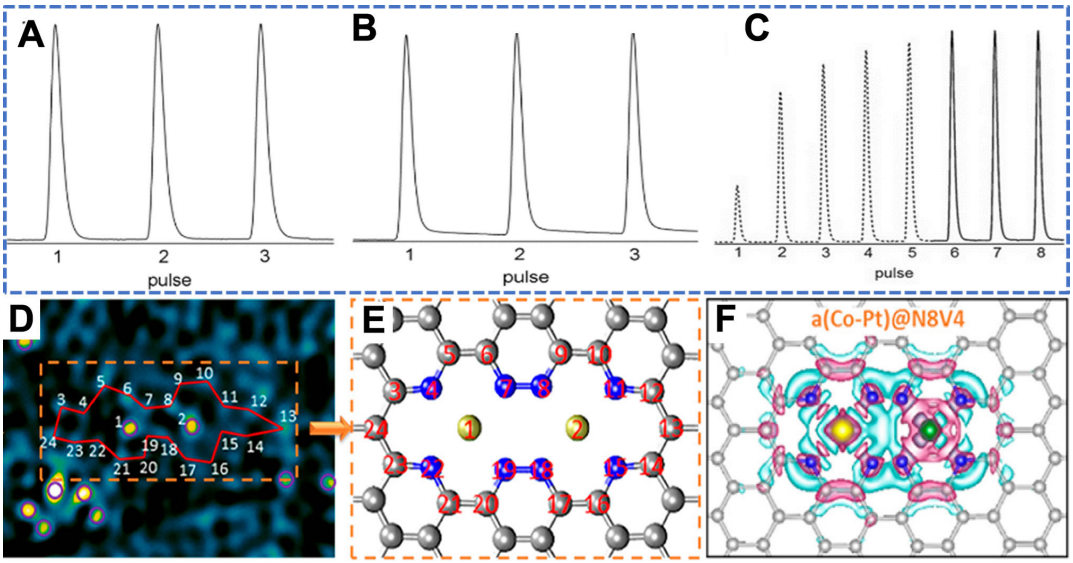

Figure 3. The atomically dispersed asymmetrical metallic structure. (A-C) H_2-O_2 titration profiles of AC, PMA/AC and Pt-PMA/AC. Reprinted with permission from Ref.[31]. Copyright 2016, WILEY VCH Verlag GmbH & Co. KGaA, Weinheim. (D) HAADF image of A-CoPt-NC after fast Fourier transformation filtering. The bright yellow spots are metal atoms, and the cyan spots are carbon atoms. Reprinted with permission from Ref.[32]. Copyright 2018, American Chemical Society. (E) Model of the configuration of the two metal atoms trapped in the defect, reconstructed from the observed atomic structure in (a). Purple circles mark metal atoms. The carbon atoms adjacent to metal atoms #1 and #2 are linked with a red line. Reprinted with permission from Ref.[32]. Copyright 2018, American Chemical Society. (F) Top view of the charge densities of a(Co-Pt)@N_8V_4, the pink area represents strong electron accumulation. Reprinted with permission from Ref.[32]. Copyright 2018, American Chemical Society.

N_8V_4 vacancies by the defect engineering method, shown in Figure 3D and E. The asymmetric deployment of Pt and Co in a(Co-Pt)@N_8V_4 can polarize the surface charges near the active sites by stimulating the electron accumulation around the Co atom and weakening electron accumulation around Pt [Figure 3F]. This charge distribution significantly enhances the adsorption of adsorbate molecules on active sites. Moreover, the asymmetric coordination of heterobimetallic species coupling at carbon defects can shift up the d orbital relative to the Fermi level, improving the binding energy between adsorbate and adsorption sites.

Based on the above analysis, a low valent ion state for coordinated TM atoms is the prerequisite of hydrogen adsorption without dissociation. Besides, the stabilization of chemisorbed molecular hydrogen under room temperature might need further modulation of the electronic structures to adsorption sites. On the one hand, the adsorption sites should possess a low coordination number. According to the d band center theory proposed by Hammer *et al.*[33], the lowering coordination number of center metal can shift the d-band level up to the Fermi level, which could strengthen the interaction between adsorption sites and adsorbate molecules. On the other hand, the asymmetric adsorption sites can effectively alter the charge distribution at the coordination structures, which will lead to local charge accumulation. This kind of charge redistribution could further promote the adsorption of adsorbate molecular by strong molecular deformation.

Previous experimental explorations further confirmed the role of the unique material structure on molecular chemisorption for hydrogen storage. Strategies of material synthesis include Grafting TM atoms to surfaces of porous materials (e.g., mesoporous silica)[34,35] and bridging the TM atoms with lightweight ligands (e.g., hydrazine) to the microporous materials[36-38]. In 2008, Hamaed *et al.*[34] reported organometallic Ti fragments as the H_2 storage material. The low-coordinated Ti (III) atoms were grafted onto mesoporous

silica using tri- and tetrabenzyl Ti precursors. The detailed experimental process is shown in Figure 4A. It can be observed that the low valent Ti atoms are three coordinates with two O atoms and one C atom, which can act as the adsorption sites. The hydrogen storage properties in Figure 4B show that the highest gravimetric storage value of 2.02 wt% recorded under the condition of 60 atm and 77 K is the sample with a Ti/Si molar ratio of 0.2 (0.20 Ti/HMS), while only 1.21 wt% hydrogen can be stored by silica precursor under the same condition. By calculations, an average of 2.7 H_2 molecules are adsorbed onto each Ti atom in 0.20 Ti/HMS. Notably that hydrogen adsorption isotherms of Ti-grafted samples do not saturate under the condition of 60 atm and 77 K. Increasing the pressure can further increase the numbers of H_2 molecules being adsorbed, according to the Le Chatelier's principle. Moreover, the binding enthalpy for Ti (III) grafted sample, by Clausius-Clapyron equation, is determined to be 22.04 kJ/mol compared to 3.5 kJ/mol for the pristine silica materials. On the one hand, the dramatically enhanced enthalpy reflects the molecular chemisorption mechanism differing from typical physical adsorption characteristics. On the other hand, the large enthalpy guarantees that around 1.1 hydrogen molecules are molecularly chemisorbed onto each Ti atom at room temperature.

In addition to grafting techniques, vanadium hydrazide gels with isolated and coordination-unsaturated V (III) species are also fabricated by using trismesitylvanadium (III) as a precursor and hydrazine as a linker[38]. The possible reaction mechanism is given in Figure 4C. The vanadium atom is tri-coordinated with N atoms in vanadium hydrazide gels, though some residual tetrahydrofuran (THF) molecules are bound to V atoms. The hydrogen adsorption isotherms [Figure 4D] present a linear hydrogen adsorption behavior, reflecting nondissociative hydrogen chemisorption, and up to 4.04 wt% of hydrogen are stored for sample C150 under 77 K and 85 bar. Even at room temperature, 49% of their adsorption can be retained as opposed to 77 K, owing to its greatly enhanced adsorption enthalpies from 3 to 36.5 kJ/mol.

MATERIAL DESIGN

Note that, though the works mentioned above exhibited good hydrogen adsorption performance, the lack of details of material structure characterization is unfavorable to our cognition of constitutive relationship, and it also brings difficulties to the further exploration of related materials. The core of rationalizing materials capable of molecular chemisorption is to fabricate isolated heteroatoms, simultaneously with low coordination number and unique coordination configuration. The expectation is that, by regulating the electronic structures of adsorption sites, the H_2 molecules can be chemisorbed with moderate bond energy, in which H_2 molecules can be adsorbed stably and released readily while exposed to a vacuum. Nevertheless, exploration and development of synthetic methodologies is a great challenge because it is difficult to synthesize a material that simultaneously has a high concentration of controllable coordination structures with unsaturated center metal atoms, lightweight and sufficient porosity, allowing the diffusion of hydrogen[39]. On the one hand, the high surface energy easily prompts the migration and aggregation of isolated metal atoms into particles. On the other hand, TMs in the solid state prefer to be hexa-coordinate in most cases, such as TiO_2, hindering the hydrogen molecular chemisorption. Experimental literature related to molecular chemisorption is rarely reported. Here, the methodology, defect engineering strategy, is highlighted as a simple and versatile strategy that could not only fabricate atomically dispersed and low-coordinate transition atoms but also modulate the coordination structure of centred TM atoms.

Defective carbon-based materials are widely considered as the ideal substrates owing to their good structural tunability, sufficient porosity, and lightweight. More importantly, the abundant defects in the carbon matrix could act as the anchoring sites to stabilize isolated TM atoms at atomic levels. Experiments have identified that a di-vacancy defect in graphene can trap atomic Ni specie in form of a four-coordinate structure (Ni-C_4) which exhibits excellent stability, shown in Figure 5A[40]. Moreover, the defect engineering

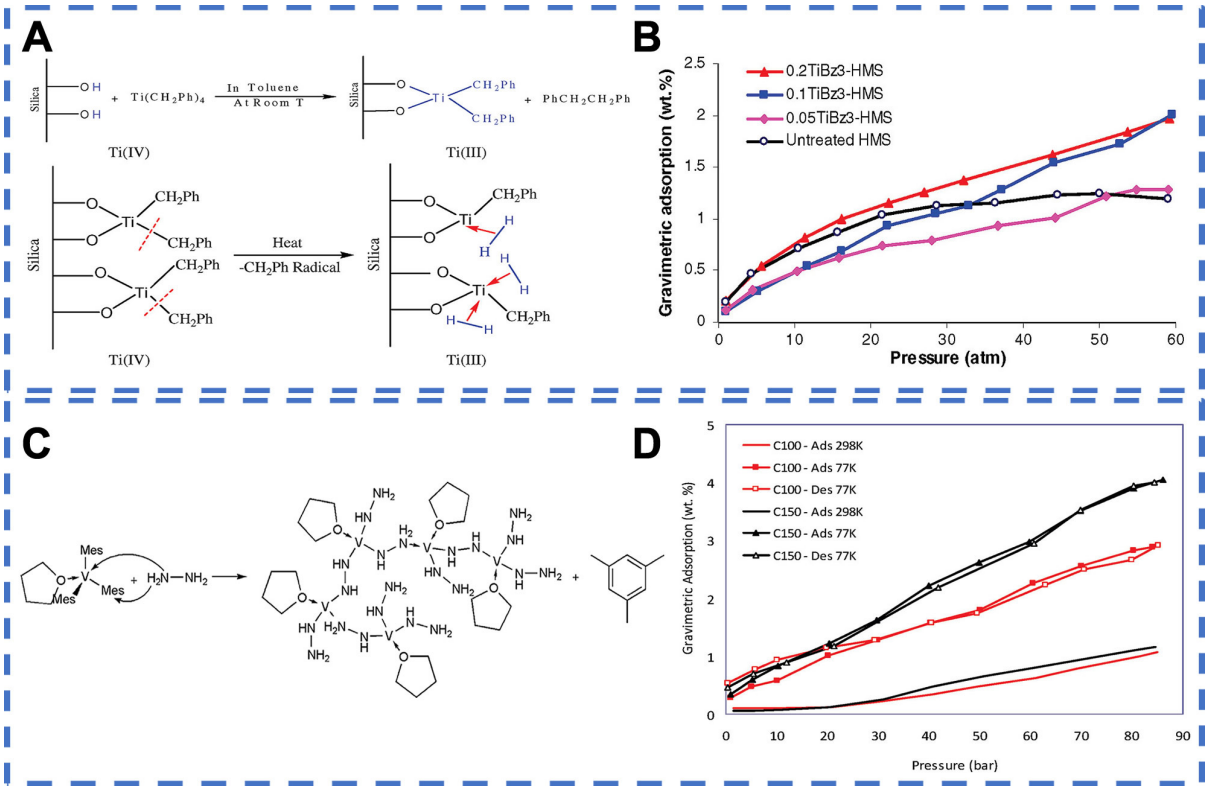

Figure 4. Hydrogen storage performance (via molecular chemisorption). (A) Schematic representation of the grafting of benzyl Ti species onto the surface of mesoporous silica. Reprinted with permission from Ref.[34]. Copyright 2008, American Chemical Society. (B) Hydrogen adsorption isotherms at 77 K for mesoporous silica treated with various molar equivalents of tribenzyl titanium. Reprinted with permission from Ref.[34]. Copyright 2008, American Chemical Society. (C) A possible mechanism for the reaction between $V(Mes)_3$·THF and N_2H_4. Reprinted with permission from Ref.[38]. Copyright 2010, American Chemical Society. (D) Hydrogen adsorption-desorption isotherms of vanadium hydrazide samples. Reprinted with permission from Ref.[38]. Copyright 2010, American Chemical Society.

strategy can be employed to regulate TM-atom-coordinated structures with different non-metallic element atoms (B, N and/or S). For example, the regulation of coordination configuration of defect-trapped transition metal atoms can be achieved by selectively replacing C atoms at defects with N atoms, shown in Figure 5B[41]. Furthermore, lowering coordination numbers by directly removing partial ligands seems feasible via an Ar-plasma etching technique[42]. Besides the configuration of the di-vacancy defect trapping a single Ni, the defect engineering can be applied to synthesize configurations that heterogeneous di-metal or even tri-metal confined into a multi-vacancy defect for hydrogen storage[43].

In addition to carbon-based materials, the defect engineering strategy can also be applied to transition metal chalcogenides by creating ion vacancy defects, which could not only modulate the coordination structure and charge distribution of center TM atoms but also optimize steric effect of H_2 adsorption. Reducing the coordination number of TM atoms by engineering anionic vacancy defects is practicable. Experimentally, the Ar-Plasma technique has successfully witnessed the removal of partial coordinated anionic ligands in transition metal chalcogenide[44]. Besides, chemical etching is also reported to create homogeneously distributed single S-vacancy defects onto the MoS_2 nanosheet surface with a high vacancy concentration of 12.11%, shown in Figure 5C[45].

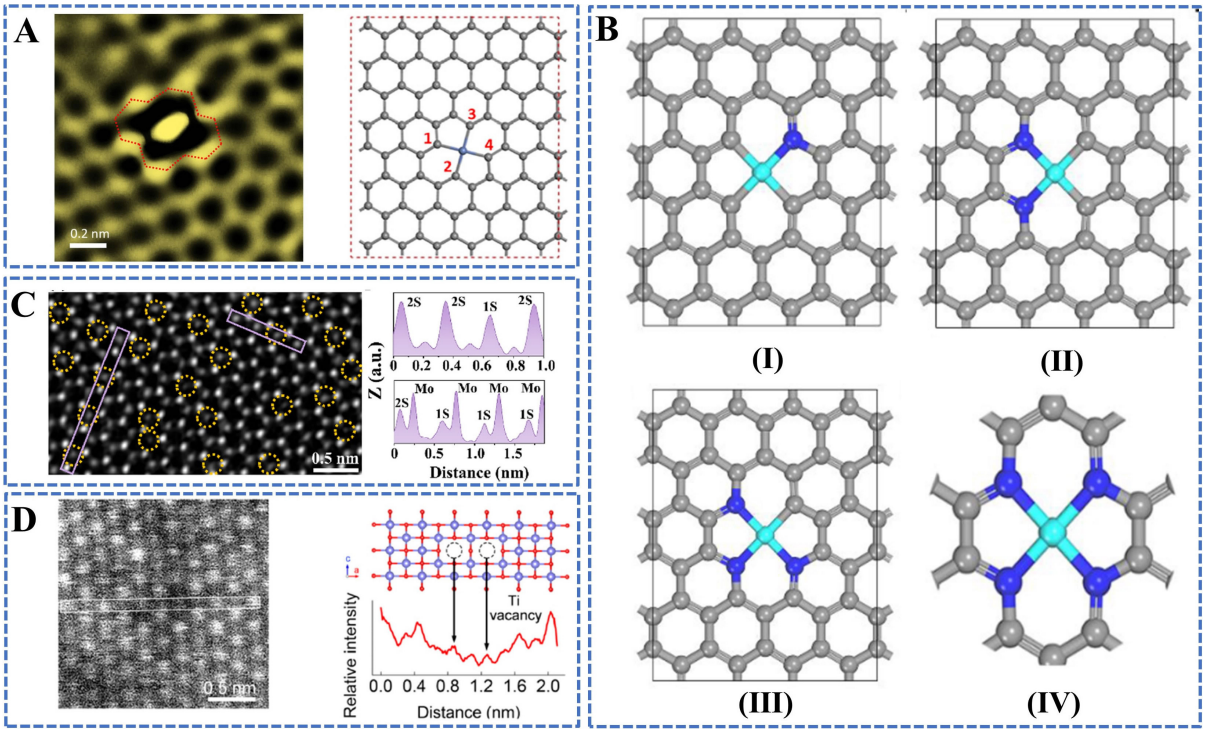

Figure 5. Methodology of the defect engineering. (A) HAADF-STEM image of the defective area with atomic Ni trapped (left) and the corresponding illustration of a single Ni atom anchored on di-vacancy (right). Reprinted with permission from Ref.[40]. Copyright 2018, Elsevier. (B) Top views of the optimized structures for $CoN_{4-x}C_x$. (I-IV) Represent four different coordination environments of cobalt atoms; I: CoN_1C_3, II: CoN_2C_2, III: CoN_3C_1, IV: CoN_4. Reproduced with permission from Ref.[41]. Copyright 2020, Wiley-VCH. (C) STEM image together with the line profiles extracted from the areas marked with purple rectangles of a monolayer MoS_2 flake film after etching. Reprinted with permission from Ref.[45]. Copyright 2020, American Chemical Society. (D) HAADF STEM images of a $Ti_{0.87}O_2$ nanosheet (left) and line profile exhibiting a clear intensity variation of atomic columns (right). The arrows indicate the Ti vacancies. Reprinted with permission from Ref.[46]. Copyright 2018, American Chemical Society.

Besides anionic vacancy defects, engineering cationic vacancy defects is also crucial for binding hydrogen via molecular chemisorption. The creation of cationic vacancies can undoubtedly enlarge the adjacent TM-TM distance, thus influencing the hydrogen adsorption behavior. Various techniques have been developed to create cationic vacancies, such as strong alkali etching[46], wet-chemistry approach[47], high-intensity ultrasonic processing[48] and so on. In Figure 5D, the HAADF-STEM image and line profile confirmed the Ti vacancy defects in the cation-deficient titanium oxide ($Ti_{0.87}O_2$) fabricated by alkali etching[46]. In addition to producing ion vacancy defects, the coordination environment and charge distribution of center metals can also be modified by introducing heteroatoms (metal or non-metal atoms) into the defects[44,49].

PERSPECTIVES AND DIRECTIONS

Developing hydrogen storage materials in the form of molecular chemisorption will construct a new conceptual paradigm in solid-state hydrogen storage fields. This unique hydrogen storage fashion endows the materials with fascinating adsorption enthalpy, allowing the hydrogen adsorption under ambient temperature and fast dehydrogenation simply by exposure to a vacuum condition. Though it is still premature to be fully understood, this method will provide a potential solution to hydrogen storage in the future. Currently, it remains a big challenge for current fabrication processes. The aforementioned defect engineering offers a doable way, albeit it needs to be further verified for hydrogen storage. Efforts to explore the unique hydrogen storage materials and understand the adsorption mechanism is urgently required.

1. Strategies of synthesizing molecular-chemisorption type materials aim to acquire high concentration of low-valent, low-coordinate binding sites.

2. Factors that affect the electronic structures of adsorption sites should be delicately and sophisticatedly modulated, including: (1) adsorption sites, such as species, spacing and quantity of adsorbent atoms; (2) coordination environment, such as coordination number, coordination atom, symmetry/asymmetry of coordination structure, and position (in plane or edge); and (3) substrates.

3. The cycle stability of materials during de-/hydrogenation is a non-ignorable performance. The interaction between ligands and central TM atoms should be fully considered prior to material design.

4. More accurate theoretical calculations combined with matching adsorption models should be provided to explore the critical interactions behind the molecular chemisorption, favoring the correlation between structure of adsorption sites with hydrogen adsorption performance.

5. Besides the TM atoms, efforts should be also devoted into developing η^2-σ complexes (type III method referred in Figure 2) constructing an integrated molecular chemisorption system.

DECLARATIONS

Authors' contributions

Conceived and wrote the paper: Lang C, Jia Y, Yan X, Ouyang L, Zhu M, Yao X

Availability of data and materials

Not applicable.

Financial support and sponsorship

This work has been supported by the Australian Research Council (ARC DP200103043) and ARC Discovery Early Career Researcher Award (ARC DE180101030).

Conflicts of interest

All authors declared that there are no conflicts of interest.

Ethical approval and consent to participate

Not applicable.

Consent for publication

Not applicable.

REFERENCES

1. Weidenthaler C, Felderhoff M. Solid-state hydrogen storage for mobile applications: Quo Vadis? *Energy Environ Sci* 2011;4:2495. DOI
2. Hwang HT, Varma A. Hydrogen storage for fuel cell vehicles. *Curr Opin Chem Eng* 2014;5:42-8. DOI PubMed
3. Lang C, Jia Y, Yao X. Recent advances in liquid-phase chemical hydrogen storage. *Energy Stor Mater* 2020;26:290-312. DOI
4. Schlapbach L and Züttel A. Hydrogen-storage materials for mobile applications. *Nature* 2001;414:353-8. DOI PubMed
5. Dalebrook AF, Gan W, Grasemann M, Moret S, Laurenczy G. Hydrogen storage: beyond conventional methods. *Chem Commun (Camb)* 2013;49:8735-51. DOI PubMed
6. Chen Z, Kirlikovali KO, Idrees KB, Wasson MC, Farha OK. Porous materials for hydrogen storage. *Chem* 2022. DOI
7. Li Y, Xiao Y, Dong H, Zheng M, Liu Y. Polyacrylonitrile-based highly porous carbon materials for exceptional hydrogen storage. *Int*

J Hydrogen Energy 2019;44:23210-5. DOI
8. Blankenship LS, Balahmar N, Mokaya R. Oxygen-rich microporous carbons with exceptional hydrogen storage capacity. *Nat Commun* 2017;8:1545. DOI PubMed PMC
9. Germain J, Fréchet JM, Svec F. Nanoporous polymers for hydrogen storage. *Small* 2009;5:1098-111. DOI PubMed
10. Sun G, Tangpanitanon J, Shen H, et al. Physisorption of molecular hydrogen on carbon nanotube with vacant defects. *J Chem Phys* 2014;140:204712. DOI PubMed
11. Panchariya DK, Rai RK, Anil Kumar E, Singh SK. Core-shell zeolitic imidazolate frameworks for enhanced hydrogen storage. *ACS Omega* 2018;3:167-75. DOI PubMed PMC
12. Lee S, Lee J, Kim Y, Kim J, Lee K, Park S. Recent progress using solid-state materials for hydrogen storage: a short review. *Processes* 2022;10:304. DOI
13. Shayeganfar F, Shahsavari R. Oxygen- and lithium-doped hybrid boron-nitride/carbon networks for hydrogen storage. *Langmuir* 2016;32:13313-21. DOI PubMed
14. Yu H, Bennici S, Auroux A. Hydrogen storage and release: kinetic and thermodynamic studies of MgH_2 activated by transition metal nanoparticles. *Int J Hydrogen Energy* 2014;39:11633-41. DOI
15. Zhang J, Li Z, Wu Y, et al. Recent advances on the thermal destabilization of Mg-based hydrogen storage materials. *RSC Adv* 2019;9:408-28. DOI
16. Luo Q, Li J, Li B, Liu B, Shao H, Li Q. Kinetics in Mg-based hydrogen storage materials: enhancement and mechanism. *J Magnes Alloy* 2019;7:58-71. DOI
17. Cao Z, Ouyang L, Wu Y, et al. Dual-tuning effects of In, Al, and Ti on the thermodynamics and kinetics of $Mg_{85}In_5Al_5Ti_5$ alloy synthesized by plasma milling. *J Alloys Compd* 2015;623:354-8. DOI
18. Konarova M, Tanksale A, Norberto Beltramini J, Qing Lu G. Effects of nano-confinement on the hydrogen desorption properties of MgH2. *Nano Energy* 2013;2:98-104. DOI
19. Martelli P, Caputo R, Remhof A, Mauron P, Borgschulte A, Züttel A. Stability and decomposition of $NaBH_4$. *J Phys Chem C* 2010;114:7173-7. DOI
20. Urgnani J, Torres F, Palumbo M, Baricco M. Hydrogen release from solid state $NaBH_4$. *Int J Hydrogen Energy* 2008;33:3111-5. DOI
21. Mao J, Yu X, Guo Z, Liu H, Wu Z, Ni J. Enhanced hydrogen storage performances of $NaBH_4$-MgH_2 system. *J Alloys Compd* 2009;479:619-23. DOI
22. García-holley P, Schweitzer B, Islamoglu T, et al. Benchmark study of hydrogen storage in metal-organic frameworks under temperature and pressure swing conditions. *ACS Energy Lett* 2018;3:748-54. DOI
23. Kubas GJ, Ryan RR, Swanson BI, Vergamini PJ, Wasserman HJ. Characterization of the first examples of isolable molecular hydrogen complexes, $M(CO)_3(PR_3)_2(H_2)$ (M = molybdenum or tungsten; R = Cy or isopropyl). Evidence for a side-on bonded dihydrogen ligand. *J Am Chem Soc* 1984;106:451-2. DOI
24. Mingos D. Recent developments in theoretical organometallic chemistry. Elsevier; 1977. p. 1-51. DOI
25. Mrtensson A, Nyberg C, Andersson S. Observation of molecular H_2 chemisorption on a nickel surface. *Phys Rev Lett* 1986;57:2045-8. DOI PubMed
26. Berwanger J, Polesya S, Mankovsky S, Ebert H, Giessibl FJ. Atomically resolved chemical reactivity of small Fe clusters. *Phys Rev Lett* 2020;124:096001. DOI PubMed
27. Vitillo JG, Regli L, Chavan S, et al. Role of exposed metal sites in hydrogen storage in MOFs. *J Am Chem Soc* 2008;130:8386-96. DOI PubMed
28. Zhou W, Yildirim T. Nature and tunability of enhanced hydrogen binding in metal-organic frameworks with exposed transition metal sites. *J Phys Chem C* 2008;112:8132-5. DOI
29. Liu Y, Su B, Dong W, Li ZH, Wang H. Structural characterization of a boron(III) η^2-σ-silane-complex. *J Am Chem Soc* 2019;141:8358-63. DOI PubMed
30. Niu J, Rao BK, Jena P. Binding of hydrogen molecules by a transition-metal ion. *Phys Rev Lett* 1992;68:2277-80. DOI PubMed
31. Zhang B, Asakura H, Zhang J, Zhang J, De S, Yan N. Stabilizing a $Platinum_1$ single-atom catalyst on supported phosphomolybdic acid without compromising hydrogenation activity. *Angew Chem* 2016;128:8459-63. DOI PubMed
32. Zhang L, Fischer JMTA, Jia Y, et al. Coordination of atomic Co-Pt coupling species at carbon defects as active sites for oxygen reduction reaction. *J Am Chem Soc* 2018;140:10757-63. DOI PubMed
33. Hammer B, Nørskov J. Theoretical surface science and catalysis-calculations and concepts. Impact of Surface Science on Catalysis. Elsevier; 2000. pp. 71-129. DOI
34. Hamaed A, Trudeau M, Antonelli DM. H_2 storage materials (22 KJ/mol) using organometallic Ti fragments as sigma-H_2 binding sites. *J Am Chem Soc* 2008;130:6992-9. DOI PubMed
35. Hoang TKA, Hamaed A, Trudeau M, Antonelli DM. Bis(benzene) and Bis(cyclopentadienyl) V and Cr doped mesoporous silica with high enthalpies of hydrogen adsorption. *J Phys Chem C* 2009;113:17240-6. DOI
36. Xu G, Pareek K, Li N, Cheng H. High capacity hydrogen storage at room temperature via physisorption in a coordinatively unsaturated iron complex. *Int J Hydrogen Energy* 2015;40:16330-7. DOI
37. Hoang TK, Hamaed A, Moula G, Aroca R, Trudeau M, Antonelli DM. Kubas-type hydrogen storage in V(III) polymers using tri- and tetradentate bridging ligands. *J Am Chem Soc* 2011;133:4955-64. DOI PubMed
38. Hoang TK, Webb MI, Mai HV, et al. Design and synthesis of vanadium hydrazide gels for Kubas-type hydrogen adsorption: a new class of hydrogen storage materials. *J Am Chem Soc* 2010;132:11792-8. DOI PubMed
39. Skipper CVJ, Antonelli DM, Kaltsoyannis N. Are metal-metal interactions involved in the rising enthalpies observed in the Kubas

binding of H_2 to hydrazine-linked hydrogen storage materials? *J Phys Chem C* 2012;116:19134-44. DOI

40. Zhang L, Jia Y, Gao G, et al. Graphene defects trap atomic Ni species for hydrogen and oxygen evolution reactions. *Chem* 2018;4:285-97. DOI
41. Yang Q, Jia Y, Wei F, et al. Understanding the Activity of Co-$N_{4-x}C_x$ in atomic metal catalysts for oxygen reduction catalysis. *Angew Chem* 2020;132:6178-83. DOI PubMed
42. Tao L, Wang Q, Dou S, et al. Edge-rich and dopant-free graphene as a highly efficient metal-free electrocatalyst for the oxygen reduction reaction. *Chem Commun (Camb)* 2016;52:2764-7. DOI PubMed
43. Zhu X, Zhang D, Chen C, et al. Harnessing the interplay of Fe-Ni atom pairs embedded in nitrogen-doped carbon for bifunctional oxygen electrocatalysis. *Nano Energy* 2020;71:104597. DOI
44. Zhuang L, Jia Y, Liu H, et al. Defect-Induced Pt-Co-Se coordinated sites with highly asymmetrical electronic distribution for boosting oxygen-involving electrocatalysis. *Adv Mater* 2019;31:e1805581. DOI PubMed
45. Wang X, Zhang Y, Si H, et al. Single-atom vacancy defect to trigger high-efficiency hydrogen evolution of MoS_2. *J Am Chem Soc* 2020;142:4298-308. DOI PubMed
46. Xiong P, Zhang X, Zhang F, et al. Two-dimensional unilamellar cation-deficient metal oxide nanosheet superlattices for high-rate sodium ion energy storage. *ACS Nano* 2018;12:12337-46. DOI PubMed
47. Liu B, Wang Y, Peng HQ, et al. Iron vacancies induced bifunctionality in ultrathin feroxyhyte nanosheets for overall water splitting. *Adv Mater* 2018:e1803144. DOI PubMed
48. Dou Y, He CT, Zhang L, et al. Approaching the activity limit of $CoSe_2$ for oxygen evolution via Fe doping and Co vacancy. *Nat Commun* 2020;11:1664. DOI PubMed PMC
49. Zhuang L, Jia Y, Liu H, et al. Sulfur-modified oxygen vacancies in iron-cobalt oxide nanosheets: enabling extremely high activity of the oxygen evolution reaction to achieve the industrial water splitting benchmark. *Angew Chem Int Ed Engl* 2020;59:14664-70. DOI PubMed

Wang *et al. Chem Synth* 2022;2:2
DOI: 10.20517/cs.2022.02

Chemical Synthesis

Research Article

Open Access

Two-dimensional manganese oxide on ceria for the catalytic partial oxidation of hydrocarbons

Hai Wang[1], Liang Wang[1,*], Qingsong Luo[1], Jian Zhang[2], Chengtao Wang[3], Xin Ge[4], Wei Zhang[4,*], Feng-Shou Xiao[1,*]

[1]Key Lab of Biomass Chemical Engineering of Ministry of Education, College of Chemical and Biological Engineering, Zhejiang University, Hangzhou 310028, Zhejiang, China.
[2]Beijing Advanced Innovation Center for Soft Matter, Science, and Engineering, Beijing University of Chemical Technology, Beijing 100029, China.
[3]Key Laboratory of Applied Chemistry of Zhejiang Province and Department of Chemistry, Zhejiang University, Hangzhou 310028, Zhejiang, China.
[4]Key Laboratory of Automobile Materials MOE, School of Materials Science & Engineering, Jilin Provincial International Cooperation Key Laboratory of High-Efficiency Clean Energy Materials, Electron Microscopy Center, and International Center of Future Science, Jilin University, Changchun 130012, Jilin, China.

***Correspondence to:** Prof. Liang Wang, Key Lab of Biomass Chemical Engineering of Ministry of Education, College of Chemical and Biological Engineering, Zhejiang University, Hangzhou 310028, Zhejiang, China. E-mail: liangwang@zju.edu.cn; Prof. Wei Zhang, Key Laboratory of Automobile Materials MOE, School of Materials Science & Engineering, Jilin Provincial International Cooperation Key Laboratory of High-Efficiency Clean Energy Materials, Electron Microscopy Center, and International Center of Future Science, Jilin University, Changchun 130012, Jilin, China. E-mail: weizhang@jlu.edu.cn; Prof. Feng-Shou Xiao, Key Lab of Biomass Chemical Engineering of Ministry of Education, College of Chemical and Biological Engineering, Zhejiang University, Hangzhou 310028, Zhejiang, China. E-mail: fsxiao@zju.edu.cn

How to cite this article: Wang H, Wang L, Luo Q, Zhang J, Wang C, Ge X, Zhang W, Xiao FS. Two-dimensional manganese oxide on ceria for the catalytic partial oxidation of hydrocarbons. *Chem Synth* 2022;2:2. https://dx.doi.org/10.20517/cs.2022.02

Received: 22 Jan 2022 **First Decision:** 11 Feb 2022 **Revised:** 27 Feb 2022 **Accepted:** 2 Mar 2022 **Published:** 16 Mar 2022

Academic Editor: Bao-Lian Su **Copy Editor:** Xi-Jun Chen **Production Editor:** Xi-Jun Chen

Abstract

Although the rational synthesis of catalysts with strong oxide-support interactions to modulate the geometric and electronic structures and achieve unusual catalytic performance is challenging in heterogeneous catalysis, it is in significant demand for the efficient and sustainable transformation of chemicals. Here, we report the synthesis and performance of a ceria-supported two-dimensional manganese oxide catalyst with strong metal oxide-support interactions, which help to produce well-dispersed and amorphous MnO_x layers on the CeO_2 matrix (MnO_x/CeO_2). This catalyst readily reacts with molecular oxygen to give a high capacity of active oxygen species, owing to the interfacial effect. The C-H bonds are adsorbed and activated by these active interfacial oxygen species, leading to high activities and selectivities in the industrially important C-H bond activation reactions, such as the oxidation of hydrocarbons to alcohols and ketones with molecular oxygen under solvent- and initiator-free

conditions at mild temperature. The performance of the MnO_x/CeO_2 catalyst is greater than that of noble metal and highly efficient Mn-Ce solid-solution catalysts. More importantly, the catalyst is stable and exhibits constant reactivity in continuous recycling tests. These results are important for the design of highly efficient catalysts for the selective oxidation of hydrocarbons.

Keywords: Strong oxide-support interactions, C-H oxidation, MnO_x/CeO_2 catalyst, heterogeneous catalysis

INTRODUCTION

The oxidation of sp^3-hybridized C-H bonds has emerged as a facile and industrially important process for the sustainable production of alcohols, ketones and epoxides from petroleum hydrocarbons[1-4]. Generally, the inorganic salts of ClO_4^- and NO_3^- are used as oxidants, which are costly and environmentally unfriendly[5]. Although molecular oxygen is regarded as a favorable oxidant, harsh reaction conditions are necessary for the activation of strong C-H bonds, which generally leads to significant energy consumption and uncontrollable selectivities[6-9]. In addition, over-oxidation occurs in many cases to produce carbon dioxide and other byproducts, particularly during vapor-phase oxidation[3,10]. As an attractive process in industry, the liquid-phase oxidation of C-H bonds has attracted tremendous attention, but the conversion of hydrocarbon substrates is always unsatisfactory. Subsequently, noble metal catalysts, peroxide initiators, organic solvents, supercritical CO_2 and ionic liquid additives are used for enhancing the substrate conversion[11-16], but new problems arise, such as increased costs and extra product purification. Therefore, the efficient catalytic oxidation of C-H bonds with molecular oxygen over non-noble metal catalysts, as well as avoiding the use of solvents and initiator additives, remains challenging.

Mn-Ce oxides have been extensively investigated as efficient catalysts for the total oxidation of NO[17], CO[18-23] and organic molecules for pollutant removal[24-28], because of their high activity toward the activation of molecular oxygen. The features of Mn-Ce oxides in molecular oxygen activation have also motivated research into the selective oxidation of C-H bond and excellent success has been achieved. For example, Mn-Ce oxides were synthesized with surfactants or ionic liquids to maximize the solid-solution phase, which readily exhibited superior activity and selectivity for the selective oxidation of hydrocarbons[18]. However, organic solvents are still necessary in most of these cases[18]. Furthermore, the expensive surfactants and ionic liquids still limit their practical applications. Developing strategies for the synthesis of efficient Mn-Ce catalysts therefore remains a vital area of research in this field.

Here, we report a ceria-supported two-dimensional manganese oxide catalyst that is highly efficient for the selective oxidation of hydrocarbons without the use of solvents and initiator additives. The key to this success is anchoring the two-dimensional and amorphous manganese oxide layers on the cerium matrix (MnO_x/CeO_2) via strong oxide-support interactions (SOSIs). Owing to these features, the catalyst readily reacts with molecular oxygen to give a high capacity of active oxygen species at 46.1%. In the solvent- and initiator-free oxidation of C-H bonds on a series of hydrocarbons with molecular oxygen at low temperatures, the MnO_x/CeO_2 catalyst exhibits high activities and selectivities, as well as good stabilities in the recycling tests (Scheme 1). For example, in the aerobic oxidation of ethylbenzene, it gives a conversion of 63.5% and a selectivity of 95.7% to the corresponding alcohol/ketone products, thereby outperforming highly efficient heterogeneous catalysts under solvent- and initiator-free systems reported in the literature.

EXPERIMENTAL

Synthesis

Synthesis of MnO_x/CeO_2 catalysts

As a typical synthesis of the MnO_x/CeO_2(0.05) [where 0.05 is the theoretical Mn/(Mn + Ce) molar ratio]

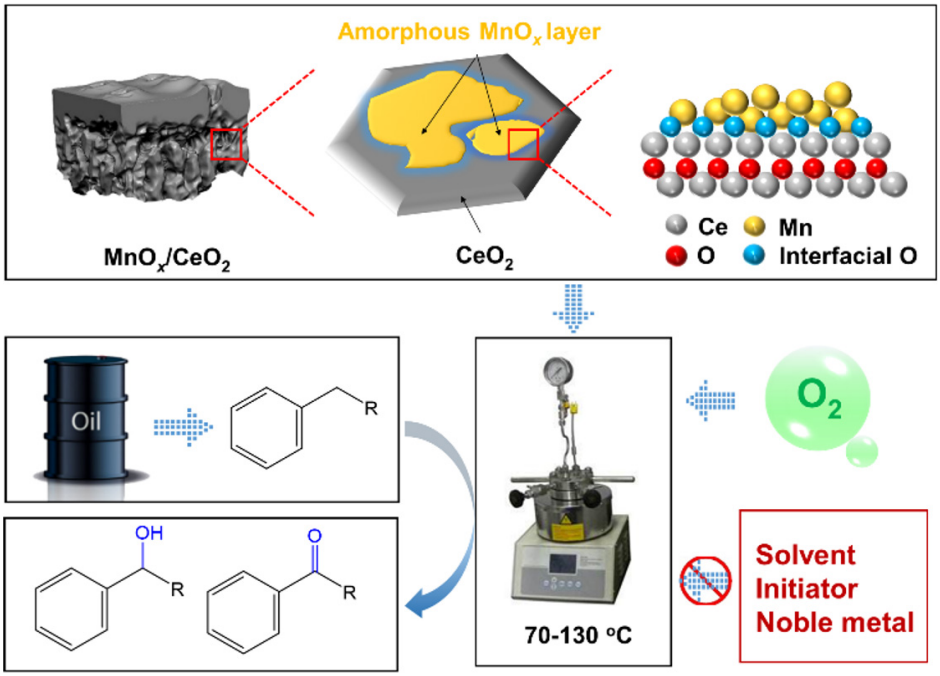

Scheme 1. Synthetic and catalytic strategies for ceria-supported two-dimensional manganese oxide catalyst with strong oxide-support interactions.

catalyst, 6 g of cerium nitrate [$Ce(NO_3)_3 \cdot 6H_2O$] and 0.26 g of a manganese nitrate aqueous solution (50 wt.%) were dissolved in 5 g of ethanol and 5 g of deionized water in flask A and stirred at room temperature for 20 min. Meanwhile, 2 g of glycerol and 4.8 g of citric acid monohydrate were dissolved in 5 g of ethanol and 5 g of deionized water in flask B and stirred at room temperature for 20 min. After that, the liquor in flask B was added to flask A with continuous stirring at room temperature for 3 h and 90 °C for 3 h in a closed reactor. Finally, the ethanol and water solvent was volatilized to obtain a foamed solid. After drying at 100 °C overnight and calcining at 800 °C for 4 h in air to remove the organic species, the $MnO_x/CeO_2(0.05)$ catalyst was finally obtained. CeO_2 and $MnO_x/CeO_2(y)$ catalysts with Mn/(Mn + Ce) molar ratios of 0.025, 0.1, 0.2 and 0.3 were synthesized using the same procedure by adjusting the amount of the manganese nitrate aqueous solution in the starting solutions. Accordingly, the samples were termed as CeO_2, $MnO_x/CeO_2(0.025)$, $MnO_x/CeO_2(0.1)$, $MnO_x/CeO_2(0.2)$ and $MnO_x/CeO_2(0.3)$, respectively.

Synthesis of acid-treated $MnO_x/CeO_2(0.05)$

First, the acid-treated $MnO_x/CeO_2(0.05)$ catalyst was synthesized by washing the as-synthesized $MnO_x/CeO_2(0.05)$ with diluted hydrochloric acid (20%) at 90 °C for 4 h. The solid was then collected by centrifugation and washed with a large excess of deionized water and dried in air at 100 °C overnight. Finally, the sample was calcined in air at 400 °C for 2 h in a rotating quartz tube to obtain the acid-treated $MnO_x/CeO_2(0.05)$ catalyst.

Synthesis of MnO_x/CeO_2 and MnO_x/SiO_2

For comparison, MnO_x/CeO_2 with an Mn/(Mn + Ce) molar ratio at 0.05 was also prepared by an incipient wetness co-impregnation method. In a typical run, an $Mn(NO_3)_2$ aqueous solution (50 wt.%) was used as a precursor and CeO_2 was used as a support (CeO_2 was prepared by the citric acid-assisted method discussed above). After impregnation, the catalysts were placed in the atmosphere statically overnight and then dried in an oven and calcined at 600 °C for 4 h in air. The resulting catalyst was denoted as MnO_x/CeO_2.

MnO_x/SiO_2 was also synthesized by the same procedure for MnO_x/CeO_2 but using SiO_2 as the support.

Catalysis

Catalytic oxidation of hydrocarbons

The oxidation of hydrocarbons in the liquid phase was performed with a high-pressure autoclave reactor equipped with a magnetic stirrer (900 rpm). In a typical run, the catalyst and hydrocarbon were mixed in the reactor and pure oxygen was used for the reaction. The autoclave was purged with oxygen three times to remove the air in the autoclave before the reaction. Oxygen was then introduced to the desired pressure. Next, the reactor was rapidly heated to the desired temperature (the reaction temperature was measured by a thermocouple in the autoclave and the pressure was measured at the reaction temperature). After the reaction, the reactor was placed in an ice bath to stop the reaction, and bromobenzene or biphenyl was used as the internal standard. In the stability test, the catalyst was removed from the reactor and washed with ethanol after each reaction run, dried overnight at 150 °C and then used in the next experiment to evaluate its recyclability.

The products were analyzed by gas chromatography (GC-14C, Shimadzu, with a flame ionization detector and ethanol or acetonitrile used to dilute the liquor before the analysis) with a flexible quartz capillary column (OV-17). The gas-phase products (e.g., CO or CO_2 produced from over-oxidation) were analyzed using a Fu Li-9790 gas chromatograph equipped with a thermal conductivity detector (TCD). The as-synthesized catalyst was used each time to make sure the reactions were conducted under identical conditions. High-pressure oxygen has been extensively used in aerobic oxidations and the reaction systems in this work were out of the explosion limits of the reactants. For example, the explosion limit of ethylbenzene is 1.0%-7.1% in oxygen and the concentration of ethylbenzene in the gaseous phase in this work is out of the explosion limit. Fire and static electricity were therefore avoided for safety reasons.

Catalytic oxidation of CO

The oxidation of CO was performed in a continuous-flow fixed-bed quartz vertical reactor (length of 400 mm and internal diameter of 6 mm) in a temperature controllable oven. First, 0.2 g of catalyst (40-60 mesh) diluted with 0.6 g of quartz sands (40-60 mesh) were located in the reactor. The feed gas containing 1% CO and 18% O_2 in He was introduced with a total rate of 20 sccm. The concentration of CO in the feed and emission gases was continually monitored by the chromatograph equipped with the TCD detector. In the kinetic study, the partial pressure of CO was controlled by adjusting the flow rate of CO and the total rate was balanced with He.

Characterization

Temperature-programmed desorption

The temperature-programmed desorption of O_2 (O_2-TPD) was measured in a BELCAT II catalyst analyzer equipped with a TCD. As a typical run, 30 mg of solid catalyst were pretreated at 600 °C for 1 h in air before the measurement and then cooled to 50 °C. The sample was then heated to 800 °C at a ramp rate of 10 °C/min for detecting the desorbed oxygen species.

In-situ Fourier transform infrared spectroscopy

The *in-situ* Fourier transform infrared (FTIR) spectra were recorded using a Nicolet *is*50 FTIR spectrometer equipped with an MCT/A detector, ZnSe windows and a high temperature reaction chamber. As a typical run, 50 mg of MnO_x/CeO_2(0.05) were localized in the sample chamber and pretreated at 120 °C for 1 h in flowing Ar (30 sccm) and then cooled to room temperature. The steam containing ethylbenzene (partial pressure in the range of 9-16 mbar) was introduced into the system with a flow of Ar carrier gas (30 sccm). After adsorption for 1 h at room temperature, a pure Ar gas was introduced to purge the sample for another

1 h and the FTIR spectrum of ethylbenzene adsorbed on the solid sample was then recorded. After increasing the reaction temperature to 160 °C in flowing Ar and maintaining it for 30 min, the FTIR spectra were recorded to understand the interaction between ethylbenzene and the active oxygen species on the catalyst surface. Whilst maintaining the temperature of the chamber at 160 °C, oxygen was introduced to further promote the interaction, where the FTIR spectra were recorded to detect the formation of carbon-oxygen species.

To investigate the crucial role of the active oxygen species on the catalyst, we eliminated the oxygen by H_2 reduction during the *in-situ* FTIR study. In a typical run, 50 mg of the MnO_x/CeO_2(0.05) sample were pretreated at 200 °C with 10% H_2/Ar for 2 h and then cooled to room temperature. The steam containing ethylbenzene was then introduced into the system with a flow of Ar carrier gas (30 sccm). After adsorption for 1 h at room temperature, a pure Ar gas was introduced to purge the sample for another 1 h. The FTIR spectrum of ethylbenzene adsorbed on the solid sample was then recorded. After that, the MnO_x/CeO_2(0.05) catalyst was treated at 200 °C in O_2 for 1 h and then cooled to room temperature. Equivalently, ethylbenzene was introduced into the sample again and the FTIR spectrum was collected for understanding its adsorption behavior on the oxidized MnO_x/CeO_2(0.05) sample. The chamber temperature was then increased to 80 °C with an oxygen flow and the FTIR spectra were recorded to characterize the interaction of ethylbenzene with the catalyst.

In-situ Raman spectroscopy

Raman spectra were recorded using an HR800 Raman spectrometer equipped with an Ar excitation source (λ = 514.532 nm). The gaseous steam was introduced into the system with a flow of Ar carrier gas (30 sccm) with the reactant partial pressure in the range of 10-20 mbar. To prove the presence of active surface oxygen species, *in-situ* Raman spectra were performed with 40 mg of the CeO_2 or MnO_x/CeO_2(0.05) sample dried in a vacuum overnight to remove the water species. The Raman spectra of CeO_2 were recorded at room temperature in air. The Raman spectra of MnO_x/CeO_2(0.05) were recorded at room temperature in air, room temperature in O_2, 140 °C in Ar, 250 °C in Ar, 350 °C in Ar and room temperature in O_2.

To further confirm the active surface oxygen species, *in-situ* oxidation of CO was conducted with 40 mg of the CeO_2 or MnO_x/CeO_2(0.05) sample dried in a vacuum overnight to remove the water species. The Raman spectra of CeO_2 were recorded at room temperature in air. The Raman spectra of MnO_x/CeO_2(0.05) were recorded at room temperature in air, room temperature in O_2, 140 °C in CO, 250 °C in CO, 350 °C in CO and 350 °C in CO and O_2.

Catalytic data analysis

Carbon balance during oxidation of hydrocarbons

The carbon balance before and after the reaction was calculated based on the number of carbon atoms in all the liquid reactants and products. For example, in the oxidation of ethylbenzene, acetophenone and phenylethyl alcohol are the detectable liquid products, while the CO_2 from over-oxidation was not included in calculating the carbon balances. The carbon balance values are calculated according to the following equation:

$$C\% = \frac{M_f*8 + M_1*n_1 + M_2*n_2 + M_3*n_3 + \ldots + M_x*n_x}{M_e*8} \times 100\%$$

where C% is the carbon balance, M_f is the final number of moles of ethylbenzene in the reactor after reaction, 8 is the number of carbon atoms in a single ethylbenzene molecule, M_1 (M_2, M_3, ……, M_x) is the number of moles of liquid product 1 (product 2, 3, ……, x) in the reactor after the reaction, n_1 (n_2, n_3, ……, n_x) is the number of carbon atoms in a single molecule of product 1 (product 2, 3, ……, x) and M_e is the number of moles of ethylbenzene in the feed mixture before the reaction.

In the kinetic study, the average reaction rates were calculated from the number of moles of substrate converted per gram of the catalyst in 1 h (mmol g_{cat}^{-1} h^{-1}) and the conversion of the reactants was controlled to be lower than 20%, which approximated the true reaction rates.

RESULTS AND DISCUSSION

Synthesis and structural characterization

The CeO_2 support was synthesized via a citric acid-assisted method [Figure 1A]. Typically, $Ce(NO_3)_3$ and citric acid were dissolved in a mixture of water, ethanol and glycerol, where the citric acid can chelate with metal ions to form the metal citrate precursor [Supplementary Figure 1]. After removing the solvent and forming a fluffy material by stirring at 90 °C, followed by calcination to remove the organic species, the CeO_2 was finally obtained [Supplementary Figure 2]. The CeO_2-supported manganese oxide catalysts were synthesized following the same procedures by adding $Mn(NO_3)_2$ in the starting solution and denoted as $MnO_x/CeO_2(y)$ [where y is the theoretical molar ratio of Mn/(Mn + Ce)] [Supplementary Figures 3-5].

Figure 1B shows the X-ray diffraction (XRD) patterns of the commercial CeO_2 and $MnO_x/CeO_2(y)$ samples with different Mn loadings, which all exhibit peaks at 28.7°, 33.3°, 47.7° and 56.5°, assigned to the (111), (200), (220) and (311) diffraction peaks of a typical CeO_2 crystal, respectively[18,22]. Notably, the shift of these diffraction peaks was undetectable for the $MnO_x/CeO_2(y)$ samples compared to the pure CeO_2, suggesting a lack of the Mn-Ce solid-solution phase[18,22]. The high dispersion and/or amorphous features of MnO_x on the CeO_2 matrix were evidenced by the undetectable XRD peaks associated with manganese oxide for $MnO_x/CeO_2(0.025)$, $MnO_x/CeO_2(0.05)$ and $MnO_x/CeO_2(0.1)$ [Figure 1C]. However, the diffraction patterns of higher Mn content samples showed the crystallization of a Mn_3O_4 hausmannite phase (JCPDS 071841)[28], demonstrating the formation of sintered MnO_x species in these samples.

The N_2 sorption demonstrates that the surface areas of CeO_2 and $MnO_x/CeO_2(0.05)$ are lower than 10 m^2/g, which should be due to the high-temperature calcination of the catalysts (800 °C for 4 h) that lead to the aggregation of the CeO_2 support and the collapse of the pore structure. The surface geometry of $MnO_x/CeO_2(0.05)$ was studied by electron microscopy characterization. As shown in Figure 2A, the bright field-scanning transmission electron microscopy image provides direct observation of the sample, showing stacked CeO_2 crystals [Supplementary Figure 6]. The Mn distribution was identified by the energy dispersive spectroscopy (EDS) elemental maps [Figure 2B-D], showing the MnO_x ensembles with diameters of 15-25 nm on the CeO_2 support, which is different from the Mn-Ce solid solution with homogeneously distributed Mn sites[18], consistent with the XRD results [Figure 1B]. Interestingly, the morphology of the MnO_x ensemble is irregular, which might suggest the amorphous structure of the MnO_x.

Figure 2E shows an enlarged view of the region in the yellow square in Figure 2A. Notably, the crystalline feature of the Mn species is completely unobservable. However, the elemental maps decidedly confirmed the existence of the MnO_x species [Figure 2F-H], demonstrating that the structural feature of $MnO_x/CeO_2(0.05)$ is mainly amorphous MnO_x on the surface of the CeO_2 matrix. The annular bright field-scanning transmission electron microscopy image with atomic resolution clearly shows the distributions of the Ce, O and Mn elements. As shown in Figure 2I-L, the ordered distributions of Ce and O are the same as

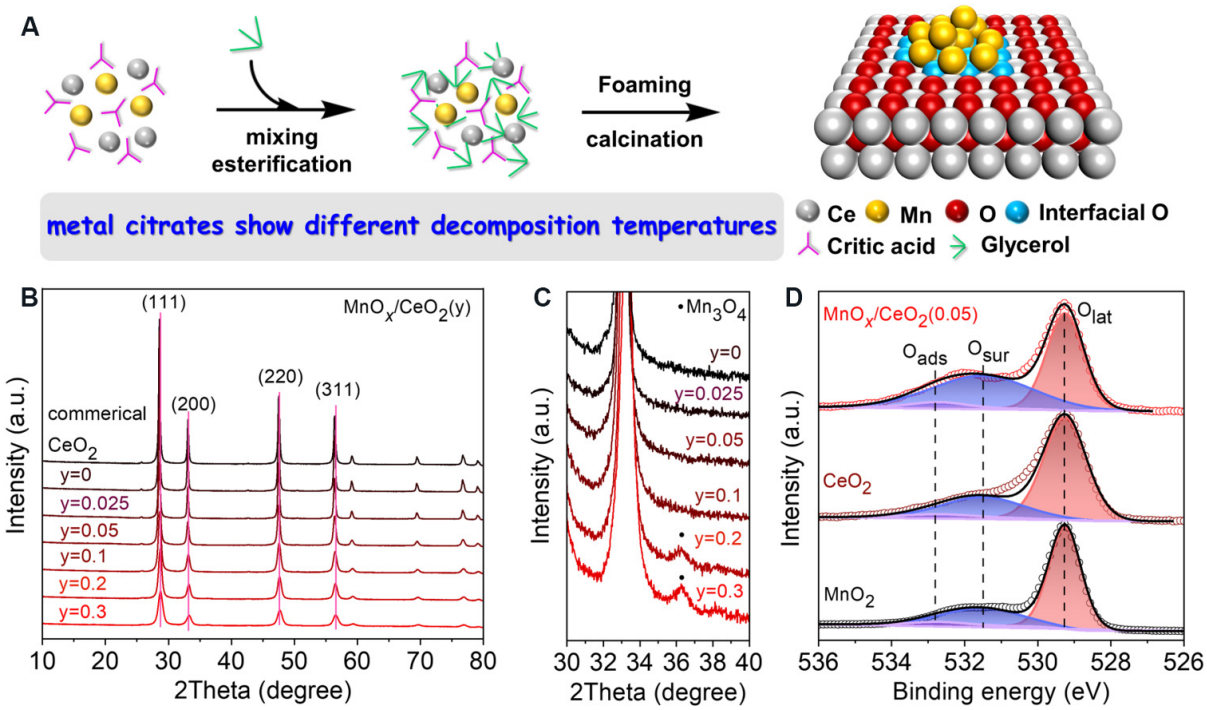

Figure 1. (A) Procedures for synthesizing $MnO_x/CeO_2(y)$ catalyst with MnO_x species anchored on the surface of ceria matrix. (B) XRD patterns of commercial CeO_2 and $MnO_x/CeO_2(y)$ catalysts with different Mn loadings. (C) Zoomed-in views of diffractions peaks in (A) from 30° to 40° for $MnO_x/CeO_2(y)$ catalysts with different Mn loadings. (D) O1s X-ray photoelectron spectra of $MnO_x/CeO_2(0.05)$, CeO_2 and MnO_2. XRD: X-ray diffraction.

those of the CeO_2 lattice. However, the random distribution of Mn confirms the amorphous feature of the MnO_x species. Significantly, the formation of an Mn-Ce solid solution is also excluded, because the smaller ionic radius of manganese ions compared to cerium ions will result in contractive lattice space in the Mn-Ce solid solution compared to the lattice space of CeO_2[18], which is not observed in this work.

The high-resolution HAADF-STEM image of the $MnO_x/CeO_2(0.05)$ catalyst directly shows that the CeO_2 matrix is partially coated with layers with an undetectable lattice [Figure 2M]. In particular, in this case, the catalyst calcined at 800 °C for 4 h precluded the carbon-containing species on the surface of CeO_2. Considering that isolated Ce sites can be found in the amorphous region [Figure 2N], it is reasonable to assign the amorphous layers to the MnO_x species. In addition, the Mn/(Mn + Ce) ratio appears at 0.22 on the catalyst surface by XPS analysis, which is distinctly different from the ratio of 0.05 in the whole oxides, indicating that MnO_x mainly exists on the CeO_2 surface. These results suggest that the structural feature of $MnO_x/CeO_2(0.05)$ is dominated by amorphous MnO_x layers on the surface of the CeO_2 matrix rather than a monophasic solid solution. The unique structure of $MnO_x/CeO_2(0.05)$ can be reasonably assigned to the citric acid-assisted method [Figure 1A], because the remarkably different decomposition temperature of cerium citrate (~161 °C) and manganese citrate (~296 °C) would benefit the phase separation to hinder the formation of the solid solution.

The MnO_x structure was further characterized by Raman and EPR measurements. As shown in Figure 2O and Supplementary Figure 7, the as-synthesized $MnO_x/CeO_2(0.05)$ catalyst shows a blue shift of the MnO_x mode (654 cm^{-1}) compared with that of various manganese oxide and supported MnO_x catalysts prepared by the conventional impregnation method (≤ 640 cm^{-1}), which is due to the SOSIs between MnO_x and the CeO_2 support and the formation of defect-rich MnO_x layers[29-31]. In contrast, the EPR spectrum of the MnO_x

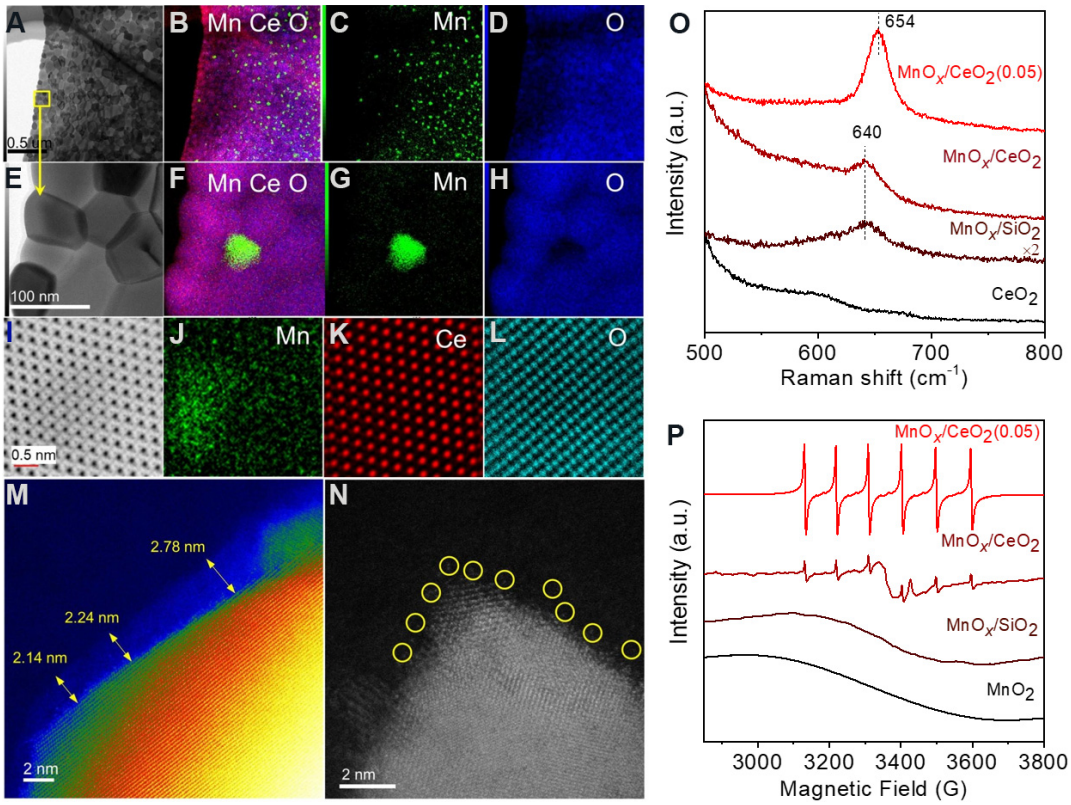

Figure 2. Electron microscopy and structural characterization. (A, E) BF-STEM images and the corresponding (B-D, F-H) Mn, Ce and O elemental maps of MnO_x/CeO_2(0.05). (E) Enlarged view of the yellow square in (A). (I-L) ABF-STEM and EDS analysis of MnO_x/CeO_2(0.05). (M, N) High-resolution STEM images of MnO_x/CeO_2(0.05) catalyst. The isolated Ce sites in the amorphous region are highlighted by yellow circles in (N). (O) Raman and (P) EPR spectra of various samples. BF-STEM: Bright field-scanning transmission electron microscopy; ABF-STEM: annular bright field-scanning transmission electron microscopy.

/CeO_2(0.05) catalyst shows sharp sextuple signals with a *g* value at 2.00 [Figure 2P], indicating the formation of abundant oxygen vacancies by loading of the MnO_x species in the MnO_x/CeO_2(0.05) catalyst[32]. For comparison, the bulky manganese oxide (MnO_2), MnO_x/CeO_2 and MnO_x/SiO_2 prepared by the conventional impregnation method [Supplementary Figure 8] exhibit broad and weak signals in the EPR spectra [Figure 2P], which can be attributed to the Mn-Mn coupling (i.e., aggregation)[33-35]. These results reasonably confirmed the successful formation of well-dispersed and amorphous MnO_x layers on the surface of the ceria matrix and the construction of abundant oxygen vacancies/defective sites in the MnO_x/CeO_2(0.05) catalyst, which are beneficial for the oxygen activation.

Figure 1D shows the O1s X-ray photoelectron spectra of the MnO_x/CeO_2(0.05), CeO_2 and MnO_2 samples. All samples show three peaks at 529.3, 531.4 and 532.7 eV, which can be assigned to the lattice oxygen of O^{2-} (O_{lat}), surface oxygen of O_2^-, O_2^{2-} or O^- (O_{sur}) and adsorbed oxygen species from water/carbonate on the solid surface (O_{ads}), respectively[18,19,28]. In these multiple oxygen species, the surface oxygen species from the defective site with an unsaturated structure displays a key role in the oxidation, which is denoted as active oxygen[18,26]. The atomic ratio of active oxygen to the total oxygen atoms on the oxide surface of CeO_2 and MnO_2 is 26.8% and 28.4%, respectively, while the MnO_x/CeO_2(0.05) exhibited a remarkably improved active oxygen capacity of 46.1% [Supplementary Table 1], which is even comparable to that of Mn-Ce solid solutions (44.1%) with a high Mn loading (50%)[18]. Considering that the MnO_x/CeO_2(0.05) has a low Mn loading (5%) and is mainly presented as amorphous MnO_x layers on the CeO_2 surface, the high capacity of

active oxygen should be due to the maximized interfacial effect, causing the rich Ce^{3+} and Mn^{2+}/Mn^{3+} species [Supplementary Table 1, Figure 2P, Supplementary Figure 9] on the surface to benefit the formation of unsaturated oxygen.

Redox investigation

The redox properties of the active oxygen species on MnO_x/CeO_2(0.05) were firstly identified by the O1s X-ray photoelectron spectrum in a temperature-programmed redox cycle [Figure 3A, Supplementary Figure 10, Supplementary Table 2]. Hydrogen treatments at low temperature (room temperature to 80 °C) partially reduced the surface oxygen sites, as evidenced by the decreased intensity of the O1s peak of O_{sur} (531.4 eV) (Figure 3A and its inset), indicating that active oxygen species were available at low temperature. The subsequent reduction at the higher temperature of 120 °C led to further removal of the active oxygen. Very importantly, the active oxygen can be regenerated after treatment in air at 50 °C, displaying a similar O1s X-ray photoelectron spectrum to that of the as-synthesized sample (Figure 3A and its inset). Therefore, the high activity and remarkable stability of MnO_x/CeO_2(0.05) in the catalytic oxidation at low temperatures are reasonably expected.

Further evidence regarding the redox properties of the active oxygen species is provided by *in-situ* Raman spectroscopy. As shown in Supplementary Figure 11, MnO_x/CeO_2(0.05) gives the F_{2g} mode of the CeO_2 matrix at 460 cm^{-1}[23,30,36]. Compared to the spectrum of CeO_2, MnO_x/CeO_2(0.05) shows an additional band at 656 cm^{-1} [Figure 3B], which is associated with the Mn-O-Mn stretching mode of the surface amorphous MnO_x species with abundant defects[29-31], corresponding to the active oxygen in the X-ray photoelectron spectra [Figure 3A]. Notably, broadening, a decrease in intensity and a red shift of the band at 656 cm^{-1} occurred during the *in-situ* treatment of MnO_x/CeO_2(0.05) in atmospheric Ar at 140 °C. The intensity of the band at 645 cm^{-1} was further decreased when the temperature increased to 250 and 350 °C in Ar. This can be well explained by the desorption of the active oxygen species associated with MnO_x species to form Mn sites with more defects[20,23]. Considering the well-dispersed, amorphous and layered structure of the MnO_x species, it can be reasonably inferred that the desorption of the interfacial oxygen species accounts for the signal changes. To probe the reversibility of the active oxygen at low temperature, we exposed the sample to molecular oxygen at room temperature, resulting in a very similar Raman spectrum to the as-synthesized MnO_x/CeO_2(0.05) sample, thereby confirming the reversibility of active oxygen species [Figure 3B, Supplementary Figure 12], in good agreement with the *in-situ* XPS results [Figure 3A]. The active oxygen on MnO_x/CeO_2(0.05) was further evidenced by the O_2-TPD test [Supplementary Figure 13]. The active and reproducible oxygen species over MnO_x/CeO_2(0.05) make it a potentially efficient catalyst for aerobic oxidation reactions.

In order to support this conclusion, we further evaluated the catalytic performance of the MnO_x/CeO_2(0.05) catalyst for the CO oxidation reaction, where the activation of oxygen molecules is regarded as a key step[37,38]. Figure 4A shows the dependence of CO conversion on temperature over the MnO_x/CeO_2(0.05) and CeO_2 catalysts. The positive role of the interfacial effect on MnO_x/CeO_2(0.05) is evidenced by the full conversion of CO over MnO_x/CeO_2(0.05) at a lower temperature (270 °C) than that over CeO_2 (370 °C). By correlating the inverse of the absolute temperature (1/T) with the initial reaction rates, the apparent activation energies of MnO_x/CeO_2(0.05) and CeO_2 appeared at 51.4 and 69.2 kJ/mol, respectively [Figure 4B]. The relatively lower apparent activation energy of MnO_x/CeO_2(0.05) indicates that CO oxidation is easier. Based on the understanding that the activation energy is sensitive to the different active oxygen[37,39], a lower apparent activation energy of MnO_x/CeO_2(0.05) than that of CeO_2 should be reasonably attributed to the abundant Mn-O-Ce interfacial sites to activate O_2, rather than simply increasing the number of active oxygen species. Figure 4C shows the dependence of the reaction rate on oxygen partial pressure over different catalysts, where MnO_x/CeO_2(0.05) always displays higher reaction rates than CeO_2 at

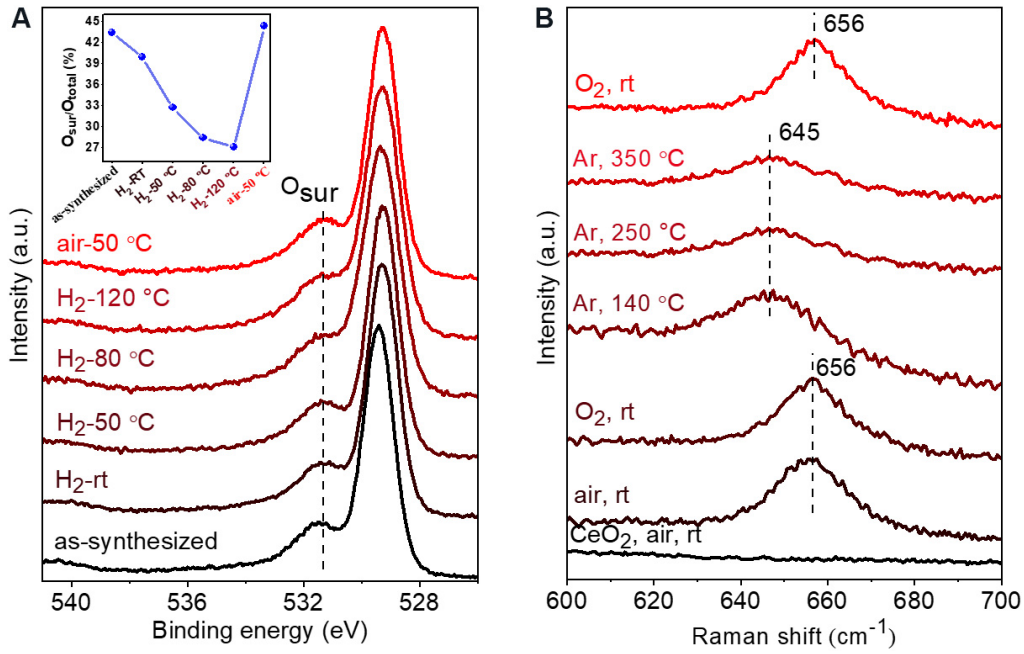

Figure 3. Redox study. (A) *In-situ* O1s X-ray photoelectron spectra of MnO_x/CeO_2(0.05) under different redox conditions. Inset: the dependences of O_{sur} capacities on redox conditions. (B) *In-situ* Raman spectra of MnO_x/CeO_2(0.05) and CeO_2 under different conditions.

the same oxygen pressure, thereby demonstrating its higher activities. Interestingly, under relatively low oxygen pressure (1.0-3.5 kPa), the reaction rates (r_0) over CeO_2 increased constantly with oxygen pressure, showing the reaction kinetic order at 0.37 [Figure 4D]. In contrast, the influence of oxygen pressure on the r_0 of MnO_x/CeO_2(0.05) is minimal with a kinetic order at 0.04 [Figure 4D]. A lower reaction kinetic order suggests that the activity of MnO_x/CeO_2(0.05) is insensitive to the oxygen pressure[37,40], which is reasonably attributed to the enhanced ability of the well-dispersed and amorphous MnO_x species in MnO_x/CeO_2(0.05) to activate molecular oxygen efficiently. These results indicate that the proof-of-concept design of the catalyst benefits the enhancement of catalytic efficacy in aerobic oxidations.

Aerobic oxidation of hydrocarbons

Initial attempts to evaluate the catalysts were performed in the selective oxidation of ethylbenzene to acetophenone and 1-phenylethanol at a low temperature of 110 °C for 6 h without solvent and initiator additives [Table 1]. A higher molar ratio of acetophenone and 1-phenylethanol indicates the deep dehydrogenation of 1-phenylethanol to acetophenone. The blank run without catalysts showed undetected reactivity (entry 1). The commercial nanosized CeO_2, MnO_2 and CeO_2 were active for the reaction, giving ethylbenzene conversion at 3.0%, 1.3% and 6.8%, respectively (entries 2-4). The Mn salts of $MnCl_2$ and $KMnO_4$, which are well-known homogeneous catalysts in oxidation, gave ethylbenzene conversion at 8.2% and 1.9%, respectively (entries 5 and 6). Interestingly, interfacing MnO_x on CeO_2 significantly influenced the catalytic activity, where enhanced conversions were achieved over the MnO_x/CeO_2 catalysts (entries 7-11). By optimizing the Mn loadings on the catalysts, the best performance was achieved over MnO_x/CeO_2(0.05) with the highest capacity of active surface oxygen, displaying ethylbenzene conversion at 12.9% (entry 8). The decreased activity for the MnO_x/CeO_2 catalysts with an Mn/(Mn + Ce) ratio higher than 0.05 is due to the aggregation of the MnO_x species [Figure 1C], leading to limited Mn-O-Ce interfacial sites for the oxidation of substrates. Very interestingly, the oxidation of ethylbenzene can be performed at a low temperature at 70 °C (entry 14), demonstrating the superior catalytic activity of MnO_x/CeO_2(0.05).

Table 1. Catalytic data in oxidation of ethylbenzene[a]

Entry	Catalyst	Temp. (°C)	Time (h)	Conv. (%)	Sel. (%)	A/P[b]
1	Blank	110.0	6.0	< 0.1	n.d.	n.d.
2	Commercial CeO_2	110.0	6.0	3.0	> 99.0	0.8
3	MnO_2	110.0	6.0	1.3	> 99.0	0.6
4	CeO_2	110.0	6.0	6.8	> 99.0	1.1
5[c]	$MnCl_2$	110.0	6.0	8.2	97.6	2.6
6[c]	$KMnO_4$	110.0	6.0	1.9	94.7	2.0
7	MnO_x/CeO_2(0.025)	110.0	6.0	9.2	> 99.0	1.2
8	MnO_x/CeO_2(0.05)	110.0	6.0	12.9	> 99.0	1.9
9	MnO_x/CeO_2(0.1)	110.0	6.0	7.1	> 99.0	0.7
10	MnO_x/CeO_2(0.2)	110.0	6.0	5.6	> 99.0	0.4
11	MnO_x/CeO_2(0.3)	110.0	6.0	4.1	> 99.0	0.5
12	MnO_x/CeO_2(0.05)	110.0	16.0	27.1	> 99.0	2.1
13	MnO_x/CeO_2(0.05)	110.0	24.0	29.4	> 99.0	2.6
14	MnO_x/CeO_2(0.05)	70.0	6.0	0.7	> 99.0	0.8
15	MnO_x/CeO_2(0.05)	90.0	6.0	4.3	> 99.0	1.5
16	MnO_x/CeO_2(0.05)	130.0	6.0	24.2	> 99.0	2.0
17	MnO_x/CeO_2(0.05)	130.0	24.0	34.7	> 99.0	1.9
18	MnO_x/CeO_2(0.05), 200 mg	130.0	24.0	52.8	> 99.0	3.4
19	MnO_x/CeO_2(0.05), 400 mg	130.0	24.0	59.2	> 99.0	7.0
20	MnO_x/CeO_2(0.05), 400 mg, 3 MPa of O_2	130.0	24.0	63.5	95.7	5.8
21	MnO_x/CeO_2(0.05), 600 mg, 3 MPa of O_2	130.0	24.0	65.6	77.6	4.7
22[d]	MnO_x/CeO_2	130.0	24.0	19.2	> 99.0	16
23	MnO_x/CeO_2(0.05), 2 MPa of N_2	110.0	6.0	< 0.1	n.d.	n.d.
24	MnO_x/CeO_2(0.05), 50 mg of hydroquinone	110.0	6.0	< 0.1	n.d.	n.d.

[a]Reaction conditions: 47 mmol of substrate, 100 mg of catalyst, 2.0 MPa of oxygen; [b]A/P: molar ratio of acetophenone and 1-phenylethanol; [c]Molar weight of the Mn in the catalyst is the same as the molar weight of Mn in MnO_x/CeO_2(0.05); [d]Catalyst prepared from conventional impregnation method. Conv.: Conversion; Sel.: selectivity to acetophenone and 1-phenylethanol; n.d.: not detected.

To realize the best performance, we optimized the reaction temperature, time, catalyst amount and oxygen pressure in the reactor (entries 12-21). The ethylbenzene conversion of 59.2% with > 99.0% selectivity to acetophenone and 1-phenylethanol was achieved (entry 19). This result, obtained under solvent- and initiator-free conditions, even outperforms a series of superior catalysts for C-H bond selective oxidations reported in the literature [Supplementary Table 3], such as the Au nanosheet with undetectable reactivity under solvent- and initiator-free conditions[12]. The MnO_x/CeO_2 catalyst synthesized from the conventional impregnation method with the same Mn loading to MnO_x/CeO_2(0.05) exhibited poor activity (entry 22), which might be due to the aggregation of the MnO_x particles and the limited interfacial sites, as confirmed by the Raman and EPR analysis [Figure 2O and P]. Increasing the MnO_x/CeO_2(0.05) catalyst amount led to enhanced ethylbenzene conversion but unsatisfactory carbon balance values because of the over-oxidation to CO and CO_2 (entries 20 and 21, Supplementary Figure 14). The molecular oxygen indeed acted as oxygen donors in the reaction, as evidenced by the undetectable conversion of ethylbenzene when using nitrogen instead of oxygen in the reaction (entry 23). When the free radical scavenger was added to the reaction system, the reaction was quenched, demonstrating that the reaction follows a radical chain mechanism (entry 24).

More importantly, the catalyst is stable, reusable and can be easily filtrated and recycled after each reaction run. Consequently, it exhibited stable catalytic performance in the recycling tests

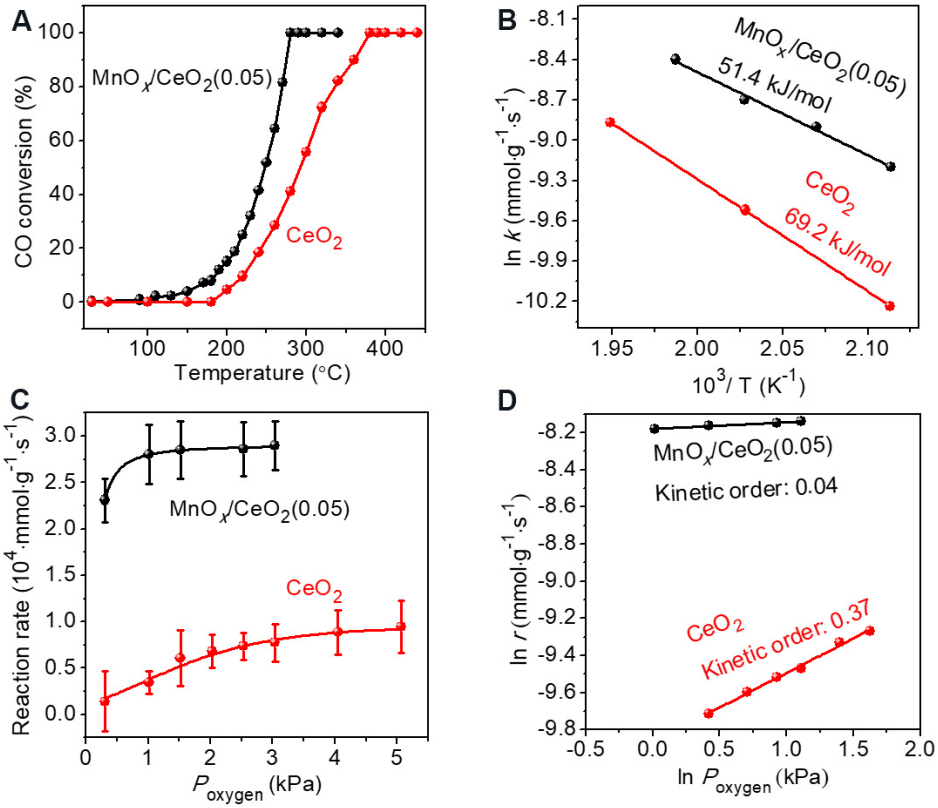

Figure 4. CO oxidation. (A) Dependence of CO conversion on temperature over MnO_x/CeO_2(0.05) and CeO_2 catalysts. (B) Arrhenius plots of CO oxidation over MnO_x/CeO_2(0.05) and CeO_2 catalysts. (C) Dependence of reaction rate on oxygen pressure in CO oxidation over MnO_x/CeO_2(0.05) and CeO_2 catalysts. (D) Data characterizing the kinetic reaction order of oxygen in CO oxidation over MnO_x/CeO_2(0.05) and CeO_2 catalysts.

[Supplementary Figure 15]. In the six runs of selective ethylbenzene oxidation, the MnO_x/CeO_2(0.05) catalyst exhibited constant conversion and selectivity, indicating good recyclability and stability. Notably, the MnO_x/CeO_2(0.05) catalyst is generally effective for the selective oxidation of various phenolic hydrocarbons [Supplementary Table 4], giving desired products with good activities and selectivities. It is noteworthy that these reactions were all performed under solvent- and initiator-free conditions, which make the MnO_x/CeO_2(0.05) catalyst potentially useful for wide applications in the selective oxidation of C-H bonds.

Mechanism investigation

Based on the aforementioned results, we conclude that MnO_x/CeO_2(0.05) is highly active for the selective oxidation of C-H bonds under solvent- and initiator-free conditions at low temperature based on its earth-abundant metals as catalysts and constructing SOSIs. In contrast to the existing understanding that highly active Mn-Ce catalysts should be dominated by the solid-solution phase, the greatest difference in our case is that MnO_x/CeO_2(0.05) has separated phases of two-dimensional and amorphous MnO_x layers on CeO_2. We conclude that the high efficacy of MnO_x/CeO_2(0.05) originates from the SOSIs and maximized interfacial effects, because a highly active solid-solution catalyst requires a high Mn concentration (~50%)[18].

In order to further address this conclusion, we performed acid treatment for MnO_x/CeO_2(0.05) to partially remove the surface MnO_x species, as confirmed by the X-ray photoelectron spectra giving the surface Mn/(Mn + Ce) ratio decreased from 0.22 to almost undetectable [Figure 5A]. The acid-treated

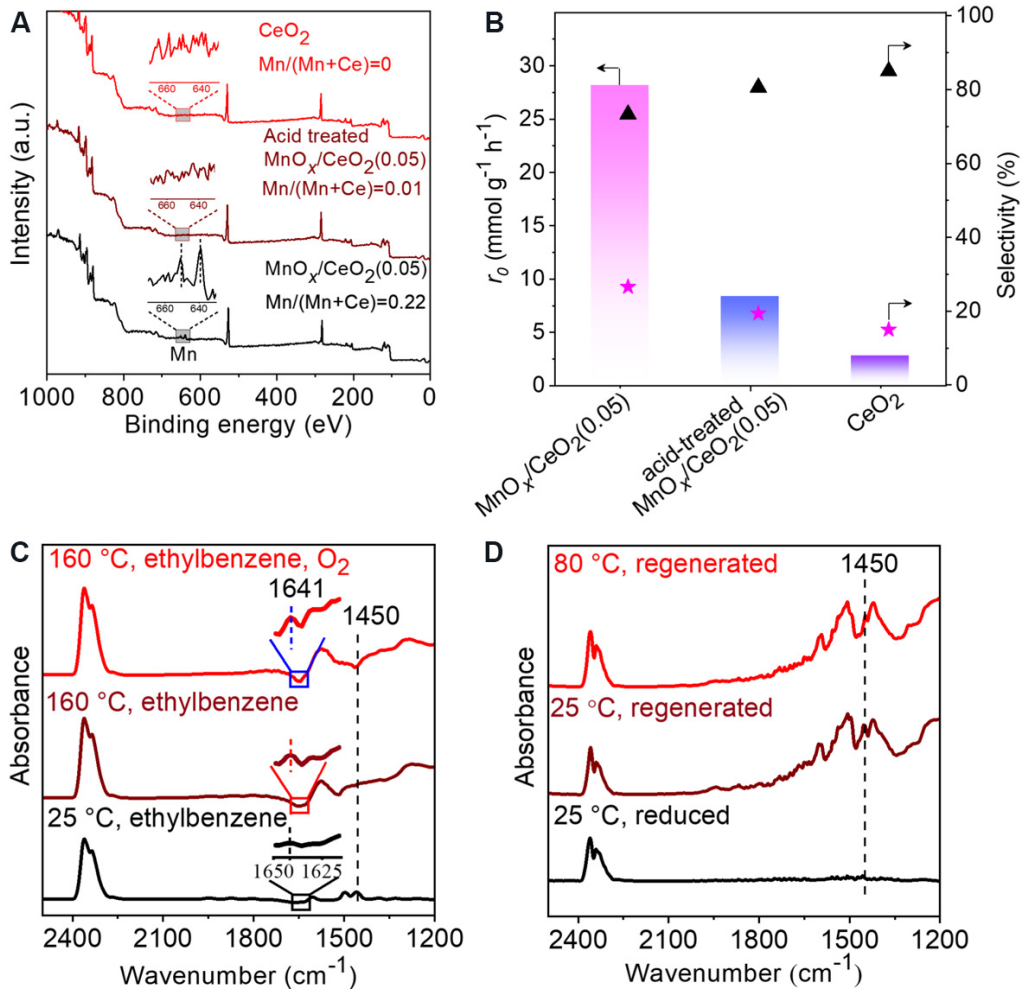

Figure 5. Mechanism studies. (A) X-ray photoelectron spectra of MnO_x/CeO_2(0.05), acid-treated MnO_x/CeO_2(0.05) and CeO_2. (B) Reaction rate and product selectivities in ethylbenzene oxidation over various catalysts. The triangles and stars represent the selectivities to 1-phenylethanol and acetophenone, respectively. (C) *In-situ* FTIR spectra of ethylbenzene adsorbed on MnO_x/CeO_2(0.05) at 25 and 160 °C in flowing Ar and then switched to O_2. (D) *In-situ* FTIR spectra of ethylbenzene adsorbed on H_2-reduced MnO_x/CeO_2(0.05) at 25 °C, O_2-regenerated MnO_x/CeO_2(0.05) at 25 °C and 80 °C. FTIR: Fourier transform infrared.

MnO_x/CeO_2(0.05) exhibited a significantly reduced ethylbenzene conversion rate (8 mmol g^{-1} h^{-1}) compared to the fresh catalyst (28 mmol g^{-1} h^{-1}) [Figure 5B] under equivalent reaction conditions, demonstrating the important role of the surface MnO_x species of MnO_x/CeO_2(0.05) in generating abundant interfacial active sites. In order to understand the role of active oxygen on MnO_x/CeO_2(0.05) for C-H bond oxidation, we performed *in-situ* FTIR spectroscopy studies of C-H bond oxidation. Figure 5C shows the ethylbenzene-adsorption FTIR spectrum of MnO_x/CeO_2(0.05), which gives the typical peak at 1450 cm^{-1} assigned to the C-H bond[18]. By increasing the temperature to 160 °C in flowing Ar, the C-H peak was remarkably weakened, which should be due to the activation of the C-H bond by the surface oxygen species on the MnO_x/CeO_2(0.05) catalyst, because the hydrocarbon favors reacting with the active surface oxygen with an asymmetric Coulombic interaction with Mn and Ce[18,20]. Meanwhile, the readily observed C=O bond at 1641 cm^{-1} confirmed that the C-H bonds are indeed oxidized by the active oxygen on the solid surface into C=O species[18]. The introduction of external molecular oxygen further enhanced the transformation of the C-H bonds at 160 °C, as evidenced by the increased intensity of the C=O peak at 1641 cm^{-1}.

The aforementioned results demonstrate the important role of the active oxygen species on the $MnO_x/CeO_2(0.05)$ catalyst in activating C-H bonds. After purging $MnO_x/CeO_2(0.05)$ with hydrogen to reduce the active oxygen at 200 °C, the system was switched to the Ar flow with ethylbenzene molecules at 25 °C. The reduced $MnO_x/CeO_2(0.05)$ failed to adsorb ethylbenzene, as confirmed by the undetectable peak of C-H bonds in the *in-situ* FTIR spectrum [Figure 5D]. Furthermore, after regeneration of the active oxygen, the adsorption of C-H bonds occurred again on the regenerated catalyst at 25 °C. Increasing the temperature to 80 °C led to a significant weakening of the C-H bonds, confirming that they were readily activated by the regenerated active oxygen species. These phenomena demonstrate the important role of active oxygen in the adsorption and activation of C-H bonds.

CONCLUSIONS

In summary, we have demonstrated a ceria-supported two-dimensional manganese oxide with a SOSI effect as an efficient catalyst for the selective oxidation of hydrocarbons, thereby breaking the normal principle of synthesizing Mn-Ce catalysts with an abundant solid-solution phase. The key to the success is to anchor well-dispersed and amorphous MnO_x layers on the CeO_2 matrix by SOSIs, forming abundant active oxygen species over $MnO_x/CeO_2(0.05)$ because of the high interfacial efficacy, which displays crucial roles in the adsorption and activation of C-H bonds. In the selective oxidation of hydrocarbons to the corresponding alcohols and ketones, $MnO_x/CeO_2(0.05)$ exhibited high activity, selectivity and recyclability under solvent- and initiator-free conditions at low temperature, outperforming the noble catalysts and the state-of-the-art Mn-Ce metal oxide catalysts. This work not only highlights the importance of SOSIs for the oxidation of C-H bonds but also extends the principle for designing efficient metal oxide catalysts for the sustainable production of valuable chemicals.

DECLARATIONS

Authors' contributions

Carried out the catalyst preparation, characterization, catalytic tests, and prepared the draft manuscript: Wang H

Performed part of the catalyst characterization: Luo Q, Zhang J, Wang C

Performed the TEM characterization: Ge X, Zhang W

Planned the study, analysed the data and wrote the manuscript: Wang L, Xiao FS

Availability of data and materials

Not applicable.

Financial support and sponsorship

This work is supported by National Natural Science Foundation of China (21822203 and 21932006), China National Postdoctoral Program for Innovative Talent (BX2021256), China Postdoctoral Science Foundation (2021M700119), and 2020 International Cooperation Project of the Department of Science and Technology of Jilin Province (20200801001GH).

Conflict of interest

All authors declared that there are no conflicts of interest.

Ethical approval and consent to participate

Not applicable.

Consent for publication

Not applicable.

REFERENCES

1. White MC. Chemistry. Adding aliphatic C-H bond oxidations to synthesis. *Science* 2012;335:807-9. DOI PubMed
2. ten Brink GJ, Arends IW, Sheldon RA. Green, catalytic oxidation of alcohols in water. *Science* 2000;287:1636-9. DOI PubMed
3. Marimuthu A, Zhang J, Linic S. Tuning selectivity in propylene epoxidation by plasmon mediated photo-switching of Cu oxidation state. *Science* 2013;339:1590-3. DOI PubMed
4. Liu W, Zhang L, Liu X, et al. Discriminating catalytically active FeN_x species of atomically dispersed Fe-N-C catalyst for selective oxidation of the C-H bond. *J Am Chem Soc* 2017;139:10790-8. DOI PubMed
5. Kulangiappar K, Anbu Kulandainathan M, Raju T. Conversion of benzylic bromides to benzaldehydes using sodium nitrate as an oxidant. *Ind Eng Chem Res* 2010;49:6670-3. DOI
6. Frei H. Chemistry. Selective hydrocarbon oxidation in zeolites. *Science* 2006;313:309-10. DOI PubMed
7. Hughes MD, Xu YJ, Jenkins P, et al. Tunable gold catalysts for selective hydrocarbon oxidation under mild conditions. *Nature* 2005;437:1132-5. DOI PubMed
8. Pradhan S, Bartley JK, Bethell D, et al. Non-lattice surface oxygen species implicated in the catalytic partial oxidation of decane to oxygenated aromatics. *Nat Chem* 2012;4:134-9. DOI PubMed
9. Yuan C, Liang Y, Hernandez T, Berriochoa A, Houk KN, Siegel D. Metal-free oxidation of aromatic carbon-hydrogen bonds through a reverse-rebound mechanism. *Nature* 2013;499:192-6. DOI PubMed
10. Zope BN, Hibbitts DD, Neurock M, Davis RJ. Reactivity of the gold/water interface during selective oxidation catalysis. *Science* 2010;330:74-8. DOI PubMed
11. Fu Q, Li WX, Yao Y, et al. Interface-confined ferrous centers for catalytic oxidation. *Science* 2010;328:1141-4. DOI PubMed
12. Wang L, Zhu Y, Wang JQ, et al. Two-dimensional gold nanostructures with high activity for selective oxidation of carbon-hydrogen bonds. *Nat Commun* 2015;6:6957. DOI PubMed PMC
13. Liu Y, Tsunoyama H, Akita T, Xie S, Tsukuda T. Aerobic oxidation of cyclohexane catalyzed by size-controlled Au clusters on hydroxyapatite: size effect in the sub-2 nm regime. *ACS Catal* 2011;1:2-6. DOI
14. Turner M, Golovko VB, Vaughan OP, et al. Selective oxidation with dioxygen by gold nanoparticle catalysts derived from 55-atom clusters. *Nature* 2008;454:981-3. DOI PubMed
15. Neufeldt SR, Sanford MS. Controlling site selectivity in palladium-catalyzed C-H bond functionalization. *Acc Chem Res* 2012;45:936-46. DOI PubMed PMC
16. Muzart J. Ionic liquids as solvents for catalyzed oxidations of organic compounds. *Adv Synth Catal* 2006;348:275-95. DOI
17. Qi G, Yang RT, Chang R. MnO_x-CeO_2 mixed oxides prepared by co-precipitation for selective catalytic reduction of NO with NH_3 at low temperatures. *Appl Catal B* 2004;51:93-106. DOI
18. Zhang P, Lu H, Zhou Y, et al. Mesoporous $MnCeO_x$ solid solutions for low temperature and selective oxidation of hydrocarbons. *Nat Commun* 2015;6:8446. DOI PubMed PMC
19. Venkataswamy P, Rao KN, Jampaiah D, Reddy BM. Nanostructured manganese doped ceria solid solutions for CO oxidation at lower temperatures. *Appl Catal B* 2015;162:122-32. DOI
20. Zou Z, Meng M, Zha Y. Surfactant-assisted synthesis, characterizations, and catalytic oxidation mechanisms of the mesoporous MnO_x-CeO_2 and Pd/MnO_x-CeO_2 catalysts used for CO and C_3H_8 oxidation. *J Phys Chem C* 2010;114:468-77. DOI
21. Elias JS, Risch M, Giordano L, Mansour AN, Shao-Horn Y. Structure, bonding, and catalytic activity of monodisperse, transition-metal-substituted CeO_2 nanoparticles. *J Am Chem Soc* 2014;136:17193-200. DOI PubMed
22. Wang C, Wen C, Lauterbach J, Sasmaz E. Superior oxygen transfer ability of Pd/MnO_x-CeO_2 for enhanced low temperature CO oxidation activity. *Appl Catal B* 2017;206:1-8. DOI
23. Zhang X, Deng Y, Tian P, Shang H, Xu J, Han Y. Dynamic active sites over binary oxide catalysts: In situ/operando spectroscopic study of low-temperature CO oxidation over MnO_x-CeO_2 catalysts. *Appl Catal B* 2016;191:179-91. DOI
24. Delimaris D, Ioannides T. VOC oxidation over MnO_x-CeO_2 catalysts prepared by a combustion method. *Appl Catal B* 2008;84:303-12. DOI
25. Cen W, Liu Y, Wu Z, Wang H, Weng X. A theoretic insight into the catalytic activity promotion of CeO_2 surfaces by Mn doping. *Phys Chem Chem Phys* 2012;14:5769-77. DOI PubMed
26. Wang Z, Shen G, Li J, Liu H, Wang Q, Chen Y. Catalytic removal of benzene over CeO_2-MnO_x composite oxides prepared by hydrothermal method. *Appl Catal B* 2013;138-139:253-9. DOI
27. Tang X, Chen J, Huang X, Xu Y, Shen W. Pt/MnO_x-CeO_2 catalysts for the complete oxidation of formaldehyde at ambient temperature. *Appl Catal B* 2008;81:115-21. DOI
28. Quiroz J, Giraudon J, Gervasini A, et al. Total oxidation of formaldehyde over MnO_x-CeO_2 catalysts: the effect of acid treatment. *ACS Catal* 2015;5:2260-9. DOI
29. Li X, Lunkenbein T, Pfeifer V, et al. Selective alkane oxidation by manganese oxide: site isolation of MnO_x chains at the surface of

$MnWO_4$ nanorods. *Angew Chem Int Ed Engl* 2016;55:4092-6. DOI PubMed

30. Lin X, Li S, He H, et al. Evolution of oxygen vacancies in MnO_x-CeO_2 mixed oxides for soot oxidation. *Appl Catal B* 2018;223:91-102. DOI
31. Xu J, Li P, Song X, He C, Yu J, Han Y. Operando raman spectroscopy for determining the active phase in one-dimensional $Mn_{1-x}Ce_xO_{2\pm y}$ nanorod catalysts during methane combustion. *J Phys Chem Lett* 2010;1:1648-54. DOI
32. Figaj M, Becker K. An electron paramagnetic resonance study of impurities in ceria, CeO_2. *Solid State Ionics* 2001;141-142:507-12. DOI
33. Yang X, Pu C, Qin H, Liu S, Xu Z, Peng X. Temperature- and Mn^{2+} concentration-dependent emission properties of Mn^{2+}-doped ZnSe nanocrystals. *J Am Chem Soc* 2019;141:2288-98. DOI PubMed
34. Kurz T, Chen L, Brieler FJ, et al. Minimal number of atoms to constitute a magnet: Suppression of magnetic order in spherical MnS nanoparticles. *Phys Rev B* 2008;78:132408. DOI
35. Goede O, Backs D, Heimbrodt W, Kanis M. EPR study of the antiferromagnetic phase transition in (Cd, Mn)S. *phys stat sol (b)* 1989;151:311-8. DOI
36. Sato T, Komanoya T. Selective oxidation of alcohols with molecular oxygen catalyzed by Ru/MnO/CeO_2 under mild conditions. *Catalysis Communications* 2009;10:1095-8. DOI
37. Xie X, Li Y, Liu ZQ, Haruta M, Shen W. Low-temperature oxidation of CO catalysed by Co(3)O(4) nanorods. *Nature* 2009;458:746-9. DOI PubMed
38. Chen G, Zhao Y, Fu G, et al. Interfacial effects in iron-nickel hydroxide-platinum nanoparticles enhance catalytic oxidation. *Science* 2014;344:495-9. DOI PubMed
39. Gu D, Tseng JC, Weidenthaler C, et al. Gold on different manganese oxides: ultra-low-temperature CO oxidation over colloidal gold supported on bulk-MnO_2 nanomaterials. *J Am Chem Soc* 2016;138:9572-80. DOI PubMed
40. Yu WZ, Wang WW, Li SQ, et al. Construction of active site in a sintered copper-ceria nanorod catalyst. *J Am Chem Soc* 2019;141:17548-57. DOI PubMed

Matlin. *Chem Synth* 2022;2:3
DOI: 10.20517/cs.2022.06

Chemical Synthesis

News

Open Access

Press statement: Vivian Wing-Wah YAM appointed president of IOCD

Stephen A. Matlin*

Institute of Global Health Innovation, Faculty Building, South Kensington Campus, Imperial College London, South Kensington, London SW7 2AZ, UK.

***Correspondence to:** Prof. Stephen A. Matlin, Institute of Global Health Innovation, Faculty Building, South Kensington Campus, Imperial College London, South Kensington, London SW7 2AZ, UK. E-mail: s.matlin@imperial.ac.uk

How to cite this article: Matlin SA. Press statement: Vivian Wing-Wah YAM appointed president of IOCD. *Chem Synth* 2022;2:3. https://dx.doi.org/10.20517/cs.2022.06

Received: 14 Mar 2022 **Accepted:** 15 Mar 2022 **Published:** 21 Mar 2022

Academic Editor: Bao-Lian Su **Copy Editor:** Jia-Xin Zhang **Production Editor:** Jia-Xin Zhang

Professor Vivian Wing-Wah YAM [Figure 1] from Hong Kong, China, has been elected as the next President of the International Organization for Chemical Sciences in Development (IOCD).

Professor Yam is IOCD's first woman President. She follows in the footsteps of the two outstanding scientists who have previously held this position: IOCD's founding President, the Nobel Laureate Glenn T. Seaborg (USA), served from 1981 until 1992, when he was succeeded by the Nobel Laureate Jean-Marie Lehn (France), who stepped down at the end of 2021.

Professor Yam is an elected Member of the Chinese Academy of Sciences (2001), Fellow of The World Academy of Sciences (2006), International Member of the US National Academy of Sciences (2012), Foreign Member of Academia Europaea (2015), and Founding Member of the Hong Kong Academy of Sciences (2015). Educated in chemistry at the University of Hong Kong (HKU) and receiving BSc (1985) and Ph.D. (1988) degrees, Professor Yam is Philip Wong Wilson Wong Professor in Chemistry and Energy at HKU, where she has served as Head of Chemistry (2000-05) and, since 2021, Interim Dean of Science. Her research work focuses on inorganic/organometallic syntheses, supramolecular chemistry, photophysics and photochemistry, and metal-based molecular functional materials.

Figure 1. Professor Vivian Wing-Wah YAM. (Retrieved from: http://web.hku.hk/~wwyam/yam/homepage/)

Professor Yam's career has been marked by many major awards for her highly distinguished scientific contributions, among which she is a Laureate of the *UNESCO-L'Oréal Award for Women in Science* (2011). In 2020 she was awarded the Porter Medal by the European Photochemistry Association, the Inter-American Photochemistry Society and the Asian and Oceanian Photochemistry Association, for her contributions to photochemistry; and in 2021, she was honoured with designation as the inaugural *Pioneer in Energy Research* by ACS Energy and Fuels and has had a Special Issue of this journal dedicated to her.

Professor Yam has shown great dedication to sustainable development and to advancing the role of women in science. Both of these are core to IOCD's mission, to promote the central role of the chemical sciences in meeting the great challenges that the world faces in the 21st Century - in particular, in achieving a sustainable and equitable future for all. Professor Yam has also been a strong supporter of the role of women in science, and her election as President follows the recent appointment of other new women Members, so that women now form the majority on IOCD's governing body for the first time in its history.

DECLARATIONS

Authors' contributions

The author contributed solely to the article.

Availability of data and materials

Not applicable.

Financial support and sponsorship

None.

Conflicts of interest

The author declared that there are no conflicts of interest.

Ethical approval and consent to participate

Not applicable.

Consent for publication

Not applicable.

Su. *Chem Synth* 2022;2:4
DOI: 10.20517/cs.2022.08

Chemical Synthesis

Editor's Choice

Open Access

Amazing circularly polarized luminescence in inorganic materials

Bao-Lian Su[1,2,*]

[1]State Key Laboratory of Advanced technology for Materials Synthesis and Processing, Wuhan University of Technology, Wuhan 430074, Hubei, China.
[2]Laboratory of Inorganic Materials Chemistry, University of Namur, Namur B-5000, Belgium.

***Correspondence to:** Prof. Bao-Lian Su, Laboratory of Inorganic Materials Chemistry, University of Namur, Rue de Bruxelles 61, Namur B-5000, Belgium. E-mail: bao-lian.su@unamur.be

How to cite this article: Su BL. Amazing circularly polarized luminescence in inorganic materials. *Chem Synth* 2022;2:4. https://dx.doi.org/10.20517/cs.2022.08

Received: 22 March 2022 **Accepted**: 22 March 2022 **Published:** 25 March 2022

Academic Editor: Bao-Lian Su **Copy Editor:** Jia-Xin Zhang **Production Editor:** Jia-Xin Zhang

Circularly polarized luminescence (CPL) is an amazing optical event specifically arising from chiral luminescent materials, which preferably emit either left-handed or right-handed circularly polarized light. CPL-active materials will find broad applications in many areas such as laser sources, 3D display, anti-counterfeiting, and bioimaging[1-3]. In recent years, the development of CPL-active materials has become an active interdisciplinary topic across the fields of chirality and optics[4]. Chirality is one prerequisite for CPL, and most CPL-active materials are traditionally constructed by using organic matter[5], partially due to the long history of chirality research in organic chemistry. Nevertheless, chirality is not limited to organic substances but is also found in natural and synthetic inorganic matter. Especially, great advances have been achieved on sophisticated synthesis strategies of chiral inorganic materials in the past decade[6]. As a result, the design of CPL-active systems using inorganic substances has gained increasing attention, which is significant to expand the scope of CPL-active materials.

In this issue of *Chemical Synthesis*, Liu *et al.*[7] gave an overview of nascent topics on CPL generated by inorganic materials [Figure 1]. In this review, the authors firstly introduced the basics of CPL, and subsequently summarized three common construction strategies for inorganics-associated CPL-active materials, including: (1) inorganic luminophores with intrinsically chiral structures; (2) inorganic luminophores with chiroptical activity induced by chiral organic ligands; (3) chiral inorganic nanomaterials

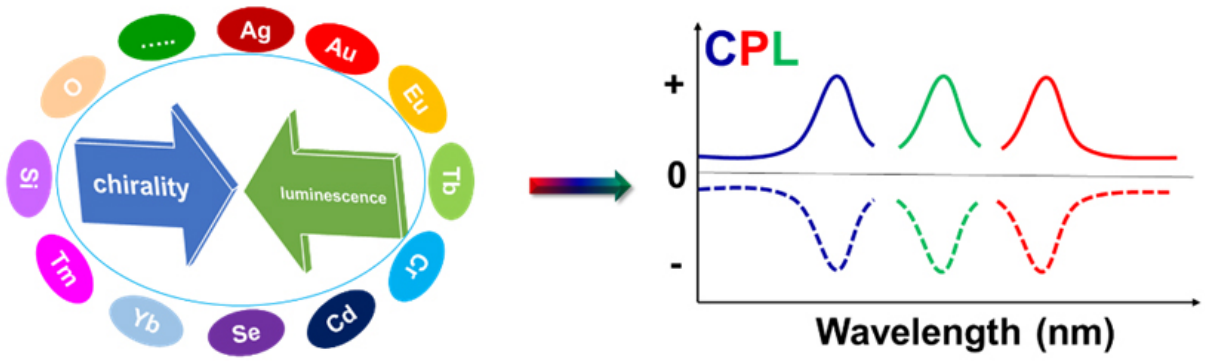

Figure 1. Schematic of CPL spectra generated by various inorganic matter through the combination of chirality and luminescence. CPL: Circularly polarized luminescence.

combined with luminophores.

The above construction methodologies are further clarified in the following two aspects: 1) endowing common inorganic luminophores with CPL, which are demonstrated by lanthanide ions, transition metal ions, metal clusters, semiconductor nanocrystals, carbon dots, and perovskite nanocrystals; 2) the usage of chiral inorganic materials as chirality sources for CPL, which include chiral nano-silica, inorganic nanocrystals and assemblies. Moreover, many CPL-related properties of these materials are summarized, which include luminophores, chirality sources, excitation/emission bands, quantum yields, and g_{lum}.

In many reports, CPL is based on down-conversion fluorescence with emission bands in the visible light spectrum. Different from this common CPL, the authors continued to introduce some special CPL-active systems featured with up-conversion, NIR emission, thermally activated delayed fluorescence (TADF), and room-temperature phosphorescence. Furthermore, they demonstrate the potential applications of inorganics-based CPL in various areas such as sensors, anti-counterfeiting, optical storage, and asymmetric synthesis.

As for the future study of inorganics-associated CPL-active systems, the authors also put forward their own perspectives on the acquisition of reliable CPL data, improving g_{lum}, evaluation of CPL properties, understanding CPL mechanism, and exploring CPL-related applications.

In summary, Liu *et al.*[7] provided readers with an overview of CPL generated by inorganic materials. These pieces of information are valuable to give insights and guidelines for the design of inorganics-associated CPL-active systems with improved CPL effects and novel applications. We are waiting for more amazing optical events.

DECLARATIONS

Authors' contributions

The author contributed solely to this manuscript.

Availability of data and materials

Not applicable.

Financial support and sponsorship
None.

Conflict of interest
The author declared that there are no conflicts of interest.

Ethical approval and consent to participate
Not applicable.

Consent for publication
Not applicable.

REFERENCES

1. Zhan X, Xu FF, Zhou Z, Yan Y, Yao J, Zhao YS. 3D laser displays based on circularly polarized lasing from cholesteric liquid crystal arrays. *Adv Mater* 2021;33:e2104418. DOI PubMed
2. MacKenzie LE, Pal R. Circularly polarized lanthanide luminescence for advanced security inks. *Nat Rev Chem* 2021;5:109-24. DOI
3. Stachelek P, MacKenzie L, Parker D, Pal R. Circularly polarised luminescence laser scanning confocal microscopy to study live cell chiral molecular interactions. *Nat Commun* 2022;13:553. DOI PubMed PMC
4. Gong Z-L, Zhu X, Zhou Z, et al. Frontiers in circularly polarized luminescence: molecular design, self-assembly, nanomaterials, and applications. *Sci China Chem* 2021;64:2060-104. DOI
5. Deng Y, Wang M, Zhuang Y, Liu S, Huang W, Zhao Q. Circularly polarized luminescence from organic micro-/nano-structures. *Light Sci Appl* 2021;10:76. DOI PubMed PMC
6. Kim H, Im SW, Kim RM, et al. Chirality control of inorganic materials and metals by peptides or amino acids. *Mater. Adv* 2020;1:512-24. DOI
7. Liu X, Jin R. Recent topics on circularly polarized luminescence generated by inorganic materials. *Chem Synth* 2022;2:1.

Su. *Chem Synth* 2022;2:5
DOI: 10.20517/cs.2022.09

Chemical Synthesis

Editorial

Open Access

Happy birthday *Chemical Synthesis*!

Bao-Lian Su[1,2,*]

[1]State Key Laboratory of Advanced technology for Materials Synthesis and Processing, Wuhan University of Technology, Wuhan 430074, Hubei, China.
[2]Laboratory of Inorganic Materials Chemistry, University of Namur, Namur B-5000, Belgium.

***Correspondence to:** Prof. Bao-Lian Su, Laboratory of Inorganic Materials Chemistry, University of Namur, Rue de Bruxelles 61, Namur B-5000, Belgium. E-mail: bao-lian.su@unamur.be

How to cite this article: Su BL. Happy birthday *Chemical Synthesis*! *Chem Synth* 2022;2:5. https://dx.doi.org/10.20517/cs.2022.09

Received: 23 March 2022 **Accepted**: 23 March 2022 **Published:** 25 March 2022

Academic Editor: Bao-Lian Su **Copy Editor:** Jia-Xin Zhang **Production Editor:** Jia-Xin Zhang

Our journal is celebrating its first anniversary as the COVID-19 pandemic is gradually easing. During the last year, we organized a strong international editorial team. With the active participation of outstanding young people in China and abroad, the first youth editorial board team composed of 37 enthusiastic and outstanding young researchers was established. In this year, through the efforts of the editorial department, 14 excellent articles were published in the first two inaugural issues. Among them, one original paper contributed by our honorary Editor-in-Chief Professor Krief was praised by Professor Sharpless, a Nobel Prize winner in Chemistry. Since the first issue was published in November last year, it has received 13,458 views and 2515 downloads and gained widespread attention around the world! We sincerely thank the editorial staff for their hard work, the quality control of our section editors, and the active participation of our young editorial committee members. Special thanks are given to our authors for their high-quality contributions. I have no words to express my gratitude to our reviewers for their precious time devoted to the evaluation of manuscripts and their professionalism and heart for the sciences for the first, second, and sometimes even third rounds of review. We know that we can continue to count on them. The success of this first year is owing to our authors and reviewers.

In the first issue of 2022, the first news is from the "International Organization for Chemical Development (IOCD)" that Prof. Vivian Wing-Wah Yam from Hongkong University, China, was elected as the IOCD's new president, the first woman president. She succeeded Prof. Jean-Marie Lehn, a Nobel Prize winner in Chemistry. We congratulate Prof. Yam for her election and wish her a great success. You will find an

excellent review article on the circularly polarized luminescence in inorganic materials contributed by Prof. Liu from Shanghai Normal University, China, and Prof. Jin from Kanagawa University, Japan. This review article was selected as Editor's choice and highlighted as the cover image. One original research article on a very hot topic "Mn-Ce catalysts for highly efficient C-H activation" was contributed jointly by Prof. Wang and Prof. Xiao from Zhejiang University, China, and Prof. Zhang from Jilin University, China. A research highlight made by Prof. Stephane Siffert, our section editor of catalysis, illustrates the high quality of this contribution. This research article is also highlighted by the cover image. Carbon neutral is our main challenge. Hydrogen economy plays a critical role in energy transformation from fossil fuels to green energy. Prof. Yao and his team from Jilin University, China, and Griffith University, Australia, present a review paper on developing efficient hydrogen storage materials and the corresponding methods to successfully realize the "hydrogen economy".

I sincerely wish that the articles in this issue will bring you the scientific advances you have been waiting for. On this important occasion of the first anniversary of our journal, we look forward to bringing you more chemistry developments, and we wish that you join us to promote together chemical research via our journal and realize our Chemical Synthesis dream.

DECLARATIONS

Authors' contributions

The author contributed solely to this manuscript.

Availability of data and materials

Not applicable.

Financial support and sponsorship

None.

Conflicts of interest

The author declared that there are no conflicts of interest.

Ethical approval and consent to participate

Not applicable.

Consent for publication

Not applicable.

Siffert. *Chem Synth* 2022;2:6
DOI: 10.20517/cs.2022.07

Chemical Synthesis

Research Highlight

Open Access

Check for updates

Mn-Ce catalysts for highly efficient C-H activation

Stephane Siffert*

Unit of Environmental Chemistry and Interactions with Living Organisms (UCEIV), University of Littoral-Opal Coast, Dunkerque F-59140, France.

***Correspondence to:** Prof. Stephane Siffert, Unit of Environmental Chemistry and Interactions with Living Organisms (UCEIV), University of Littoral-Opal Coast, 145 avenue Maurice Schumann, Dunkerque F-59140, France. E-mail: siffert@univ-littoral.fr

How to cite this article: Siffert S. Mn-Ce catalysts for highly efficient C-H activation. *Chem Synth* 2022;2:6. https://dx.doi.org/10.20517/cs.2022.07

Received: 18 Mar 2022 **Accepted:** 21 Mar 2022 **Published:** 29 Mar 2022

Academic Editor: Bao-Lian Su **Copy Editor:** Jia-Xin Zhang **Production Editor:** Jia-Xin Zhang

Keywords: C-H oxidation, Mn-Ce oxides, strong oxide-support interactions (SOSIs)

The environmentally friendly and effective oxidation of sp^3-hybridized C-H bonds has attracted much attention for the sustainable production of alcohols/ketones/epoxides from petroleum hydrocarbons[1,2]. However, the catalysis with oxygen as the oxidant is obstacled by the low efficacy of the catalysts. Mn-Ce solid-solution is reported as a promising catalyst for the aerobic oxidation reactions because of its maximized Mn-O-Ce interfaces, but expensive surfactants and ionic liquids and high Mn content are usually required for maximization of solid-solution phase, which is really costly for the catalyst preparation[3]. However, for oxidation reactions, the solid solution phase is not always the most efficient catalyst[4]. The efficient catalytic oxidation of C-H bonds with molecular oxygen over non-noble metal catalysts, as well as avoiding the solvents and initiator additives, is highly desired yet challenging. Titania (TiO_2) is one of the preferred strong oxide-support interactions (SOSIs) supports[5], but Wang *et al.*[6] reported a highly active Mn-Ce oxide catalyst with SOSIs for the catalytic partial oxidation of hydrocarbons without solvents and initiator additives [Figure 1A]. The TEM analysis showed the existence of manganese oxide layers with two-dimensional and amorphous status on the cerium matrix [MnO_x/CeO_2, Figure 1B and C], and a high capacity of active oxygen species at 46.1% is obtained. The MnO_x/CeO_2 catalyst with SOSIs shows high activities and selectivities in the oxidation of hydrocarbons to alcohols and ketones with molecular oxygen under solvent- and initiator-free conditions at mild temperature [Figure 1A], which outperform the noble metal catalysts and the highly efficient solid-solution Mn-Ce catalysts[3,7]. Importantly, the MnO_x/CeO_2 is stable and exhibits constant performances in the continuous recycling tests.

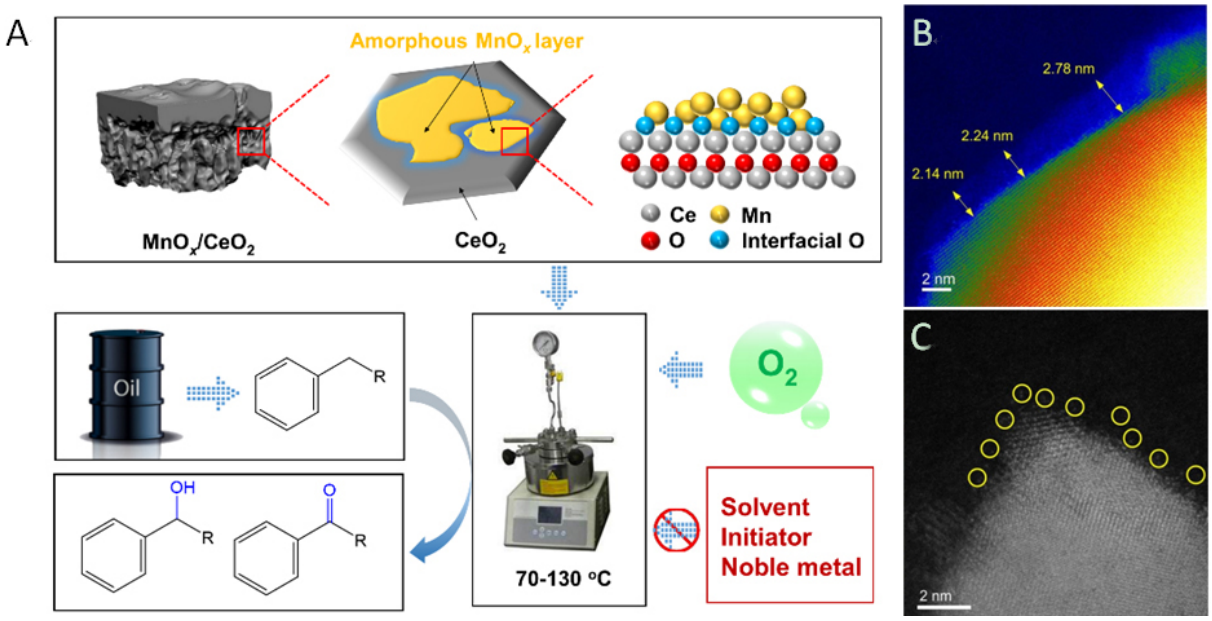

Figure 1. (A) Synthetic and catalytic strategies of the ceria-supported two-dimensional manganese oxide catalyst with SOSIs. (B,C) High-resolution STEM images of MnO_x/CeO_2 catalyst with SOSIs. The isolated Ce sites in the amorphous region were highlighted by yellow circles in (C)[6].

Multiple characterizations (EPR, *in situ* Raman, *in situ* FTIR, *in situ* XPS…) are used to study the redox properties of the materials. The EPR, Raman, and XPS results demonstrated the existence of abundant oxygen vacancies/defective sites in the MnO_x/CeO_2 catalyst, which are beneficial for oxygen activation. More importantly, the *in situ* Raman and XPS studies indicated the availability of the active oxygen species at low temperature (< 80 °C) and can be regenerated during the continuous oxidation process, which makes it extremely active for the aerobic oxidation reactions. The *in situ* FTIR experiments confirmed the pivotal role of surface active oxygen species for the adsorption and activation of the C-H bond, which accelerated the conversion of hydrocarbons to corresponding alcohols and/or ketones.

This work teaches us how to use the SOSIs to construct abundant active interfacial sites for the activation of C-H bonds. The interfacial sites can not only regulate the catalytic activities but also foster further studies on the structure-performance relationship of various supported metal oxide catalysts. It is anticipated that this method will be further applied for designing efficient metal oxide catalysts for the sustainable production of valuable chemicals.

DECLARATIONS

Authors' contributions

The author contributed solely to the article.

Availability of data and materials

Not applicable.

Financial support and sponsorship

None.

Conflicts of interest

The author declared that there is no conflict of interest.

Ethical approval and consent to participate

Not applicable.

Consent for publication

Not applicable.

REFERENCES

1. White MC. Chemistry. Adding aliphatic C-H bond oxidations to synthesis. *Science* 2012;335:807-9. DOI PubMed
2. Marimuthu A, Zhang J, Linic S. Tuning selectivity in propylene epoxidation by plasmon mediated photo-switching of Cu oxidation state. *Science* 2013;339:1590-3. DOI PubMed
3. Zhang P, Lu H, Zhou Y, et al. Mesoporous MnCeOx solid solutions for low temperature and selective oxidation of hydrocarbons. *Nat Commun* 2015;6:8446. DOI PubMed PMC
4. Jonas F, Lebeau B, Siffert S, et al. Nanoporous CeO_2-ZrO_2 Oxides for Oxidation of Volatile Organic Compounds. *ACS Appl Nano Mater* 2021;4:1786-97. DOI
5. Barakat T, Rooke JC, Cousin R, et al. Investigation of the elimination of VOC mixtures over a Pd-loaded V-doped TiO_2 support. *New J Chem* 2014;38:2066-74. DOI
6. Wang H, Wang L, Luo Q, et al. Two-dimentional manganese oxide on ceria for the catalytic partial oxidation of hydrocarbons. *CS* 2022. DOI
7. Wang L, Zhu Y, Wang JQ, et al. Two-dimensional gold nanostructures with high activity for selective oxidation of carbon-hydrogen bonds. *Nat Commun* 2015;6:6957. DOI PubMed PMC

Liu *et al. Chem Synth* 2022;2:7
DOI: 10.20517/cs.2022.01

Chemical Synthesis

Review

Open Access

Check for updates

Recent advances in circularly polarized luminescence generated by inorganic materials

Xinling Liu[1], Ren-Hua Jin[2,*]

[1]The Education Ministry Key Lab of Resource Chemistry, College of Chemistry and Materials Science, Shanghai Normal University, Shanghai 200234, China.
[2]Department of Material and Life Chemistry, Kanagawa University, Yokohama 221-8686, Japan.

Correspondence to: Prof. Ren-Hua Jin, Department of Material and Life Chemistry, Kanagawa University, 3-27-1 Rokkakubashi, Kanagawa-ku, Yokohama-shi, Yokohama 221-8686, Japan. E-mail: rhjin@kanagawa-u.ac.jp

How to cite this article: Liu X, Jin RH. Recent advances in circularly polarized luminescence generated by inorganic materials. *Chem Synth* 2022;2:7. https://dx.doi.org/10.20517/cs.2022.01

Received: 5 Jan 2022 **First Decision:** 7 Feb 2022 **Revised:** 23 Feb 2022 **Accepted:** 24 Feb 2022 **Published:** 24 Feb 2022

Academic Editor: Bao-Lian Su **Copy Editor:** Jia-Xin Zhang **Production Editor:** Jia-Xin Zhang

Abstract

Circularly polarized luminescence (CPL) is an interesting phenomenon that represents the unequal emission of left- and right-handed polarized light from an emitter. CPL is promising in chirality characterization and various optical applications. Traditionally, research on CPL has been centered on organic substances. Nevertheless, in recent years, CPL based on inorganic substrates has also become a nascent topic, which is significant in exploring novel chirality- and luminescence-related properties and applications in inorganic materials. This short review summarizes the recent progress made regarding the following two aspects: 1) how to endow common inorganic luminophores with CPL activity; 2) how to use emerging chiral inorganic nanomaterials to design CPL-active systems. The general synthesis strategies, optical properties, applications and outlook of CPL-active inorganic materials are also demonstrated.

Keywords: Circularly polarized luminescence, chirality, luminescence, inorganic luminescent materials, inorganic chiral materials

INTRODUCTION

Chirality is termed as the phenomenon where a certain object is nonsuperposable on its mirror image. When two objects with such a relationship exist, they are known as enantiomers. Chirality is pervasive and manifests itself at different scales, ranging from macroscopic left and right hands to molecular-scale

asymmetric carbon atoms and to various helical structures [Figure 1A-C]. The significance of chirality is well acknowledged, for example, only one given enantiomeric form of many biomolecules is preferred to maintain life. The above homochirality of life also raises an exacting enantiomer selectivity toward numerous daily chemicals, drugs and pesticides. Therefore, understanding chiral structure-property relationships is one of the most important topics across a broad range of disciplines[1,2].

Light can also be chiral in the form of circularly polarized (CP) light. As shown in Figure 1D, around the direction of propagation, the electric field of CP light rotates in either a counterclockwise or clockwise helical pattern, resulting in left-handed CP light (LCP) or its counter-enantiomer of right-handed CP light (RCP), respectively. CP light has many promising applications, including three-dimensional (3D) and holographic display, spintronics, encryption, diagnosis and asymmetric synthesis[3-10]. Traditionally, a combination of a linear polarizer and a quarter-wave plate is applied to obtain CP light. However, this method suffers from a severe loss of light, especially in LED displays (up to 50%), invalidity beyond a certain frequency range and incompatibility with highly integrated photonic circuits[11,12]. Therefore, it is of interest to explore high-efficiency methods for the generation of CP light.

Usually, enantiomers are indistinguishable to some extent, since they share many identical properties. Fortunately, they respond differently toward LCP and RCP, which enables us to "see" microscale chiral matter using CP light-based spectroscopy[13,14]. Furthermore, the capability of chiral substances to manipulate the polarization states of light provides an alternative method to enable a luminophore to emit LCP and RCP beams unequally, which is known as circularly polarized luminescence (CPL)[15]. A schematic description for CPL in chiral systems is shown in Figure 1E. In principle, a pair of CPL-active enantiomers exhibit the same photoluminescence (PL) spectra. However, the LCP and RCP components in the emission are unequal when chirality is taken into consideration, *i.e.*, LCP is over than RCP in one enantiomer, while the reverse is true in the other enantiomer. By measuring the difference between LCP and RCP (denoted by "I_L-I_R", where I_L and I_R are the intensity of LCP and RCP, respectively) at a given emission wavelength, a CPL spectrum can be drawn using "I_L-I_R" as the vertical axis and emission wavelength as the horizontal axis. It is noted that the value of "I_L-I_R" is expressed as an ellipse angle θ (mdeg) in many studies and some commercial CPL instruments. This is because the overall polarization trajectory for a mixture of LCP and RCP light becomes an ellipse when I_L is unequal to I_R. The CPL signals usually overlap with the corresponding PL signals, but a pair of enantiomers show opposing CPL spectra.

Another important index to evaluate CPL is the dissymmetry factor of g_{lum}:g_{lum} = $[2(I_L-I_R)]/(I_L+I_R)$. For the values of g_{lum} ranging from -2 to +2, only a given handedness CP light is emitted in the extreme cases (+2 for LCP only and -2 for RCP only), while no circular polarization occurs (i.e., I_L=I_R) when g_{lum} is zero. Consequently, CPL spectroscopy affords a unique tool to study the chiral structures and properties of matter in excited states, is the emission analog of common circular dichroism (CD) spectroscopy and is supplementary to fluorescence spectroscopy. In return, the construction of various CPL-active chiral luminescent materials further expands the applications of CP light.

Over the past decade, notable progress has been made in the exploration of novel CPL-active systems, together with the advancement of CPL spectroscopy. However, much research has focused on organic substances, partially due to the fact that research on chirality has a long history in organic chemistry[16-21]. According to the principles of CPL in chiral systems, the choices of either luminescent or chiral unity should be diverse, thus allowing for a broad range of potential CPL-active systems beyond organics. On this basis, it is noteworthy that inorganic-based CPL has become a new and active research topic in recent years. For example, many inorganic luminophores are employed to create more colorful CPL candidates and

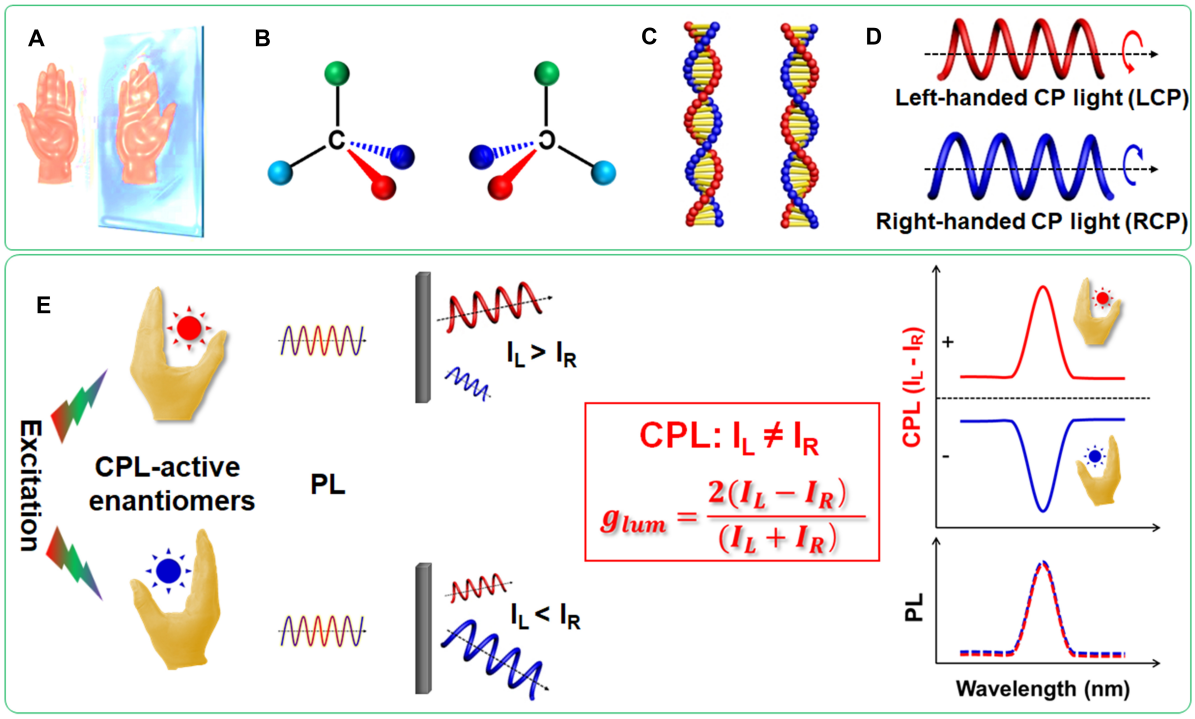

Figure 1. Typical enantiomers of (A) left and right hands, (B) chiral carbon centers, (C) helices and (D) left- and right-handed CP light. (E) Schematic of CPL from two CPL-active enantiomers. CPL: Circularly polarized luminescence.

emerging chiral inorganic nanomaterials are able to impart various luminophores with CPL activity[22,23]. Such research is significant for many reasons, including the fact that it brings a new perspective to explore the luminescence properties and mechanisms of inorganic luminophores, especially in chiral environments. In addition, it provides a toolbox to analyze the structures of chiral inorganic materials and is helpful in understanding the chirality transfer in "matter-matter" or "light-matter" interactions. Finally, it also offers more inorganic/organic functional materials with the power to manipulate light to broaden CPL-based applications[24-28].

In this short review, we consider two inorganic-associated CPL-active systems, namely, inorganic luminophore-containing and chiral inorganic host-based systems. For the former systems, various classes of inorganic luminophores are described, including metal ions (e.g., lanthanide and chromium ions), perovskite nanocrystals (NCs), metal clusters, carbon dots and semiconductors nanoparticles (NPs). Given that there are some recent well-written reviews focusing on lanthanide complexes, chromium complexes and perovskite NCs, they are discussed at length here. With regards to the latter systems, the utilization of chiral silica (SiO_2) nanomaterials, chiral inorganic crystals and helical inorganic assemblies as hosts for CPL is discussed. To demonstrate the recent progress in these systems, some typical examples are selected and discussed. The properties (components, construction strategies and excitation and emission wavelengths, g_{lum}) of these examples are summarized in Table 1.

We provide an overview of inorganic-based CPL. Firstly, several types of construction strategies for CPL-active systems are summarized, which are further clarified by selected examples of CPL-active systems containing inorganic luminophores or chiral inorganic nanomaterials. Next, CPL-active systems based on some special luminescent processes are listed, which are different from the common down-conversion

Table 1. Components, construction strategies and CPL properties of some inorganic-based CPL-active systems

Luminophore	Construction strategy type [chiral sources]	Excitation wavelength (nm)	Emission wavelength (nm)	Quantum yield (%)	Magnitude of g_{lum}
1. Inorganic luminophore-based CPL					
Yb^{3+}	II [PrPyBox, PhPyBOx]	365	972	0.60-0.70	10^{-2}, Ref.[78]
$NaYF_4$:Yb/Tm, $NaYF_4$:Yb/Er	III [L-/D-GAm assemblies]	980	360, 476, 802 (Tm), 540, 654 (Er)	N	10^{-3}, Ref.[88]
$CaAl_2O_4$:Eu, Nd	II [L-/D-cysteine]	320	440	N	10^{-2}, Ref.[81]
ZnO	I [L/D-methionine]	325	510	N	N , Ref.[36]
CdSe	II [L-/D-cysteine]	451	605	N	10^{-3}, Ref.[41]
CdSe/CdS	II [L-/D-cysteine]	400	583-683	35-60	10^{-4}, Ref.[64]
Ag clusters	I [see Figure 6A]	365	558	3.9	10^{-1}, Ref.[57]
Au clusters	I [see Figure 12A]	365	500	36.7	10^{-3}, Ref.[86]
Ag clusters	I [see Figure 12A]	N	574	56, 95	10^{-3}, Ref.[80]
AuAg clusters	III [G-quartet nanofiber]	356	475	9.42	10^{-2}, Ref.[82]
Ag clusters	III [zeolite assembly]	360	520	N	10^{-2}, Ref.[60]
Carbon dots	III [L-/D-GAm assemblies]	350-370	445-455	N	10^{-3}, ref.[54]
Carbon dots	III [L-/D-GAm assemblies]	380	546, 604	30-55	10^{-3}, Ref.[55]
Carbon dots	III [cellulose nanocrystal assembly]	N	450-620	5.2 (FL), 0.16 (Phos)	10^{-1}, Ref.[52]
2. Chiral inorganic host-based CPL					
Tb^{3+}	III [helical silica]	230	545	N	10^{-3}, Ref.[70]
$CsPbBr_3$	III [helical silica]	365	517.5	N	10^{-3}, Ref.[73]
Tetraphenylethylene (TPE) derivative	III [helical silica]	366	453	57	10^{-2}, Ref.[75]
TPE derivative	III [helical silica]	365	500	20-27	10^{-3}-10^{-4}, Ref.[74]
Tb_2O_3, Eu_2O_3	III [chiral silica nanofibers]	375	545 (Tb_2O_3), 615 (Eu_2O_3)	N	10^{-3}, Ref.[71]
Porphyrin (TCPP), TPE, $MAPbBr_3$	III [chiral silica nanofibers]	375	650 (TCPP), 476 (TPE), 525 ($MAPbBr_3$)	N	10^{-3}, Ref.[72]
Eu^{3+}	III [$TbPO_4{\cdot}H_2O$]	365	590-705	N	10^{-3}-10^{-2}, Ref.[26]
DACT and TMD	III [assemblies of GdOOH nanowires]	N	550 (DACT), 650 (TMD)	N	N, Ref.[76]

N: Not given; FL: fluorescence; Phos: phosphorescence.

luminescence in the visible range. Some typical applications are displayed, followed by a short conclusions and perspectives section.

CONSTRUCTION STRATEGIES FOR CPL-ACTIVE SYSTEMS

There are various strategies to achieve CPL in chiral systems. A straightforward strategy [type I, Figure 2A] is where the luminophore itself is chiral, which is known as an intrinsically chiral luminophore. However, unlike organic molecules with diverse chiral geometries, many inorganic luminescent substances are not chiral. Therefore, a subtle design of symmetry-breaking synthetic methods is often required to produce chiral structures[26,29]. Chirality transfer is widespread on various interfaces[30,31], which makes it more flexible and versatile to enable CPL, even on preformed achiral luminophores. More specifically, the chirality can be transferred from chiral ligands [type II, Figure 2B] and chiral hosts [type III, Figure 2C]. In Type I, to acquire chiral products, chiral ligands or hosts are also employed but are finally removed. Compared with type I, one characteristic in types II and III is that the chiral ligands or hosts are required to co-exist with the luminophore for chirality inducement.

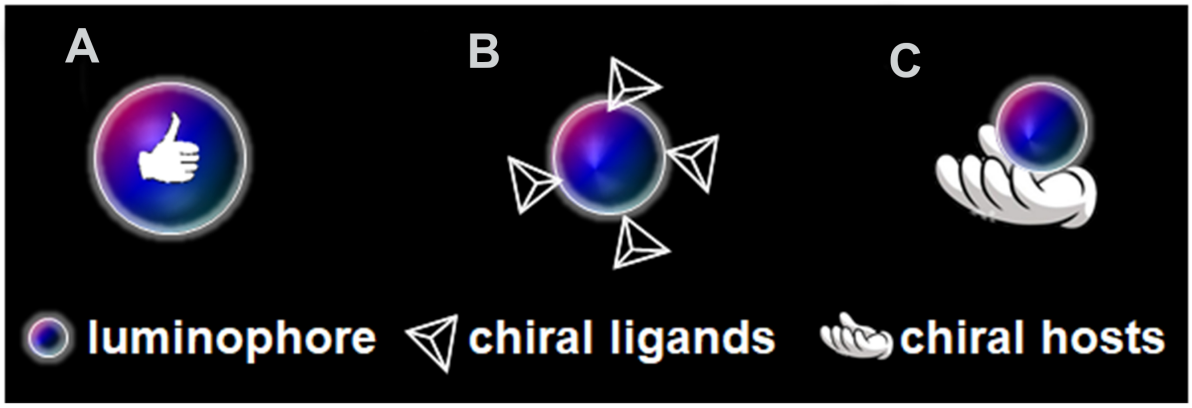

Figure 2. Three types of construction strategies of CPL-active systems: (A) intrinsically chiral luminophores (type I); (B) chiral ligand-induced CPL (type II); (C) "host-guest"-induced CPL (type III). CPL: Circularly polarized luminescence.

Intrinsically chiral luminophores (type I)

The chirality in inorganic materials can appear in various forms. For crystalline materials, point and space groups are basic tools to describe crystal structures. There are 230 group spaces, which are created via the combination of 32 point groups and 14 types of Bravais lattices. Point and space groups are also useful to judge chirality and chiroptical activity. Chiral crystals can exist in 65 Sohncke space groups, which are divided into two categories: I) 22 chiral groups with helical operations that thus contain 11 enantiomeric pairs (e.g., $P3_1$ and $P3_2$); II) the remaining 43 groups are achiral; however, if the unit (i.e., the smallest collection of atoms from which the whole crystal is restored by the application of all symmetry operations of the space group and translation) is chiral, the crystals can be chiral[32]. Early in 1948, chiral crystals with CPL activity were demonstrated in sodium uranyl acetate $Na[UO_2(CH_3COO)_3]$ crystals formed from achiral molecular subunits. The space group of $Na[UO_2(CH_3COO)_3]$ crystals belongs to the chiral space group of $P2_13$ and the chirality is caused by the helical canting of the three $[UO_2(CH_3COO)_3]$ rings and the noncentrosymmetric spatial arrangement of four coordination clusters. Moreover, the crystallographic structure is cubic, which is advantageous to observe CPL with small interruptions caused by birefringence. With such unique structures, a high g_{lum} of 1.31 was observed in $Na[UO_2(CH_3COO)_3]$ crystals by Riehl and Richardson[33] and Moran *et al.*[34].

Another method to endow crystals with optical activity is by creating crystalline defects (e.g., screws and distortions), which are caused by chiral additives regulating the nucleation-growth process[35]. In addition to the lattice chirality described above, chiral nano-/micromorphologies (e.g., copying the helical patterns of chiral organic templates) on a higher length scale can also induce chiroptical activity in crystalline or amorphous materials[31]. Duan *et al.*[36] demonstrated chiroptically-active crystalline ZnO films with multiple chiralities on different scales. Using chiral amino acids of L-/D-methionine (Met) as both structure-directing and symmetry-breaking agents, chiral hydroxide zinc carbonate (HZC) nanostructures were formed on quartz substrates. After removing organic species by calcination at 550 °C in air, HZC was transformed into chiral nanostructured ZnO films (L-CNZF, obtained with L-Met) with three levels of chirality [Figure 3]. On the primary level, the crystal structure of the ZnO nanoplate shows a subtle helical distortion along the [10-11] axis in a left-handed coiled pattern together with some lattice defects, which is caused by the chiral center of the methionine molecules. On the secondary level, several dozens of ZnO nanoplates are bent into a ZnO particle with a right-handed helix form. On the tertiary level, the arrangement of several ZnO particles forms a left-handed circinate helical morphology on the microscale. For the ZnO films (D-CNZF) obtained using D-Met, the handedness one of each level is just opposite to the corresponding one of L-CNZF. These ZnO films showed various chiroptical activities in their CD, CPL and

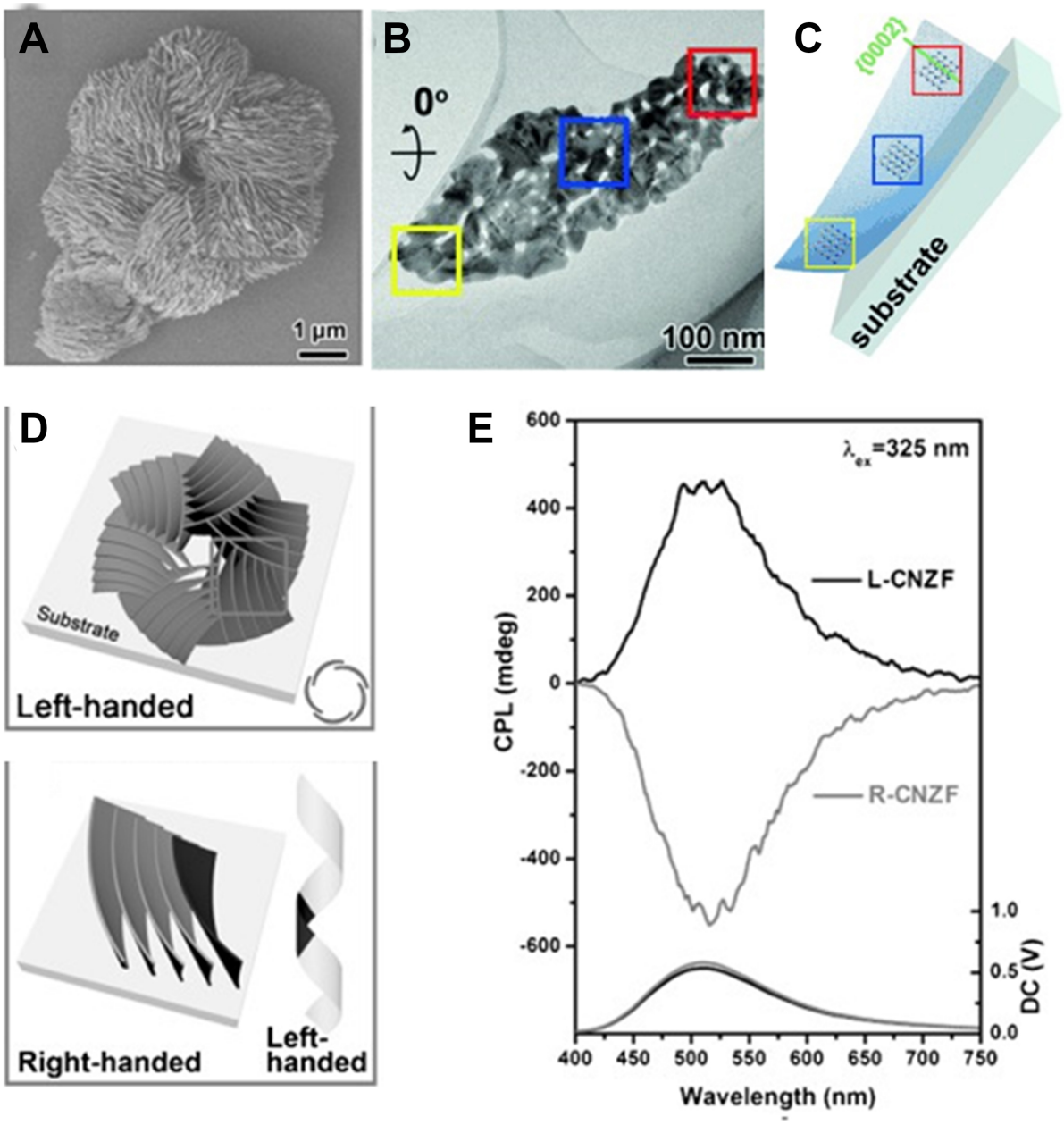

Figure 3. (A) SEM image of L-CNZF. (B) TEM image and (C) SAED patterns of a single ZnO nanoplate. (D) Schematic of hierarchical chirality in L-CNZF. (E) PL and CPL spectra of L- and R-CNZF. Reproduced with permission from Ref.[36]. Copyright (2015) John Wiley and Sons. SAED: Selected area electron diffraction; CPL: circularly polarized luminescence; PL: photoluminescence; CNZF: chiral nanostructured ZnO films.

Raman optical activity spectra. Under a 325 nm excitation, D-CNZF and L-CNZF exhibited antipodal CPL signals centered at 510 nm, consistent with the fluorescence band maximum.

Chiral ligand-induced CPL (type II)

Small chiral organic molecules are widely found and are powerful for producing chiroptical signals on inorganic substances. As shown in Figure 4, for example, CD signals are observed on plasmonic metal (Au and Ag) and semiconductor (e.g., CdS, CdSe and CdTe) NPs capped with chiral ligands[40-42]. The chirality

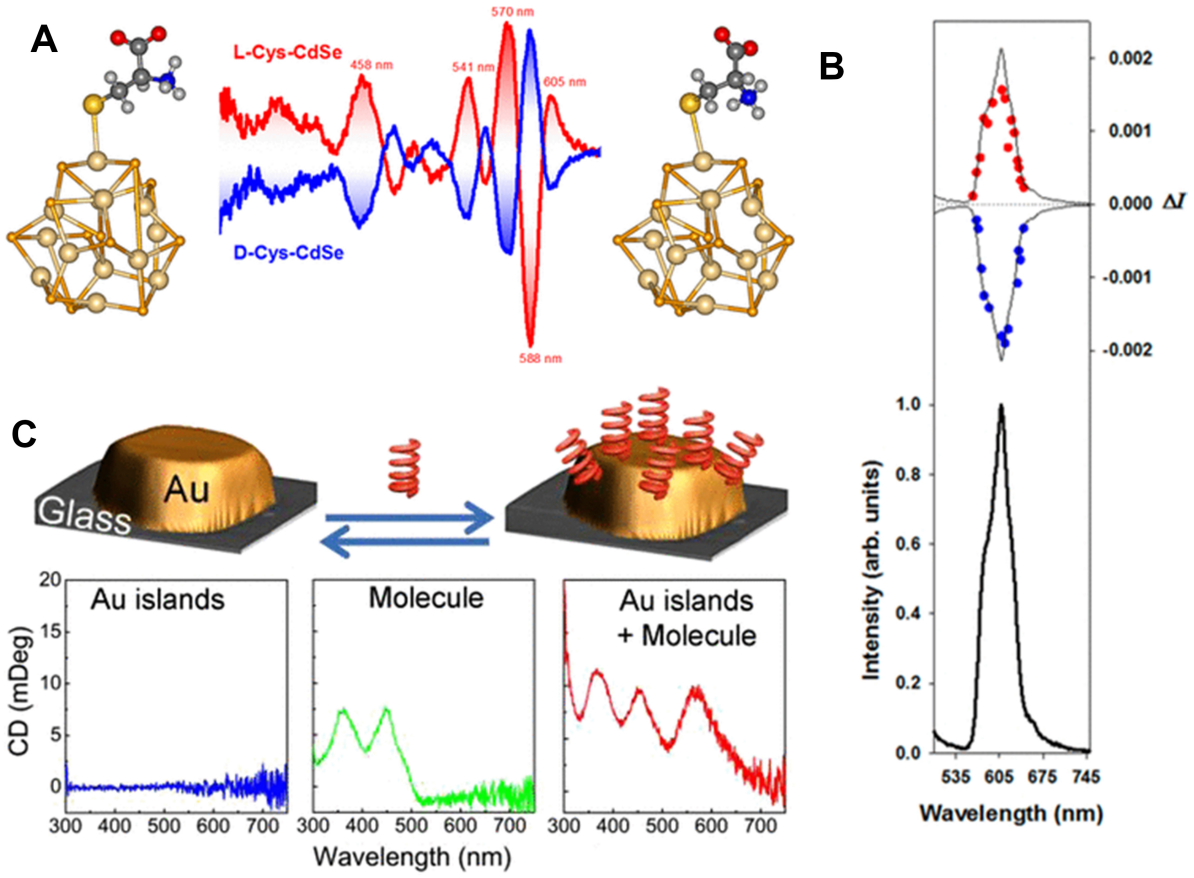

Figure 4. (A) Optimized geometries and induced CD spectra. (B) CPL (top) and total luminescence (bottom) spectra of L- and D-cysteine-capped CdSe quantum dots. Reproduced with permission from Ref.[41]. Copyright (2013) American Chemical Society. (C) Chiral riboflavin molecule-induced CD optical activity in Au islands deposited on a glass substrate. Reproduced with permission from Ref.[42]. Copyright (2013) American Chemical Society. CD: Circular dichroism; CPL: circularly polarized luminescence.

transfer from ligands to inorganics can proceed through various mechanisms, including surface atom distortion with asymmetric clusters, the chiral arrangement of ligands on the surface, crystalline defects and the electronic interaction or coupling between chiral molecules and inorganic species[43,44].

The combination between inorganic nanomaterials and chiral ligands can be fulfilled by two synthetic routes, namely, ligand-guided one-step synthesis or post-modification by ligands exchanges. Although these methods appear easy to carry out, the chirality induction is dependent upon many factors, such as the types of ligands, the sizes/shapes of the NPs and the synthetic conditions. Furthermore, although the chirality is mainly judged by the CD signals, CD activity does not guarantee CPL activity. This is understandable based on the differences between the CD and CPL mechanisms, i.e., CD is associated with absorption from the ground states, while CPL is associated with emissions in the excited states.

"Host-guest"-induced CPL (type III)

Based on the concept of chirality induction in type II, it is found that various luminescent guests show chiroptical activity after being embedded in many chiral materials as chiral hosts. Moreover, several different guests can be simultaneously integrated into one host to acquire white CPL. In particular, with this method, emerging novel inorganic nanomaterials have found broad applications in CPL in recent years by

encapsulating inorganic and/or organic luminescent guests. As a result, this strategy is more flexible for producing multicolor CPL by a rational combination between hosts and guests, thus widening the scope of inorganic CPL-active systems.

OVERVIEW OF INORGANIC-ASSOCIATED CPL-ACTIVE SYSTEMS

Inorganic luminophore-containing systems

Metal ion-based luminophores

Lanthanide ions [Ln(III)] are appealing for CPL because of their interesting optical properties, such as a large pseudo-Stokes shift, long lifetime and unique spectral fingerprint from the ultraviolet (UV) to near-infrared (NIR) range. In particular, the magnetic dipole allowed transitions in lanthanide ions are advantageous for a high g_{lum}; for example, a high g_{lum} value of 1.38 was reported for Eu(III) complexes[45]. Since lanthanide ions are isotropic, lanthanide-based CPL is predominantly demonstrated in various chiral lanthanide complexes, where the coordination orientation of chiral ligands can form left- or right-handed twists and helices. The CPL mechanism of these complexes can be interpreted based on multipole [Ln(III)]-point charge (chiral ligand) interactions and/or multipole [Ln(III)]-dipole (excited-ligand) coupling. Since there have been several recent reviews on CPL-active lanthanide complexes, they are not described here and the reader can refer to Refs.[46-48].

Other transition metal complexes with CPL activity have also been reported. For example, chromium(III) (Cr^{3+}) is of interest due to its earth abundance, kinetic inertness and magnetically allowed but electric-dipole forbidden emissions (600–800 nm) from the Cr(^{2}E) and Cr($^2T_1$) states. In a recent report, helical $[Cr(dqpR)_2]^{3+}$ (dqp = 2,6-di(quinolin-8-yl)pyridine; R = OCH_3, Br or C ≡ CH) complex enantiomers were resolved[49]. A high quantum yield (up to 17%), long-lived excited lifetimes (1.35 ms) at room temperature in aqueous solutions and a large g_{lum} (0.20) were found for these chiral complexes, thereby providing satisfactory CPL brightness. More reports on CPL-active chromium-based materials have been well summarized in a recent review[50], so this topic will not be discussed in detail here.

In addition to metal complexes, metal ion-containing luminophores can also be found in metal oxides (e.g., Eu_2O_3) and metal ion-doped inorganic matrixes (e.g., $NaYF_4$:Yb/Tm, $NaYF_4$:Yb/Er and $CaAl_2O_4$:Eu,Nd). As discussed below, they can also be engineered with CPL in highly thermal stable oxides for up-conversion, NIR emission and phosphorescence applications.

Carbon dots

Since the discovery of carbon dots in 2006, their luminescence has gained increasing attention as they possess many important features, such as easy production, rich raw materials, multicolor emission, high stability and versatile surface chemistry. In some early reports, carbon dots with chiroptical activity in their CD spectra were easily prepared using chiral molecular precursors; however, the CPL activity was not easily demonstrated[51]. The CPL of carbon dots was recently activated using the simple "host-guest" strategy[52-55].

One special characteristic of carbon dots is that their emission wavelength can be tuned by changing their excitation wavelength. Building on this phenomenon, Li *et al.*[54] showed an excitation-dependent CPL example. A chiral L-/D-glutamic acid gelator (L-/D-GAm) was assembled into a helical structure that was used as a chiral host to co-assemble with the nitrogen-doped carbon dot guest. The as-formed composites (L-and D-co-gels) appeared as spiral nanotubes [Figure 5A]. The maximum emission wavelength changed from 400 to 460 nm as the excitation wavelength increased from 300 to 400 nm [Figure 5B]. Similarly, the CPL signals were also red-shifted with increasing excitation wavelength from 350 to 370 nm [Figure 5C] and the $|g_{lum}|$ was ~ 2×10^{-3}-4×10^{-3} under a 360 nm irradiation.

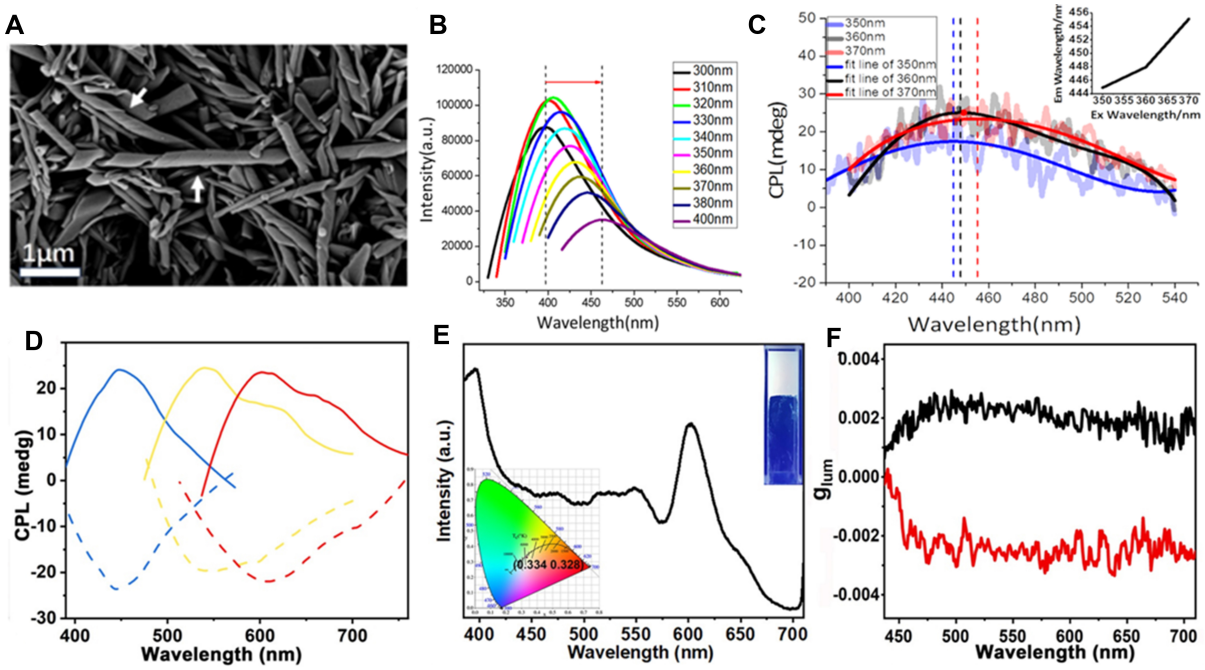

Figure 5. Morphologies and optical properties of D-co-gel: (A) FE-SEM image; (B) PL; (C) CPL spectra with the fitting line (inset: plot of the maximum CPL emission wavelength versus the excitation wavelength) under different excitations. Reproduced with permission from Ref.[54]. Copyright (2020) American Chemical Society. (D) Mirror image CPL spectra of three carbon dot-doped co-gels. (E) PL spectra of white-emitting co-gel (insets: a photograph of the co-gel under 365 nm (top right) and its CIE coordinate value (bottom left). (F) g_{lum} of white-emitting co-gel from D-GAm (black) and L-GAm. Reproduced with permission from ref.[55]. Copyright (2021) John Wiley and Sons. PL: Photoluminescence; CPL: circularly polarized luminescence.

Again, using L-/D-GAm co-gels as the hosts to encapsulate three kinds of carbon dots with blue, yellow and red emission colors, Ru *et al.*[55] demonstrated a white CPL system. These carbon dots displayed CPL signals at 450, 550 and 610 nm, with a $|g_{lum}|$ of ~10^{-2} [Figure 5D]. Furthermore, by simply blending these three kinds of carbon dots at a mass ratio of 4.63:15.75:1 (blue:yellow:red), white emission was fulfilled with a CIE chromaticity diagram coordinate value of (0.334, 0.329) [Figure 5E]. This as-obtained mixture showed circularly polarized white-light emission with a g_{lum} of ~ 2.5×10^{-3} [Figure 5F], which is smaller than the g_{lum} of the individual carbon dots.

Metal clusters

Fluorescent metal clusters composed of a few to a hundred atoms represent a class of special luminophores that provide a link between nanoparticles and the atomic behavior of metals. These ultrasmall metal clusters exhibit molecule-like properties, including size-regulated fluorescence and discrete electronic states, which are promising for a broad range of biological applications. The ultrasmall size of the metal clusters is also possibly advantageous for the combination between metal clusters and ligands (or hosts), meaning that diverse CPL-active metal clusters can be synthesized by the three strategies discussed above (types I-III)[56].

Wu*et al.*[57] synthesized spirocyclic Ag clusters [2-(R) and 2-(S), Figure 6A] using two types of chiral diide ligands and 2-(pyridin-2-yl)-1H-benzo[d]imidazole (PBZ). The intrinsic chirality origin of 2-(R) and 2-(S) can be ascribed to the chiral diides, the spirocyclic arrangement of a Ag_9 cluster and the helical arrangement of PBZ molecules. In addition, 2-(R) and 2-(S) can crystalize into crystals with the chiral space group of $P2_1$. In a mixed solvent of water and methanol, with an increase in the water fraction, 2-(R) and 2-(S) assemble into μm-long helical nanofibers. Furthermore, the solid films of 2-(R) and 2-(S) show strong and mirror-

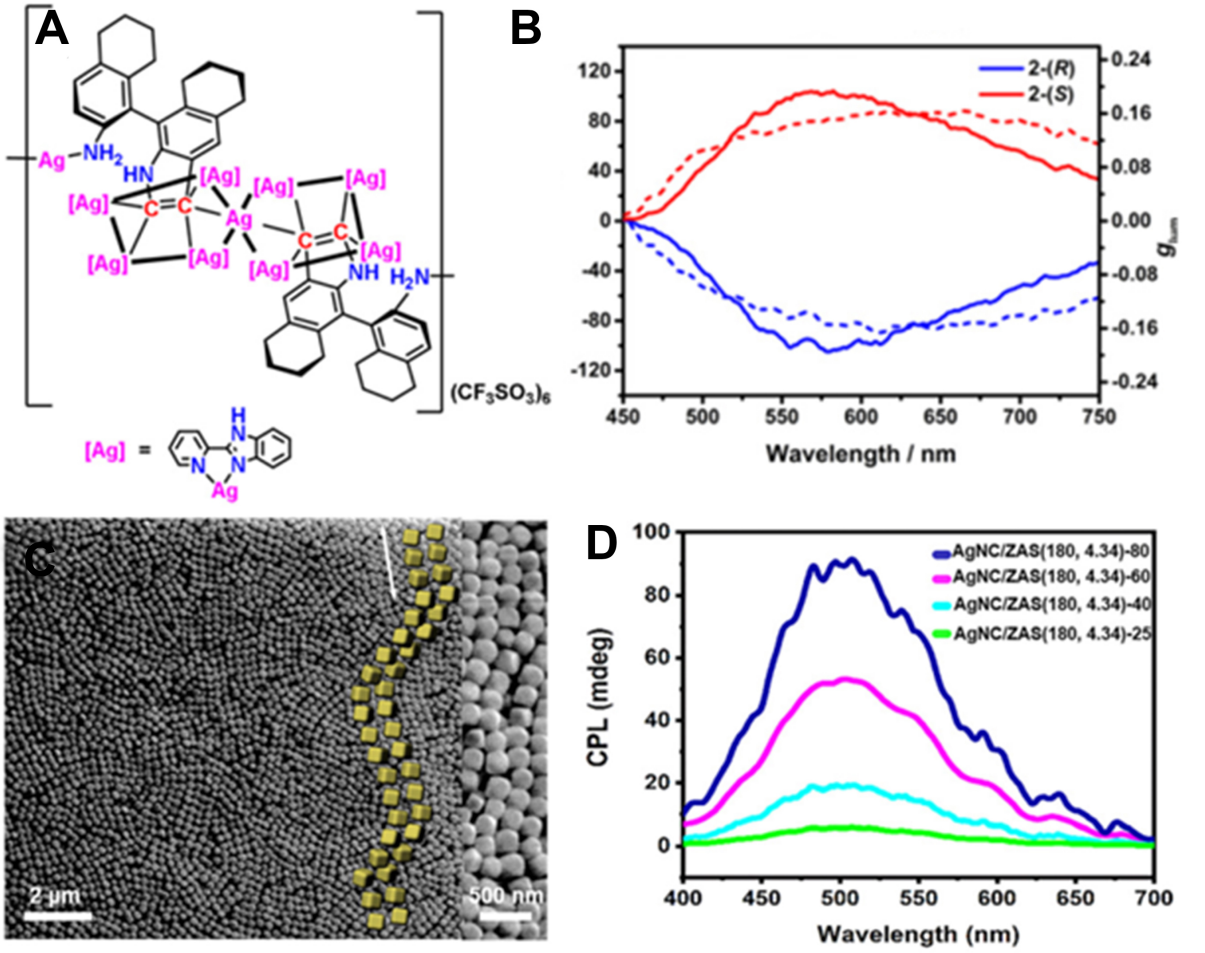

Figure 6. (A) Spirocyclic Ag cluster structure of 2-(S). (B) CPL spectra (solid line) and g_{lum} (dotted line) for film samples of 2-(R) and 2-(S). Reproduced with permission from ref.[57]. Copyright (2021) John Wiley and Sons. (C) SEM image of ZAS(180, 4.34)-80 showing helices with yellow blocks. (D) CPL spectra of AgNC/ZAS(180, 4.34)-T under different temperatures (T). Reproduced with permission from Ref.[60]. Copyright (2020) John Wiley and Sons. CPL: Circularly polarized luminescence; ZAS: zeolite LTA superball.

imaged CPL signals centered at 558 nm, with a high g_{lum} of 0.16 [Figure 6B]. Such a high g_{lum} may benefit from the exciton couplings between the helically arranged PBZ molecules of individual spirocyclic clusters and the microscopic helical assembly. In other words, both the molecular-level and microscale chirality contribute to the high g_{lum}. The assembly- and aggregate-induced CPL of metal clusters is also found in gold clusters of Au_3[R/S-BINAP]$_3$Cl and copper clusters of $[Cu_{14}(R/S\text{-DPM})_8]^{6+}$ (DPM = R/S-2-diphenyl-2-hydroxylmethylpyrrolidine-1-propyne), which are CPL inactive when dispersed in good solvents (e.g., CH_2Cl_2) but become CPL active in the aggregate states after the addition of poor solvents (e.g., n-hexane)[58,59].

Using a host-guest method, Tao *et al.*[60] reported the CPL activity of luminescent Ag nanoclusters (AgNC) incorporated in colloidal zeolite LTA superball (ZAS) assemblies. The macroscopic porous films built from ZAS showed 3D long-range periodicity featuring a photonic band gap (PBG) [Figure 6C]. For one-dimensional PBG structures, the maximum PBG wavelength λ_{max} is calculated as follows: $\lambda_{max} = nP\sin\theta$, where n and P are the average refractive index and helical pitch of a PBG structure, respectively, θ is the angle of the incident light with respect to the PBG structures. A PBG structure with a helical periodic profile can selectively reflect CP light, especially at λ_{max}, with the same handedness of the PBG structure while

allowing the transmittance of the opposite-handed CP light[61-63]. For example, LCP is blocked while RCP is transmitted within a left-handed helical PBG structure, and therefore a large difference between LCP and RCP was detected with a high g_{lum}. By embedding luminescent AgNC, the AgNC/ZAS enabled the selective reflection of R-CP light and allowed L-CP light, resulting in a g_{lum} of 0.013 at a 520 nm emission. The g_{lum} can be tuned by the assembly temperature to change the helical pitches of PBG structures [Figure 6D].

Semiconductor nanocrystals

Semiconductor nanocrystals (NCs), mainly comprised of elements from the II-VI, III-V and IV-VI groups of the periodic table, show many promising optical properties, including exceptional brightness, high quantum yield, superior photostability and size-tunable emission. Colloidal semiconductor NCs are usually capped with organic ligands for the purposes of surface passivation and good dispersibility. In addition, surface ligands also influence the photoluminescent properties. By a ligand-exchange step, chiral ligands can be absorbed onto the surfaces of NCs to make semiconductor NCs CPL active[27,41,64].

As shown in the previous work by Tohgha *et al.*[41], CPL signals at ~ 605 nm ($|g_{lum}|$ of 3-4×10^{-3}) are observed on CdSe NPs modified with D- and L-cysteine. Furthermore, Cheng *et al.*[64] conducted a systematic study of the CPL properties of cysteine-modified CdSe/CdS core-shell NCs with different shapes [Figure 7A][27]. The CdS shell could improve the luminescent quantum yield (QY) of the CdSe core. Interestingly, even if the CdSe core is separated from chiral ligands by the CdS shell, CdSe still shows CPL bands from 550 to 650 nm with a $|g_{lum}|$ of 1-9×10^{-4}. The CPL performance may be caused by orbital coupling and Coulombic dipole interactions between CdSe and cysteine. The PL and CPL could be manipulated by the thickness and shapes of the CdS shell (g_{lum} increases with decreasing CdS shell thickness) but is proportional to the QY [Figure 7B and C]. This work confirmed that chiral ligands can control the whole wavefunction even though there exists an energy barrier of the thin CdS shell.

Perovskite nanocrystals

Luminescent metal halide perovskite colloidal NCs composed of inorganic octahedral layers and organic ligands represent a class of promising next-generation optoelectronic materials. As summarized in recent reviews[65-67], using type I and II strategies with the assistance of a series of chiral ligands, CPL is also extended to perovskite NCs with potential applications in CP light detection, quantum networks, ferroelectrics and spintronics. In addition to organic molecules as chirality sources, some inorganic nanomaterials are also able to endow perovskite NCs with CPL activity, thereby offering new CPL-active candidates.

Chiral inorganic host-based systems

Chiral silica

Over the past two decades, a variety of chiral silica nanomaterials have been reported and their chirality can be manifested by helical outwards or molecular-scale asymmetry on the siloxane framework[68]. Compared with chiral organic molecules, a prominent feature of silica is its thermal stability (close to 1,000 °C), which is desirable for high-temperature synthetic procedures. It has been confirmed that ions, molecules and nanoparticles incorporated within these chiral nano-silica materials can become CD active[69,70]. With the above success, it is of interest to explore chiral silica-based CPL-active systems.

Our group first demonstrated several entirely inorganic silica-lanthanide oxide CPL systems[71]. In our previous work, we found that linear polyethylenimine and L- (or D-) tartaric acids can co-assemble into catalytic chiral templates to direct the formation of chiral SiO_2 nanofibers [Figure 8A]. Vibrational circular dichroism spectroscopic analysis revealed the asymmetric feature of Si-O-Si frameworks on the molecular

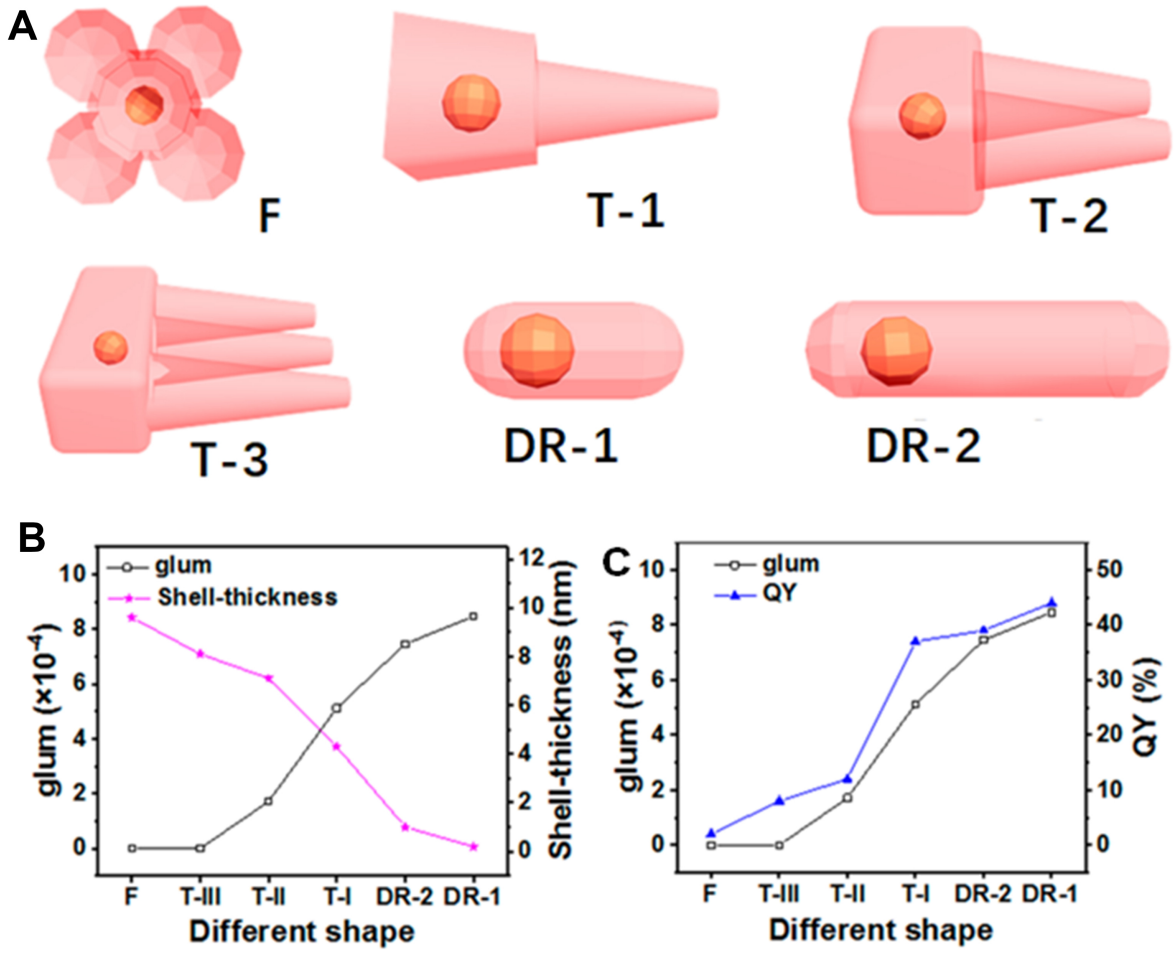

Figure 7. (A) Schematic anisotropic shapes of CdSe/CdS (gold-colored core: CdSe; orange-color shell: CdS). (B) Dependence of g_{lum} of D-Cys-CdSe/CdS, CdS shell thickness and (C) QY on different shapes. Reproduced with permission from Ref.[27] Copyright (2020) American Chemical Society. QY: Quantum yield.

scale, which can be maintained even up to 900 °C. These SiO_2 nanofibers are used as chiral nanoreactors for the formation of sub-10 nm Eu_2O_3 (or Tb_2O_3) NPs, which are transformed from the Eu^{3+} (or Tb^{3+}) trapped in SiO_2 after heating at 900 °C in air [Figure 8B and C]. Interestingly, the CPL features of NPs are observed around the emission wavelengths of 615 nm (Eu_2O_3) and 545 nm (Tb_2O_3) with a $|g_{lum}|$ of the order of 10^{-3}. However, the excitation wavelength using homemade CPL spectroscopy is 375 nm, which deviates from the optimized excitation wavelength from PL spectra. The influence of the excitation wavelength on the CPL performance was not probed.

In addition to lanthanide oxides, other luminophores are also endowed with CPL after being embedded within these SiO_2 nanofibers [Figure 8D][72]. As a unique luminescent phenomenon, aggregation-induced emission (AIE) has gained ever-increasing attention. Tetraphenylethene (TPE) and its derivatives are representative AIE luminogens (AIEgens) with high quantum yields and ready functionalization. TPE molecules can be easily absorbed onto SiO_2 nanofibers modified with phenyl groups and have already demonstrated AIE-based CPL signals of ~ 476 nm in the aggregated state. When SiO_2 was modified by amine groups, fluorescent carboxylic molecules (5,10,15,20-tetrakis(*P*-carboxyphenyl)porphyrin, 1-

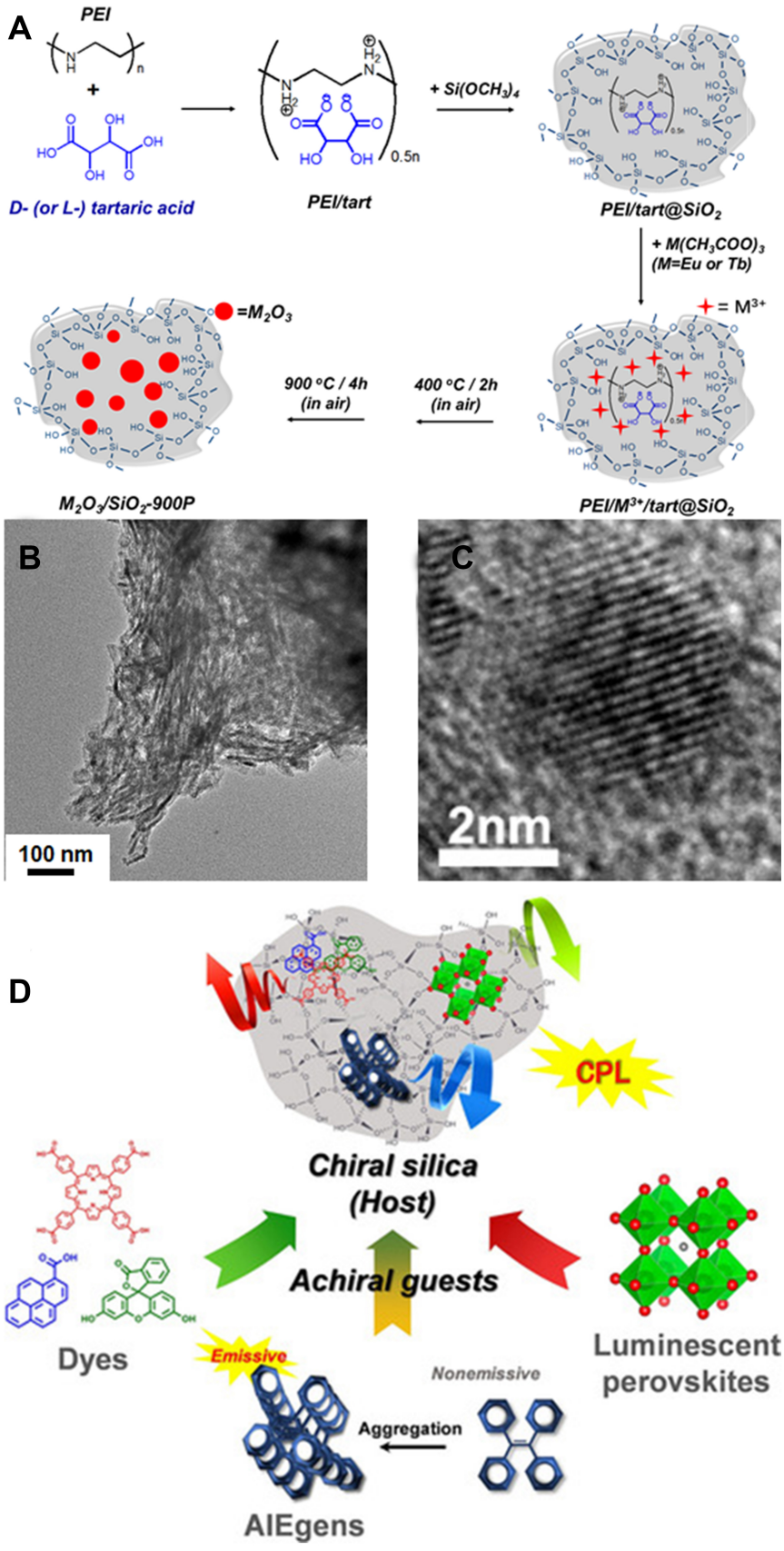
A
PEI
D- (or L-) tartaric acid
PEI/tart
+ Si(OCH3)4
PEI/tart@SiO2
+ M(CH3COO)3
(M=Eu or Tb)
= M3+
PEI/M3+/tart@SiO2
400 °C / 2h
(in air)
900 °C / 4h
(in air)
=M2O3
M2O3/SiO2-900P
B
100 nm
C
2nm
D
CPL
Chiral silica
(Host)
Achiral guests
Dyes
Luminescent
perovskites
Emissive
Nonemissive
Aggregation
AIEgens

Figure 8. (A) Schematic of chiral SiO_2 nanofiber synthesis using PEI/D-tart (or PEI/L-tart) as chiral catalytic templates and their usage to prepare chiral lanthanide oxide (M_2O_3) NPs. (B) TEM image of Tb_2O_3/D-SiO_2 nanofibers. (C) TEM image of an individual Tb_2O_3 nanoparticle on Tb_2O_3/D-SiO_2 nanofibers. Reproduced with permission from Ref.[71]. Copyright (2018) John Wiley and Sons. (D) Various CPL-active systems using chiral silica as hosts to incorporate organic fluorescent dyes, AIEgens and perovskites NCs. Reproduced with permission from Ref.[72]. Copyright (2020) John Wiley and Sons. CPL: Circularly polarized luminescence.

pyrenecarboxyl acid and fluorescein) were attached to SiO_2 and then showed CPL signals at their characteristic emission bands with a $|g_{lum}|$ of 2-5×10^{-3}. In addition, these amine-modified SiO_2 materials could work as chiral reactors for the *in-situ* formation of perovskite NCs with CPL activity. These results imply the significant potential of chiral SiO_2 in designing CPL-related materials.

Harada *et al.*[70] found that cationic gemini surfactants of C_2H_4-1,2-$[(CH_3)_2N^+C_{16}H_{33}]_2$ self-assemble into helical structures in the presence of L- or D-tartrate counter ions. Using these organic helices as templates (dented by 16-2-16 L-tartrate or 6-2-16 D-tartrate), elegant right- and left-handed SiO_2 nanohelices could be prepared and further used as chiral hosts to synthesize lanthanide ion- and perovskite-containing CPL systems [Figure 9A]. After the absorption of Tb^{3+} onto SiO_2 nanohelices and calcination at 900 °C for 4 h in air, the small amount of Tb^{3+} (~ 0.31%) can display CPL outputs at ~ 545 nm (irradiated at 230 nm) with a $|g_{lum}|$ of ~ 10^{-3} due to the helical-morphological chirality of SiO_2. The chiroptical activity may be due to the 4f orbitals of Tb^{3+} being chirally distorted by the asymmetrically arranged Si-O framework. In addition, after modifying the surfaces of SiO_2 helices with amine by 3-aminopropyl-triethoxysilane, perovskite $CsPbBr_3$ nanocrystals (PNCs) are grafted onto SiO_2[73]. When suspended in toluene, PNC-SiO_2 do not exhibit CD and CPL signals. In contrast, after casting the above suspension on quartz and drying, the PNC-SiO_2 in a dried film state became both CD and CPL active. The maximum CPL signals locate at 517.5 nm (under a 360 nm excitation) and the $|g_{lum}|$ reaches 5.7-6.9×10^{-3}. It was found that PNCs are closely packed and helically arranged around SiO_2 helices during the solvent evaporation process, which facilitated the dipolar interaction between the PNCs and then produced CPL.

The synthesis of the CPL-active materials above occurs via a two-step process, which requires the synthesis of SiO_2 in advance. In fact, the luminescent components could also be one-step incorporated into a siloxane framework during the condensation of silica sources (e.g., tetraethyl orthosilicate and multisilylated organic molecules). For example, Cai *et al.*[74] designed TPE-containing bis(triethoxysilane) (BTSTPE) as the silica precursor and then prepared TPE-bridged polybissilsesquioxane (TPE-silica) nanotubes with single-handed helicity using the self-assemblies of a pair of chiral cationic low-molecular-weight gelators (L-ValPyBr and D-ValPyBr) as templates [Figure 9B]. Strikingly, the TPE-silica products showed high thermal stability with only a 5% weight loss at ~ 500 °C. The helical TPE-silica powders emit green light at ~ 500 nm with a quantum yield of over 21%, which is higher than that of its precursor of BTSTPE. The CPL outputs are found at 500 nm with a $|g_{lum}|$ of 0.6-1.6×10^{-3}. In another work, Zhang *et al.*[75] reported AIEgen-silica helical nanotubes displaying CPL signals at 453 nm with a g_{lum} up to 0.02 [under a 366 nm excitation, Figure 9C]. The CPL-active products were obtained by the co-assembly from 2-[4-(1,2,2-triphenylethenyl)-phenoxy]-acetic acid (as the luminophore), N-trimethoxysilylpropyl-N,N,N-trimethylammonium chloride (as a co-structure directing agent) and tetraethylorthosilicate (as a silica precursor).

Other chiral inorganic hosts

As discussed above, there are 22 chiral space groups in crystal structures, providing the possibility of generating intrinsically chiral crystalline materials. For example, the space groups of $TbPO_4·H_2O$ crystals belong to the chiral group of $P3_121$ or its enantiomorph $P3_221$. Hananel *et al.*[26] employed tartaric acid enantiomers as chirality inducers to produce chiral $TbPO_4·H_2O$ doped with Eu^{3+}. Under a 365 nm excitation, Eu^{3+} in the $TbPO_4·H_2O$ host showed strong CPL signals between 590 and 720 nm corresponding to the $^0D_5$→

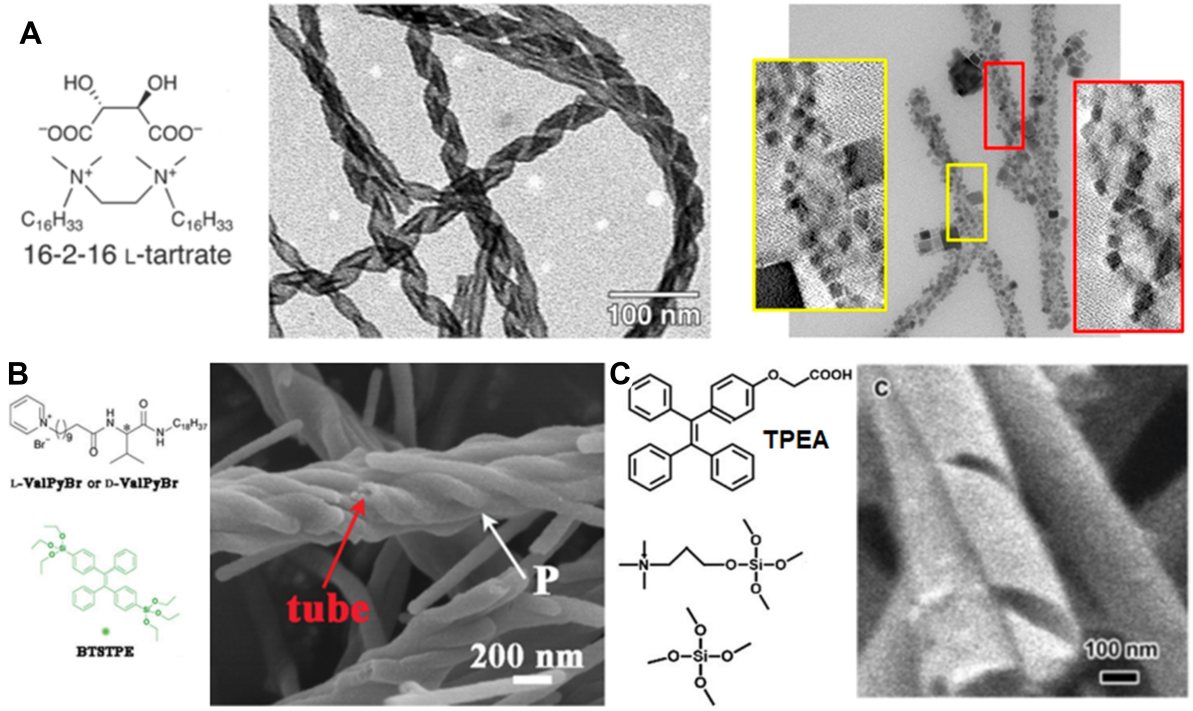

Figure 9. (A) Molecular structure of 16-2-16 L-tartrate (left) and TEM images of L-SiO_2:Tb^{3+} calcined at 900 °C (middle) and nanohelices@PNCs in a dried film and the cross sections (yellow and red frames) obtained with 3D tomography reconstructions (right). Reproduced with permission from Ref.[70]. Copyright (2021) Royal Society of Chemistry. Reproduced with permission from Ref.[73]. Copyright (2020) American Chemical Society. (B) SEM image of TPES-P. Reproduced with permission from Ref. [74]. Copyright (2019) Royal Society of Chemistry. (C) SEM image of L-CASN. Reproduced with permission from Ref.[75]. Copyright (2019) Royal Society of Chemistry. TPES-P: TPE-silica with plus helice. L-CASN: left-handed chiral lamellar mesostructured AIEgen-silica hybrid hollow nanotubes;

^7F_J transitions of Eu^{3+}. The g_{lum} could be 0.06 at 612 nm and is comparable with many chiral Eu(III) complexes. In this work, CPL spectroscopy is also used as a tool to study the symmetry breaking behavior of chiral $TbPO_4 \cdot H_2O$ crystals controlled by the enantiomeric excess (e.e.) of tartaric acid.

Unlike the case above where the symmetry breaking is regulated by chiral molecules, Zhang *et al.*[76] found that oleyamine-coated GdOOH nanowires with a diameter of less than 1 nm could randomly transform into macroscopic left- and right-handed helical assemblies (MHAs) at the centimeter level by an evaporation-induced self-assembly process without the assistance of a chiral dopant [Figure 10A,B][76]. The spontaneous formation of helices is a result of an energy-minimizing process and the handedness is uncontrollable. Fortunately, the left- and right-handed helices can be observed by the naked eye and easily separated. Achiral fluorescent molecule guests of DACT and TMD embedded into MHAs showed CPL signals at their emission bands at 500 and 625 nm, respectively.

SELECTED SPECIAL CPL-ACTIVE SYSTEMS

Many luminophores show down-conversion fluorescence with emission bands in the visible range. In fact, there are other luminescent processes, including up-conversion PL, phosphorescence, thermally activated delayed fluorescence (TADF) and NIR emission. Studies of the CPL related to these processes could enrich our understanding of the origin of CPL and help us to explore more CPL-related applications. Therefore, some special CPL-active systems are presented in this section.

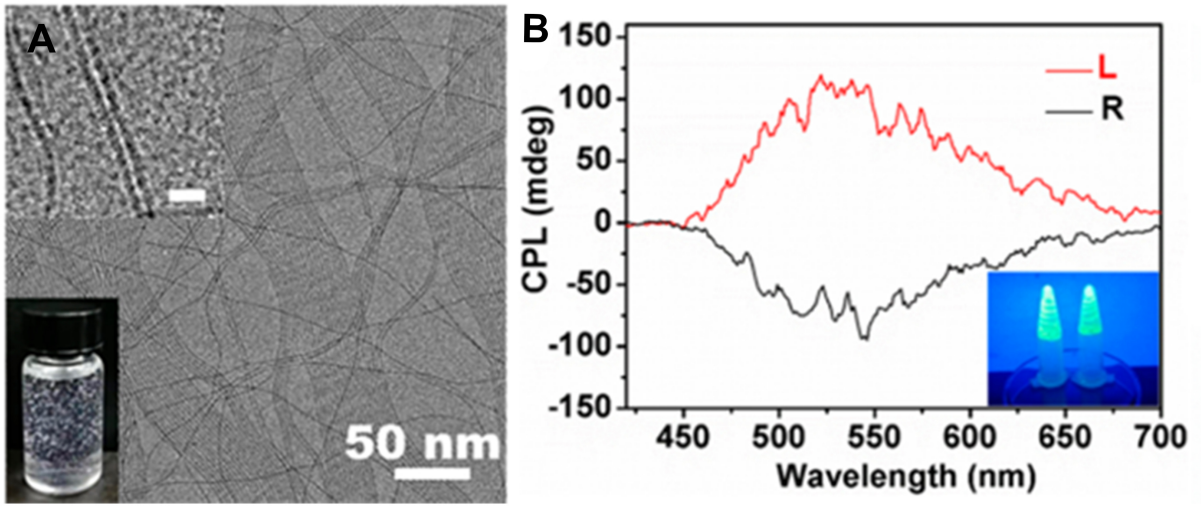

Figure 10. (A) Cryo-electron microscopy image and its large-magnification version (upper inset) of the sub-1 nm GdOOH nanowires (bottom: a photograph of the dispersion of nanowires). (B) CPL spectra of DACT-MHA. Reproduced with permission from Ref.[76]. Copyright (2020) American Chemical Society. CPL: Circularly polarized luminescence; MHA: macroscopically spiral assemblies.

Up-conversion CPL

Up-conversion luminescence is capable of converting long-wavelength NIR light to shorter-wavelength narrow and sharp emission ranging from UV, to visible and even to shorter NIR light. Up-conversion luminescence is utilized widely in a broad range of areas, especially in biological and biomedical ones, due to low background fluorescence, weak photodamage, good penetration in tissues and high sensitivity.

Lanthanide ions (e.g., Yb^{3+}, Er^{3+} and Tm^{3+}) doped in fluoride-based matrixes (e.g., $NaYF_4$ and $NaGdF_4$) possess high up-conversion efficiencies because of sufficient metastable energy and excited states with a long lifetime. Yang *et al.*[77] offered a dexterous solution for an up-conversion CPL based on a radiative energy transfer process from $NaYF_4$:Yb/Tm Upconverting nanoparticles (UCNPs) to $CsPbBr_3$ perovskite nanocrystals (PKNCs) in the chiral nematic liquid crystal (N*LC) featured with PBG [Figure 11A]. A high $|g_{lum}|$ is possible in a PBG structure due to strong handedness-selective reflection of CP light. However, the light loss may occur and the emission of emitters is boosted when the emission wavelength is located at the edge of the photonic bandgap, while the emission is suppressed at the center of the bandgap. Therefore, it is a challenge to achieve both a large g_{lum} and high emission efficiency. To address this issue, an achiral nematic liquid crystal SLC1717 and chiral dopant R-(or S-)811 were used to form left- or right-handed helical N*LC, where two different emitters of $NaYF_4$:Yb/Tm and $CsPbBr_3$ were embedded. Under a 980 nm excitation, $NaYF_4$:Yb/Tm UCNPs showed emission bands at 450 and 475 nm near the edge of the bandgap of N*LC and these emissions were thus enhanced and the g_{lum} at 475 nm was 0.3. The emission of PKNCs was centered at 495 nm, which overlaps with the center of the bandgap. Fortunately, the emission of PKNCs could be enhanced via a radiative energy transfer with quenching the emission of $NaYF_4$:Yb/Tm at 475 nm. Meanwhile, a very high g_{lum} of 1.1 was still achieved for PKNCs at 495 nm.

NIR emission CPL

The emission at the NIR range from luminophores is highly beneficial to optical applications in transparent biological windows because of the suppressed absorption or scattering from skin and blood. However, there is a lack of suitable, reliable detection instruments for weak NIR emission and reports on NIR-CPL are scarce. Yb^{3+} is a typical NIR emitter in the range of 900–1050 nm. The complex of $Yb(TTA)_3$ (TTA = 2-thenoyltrifluoroacetonate) shows relatively good quantum yields due to the antenna effect of TTA ligands.

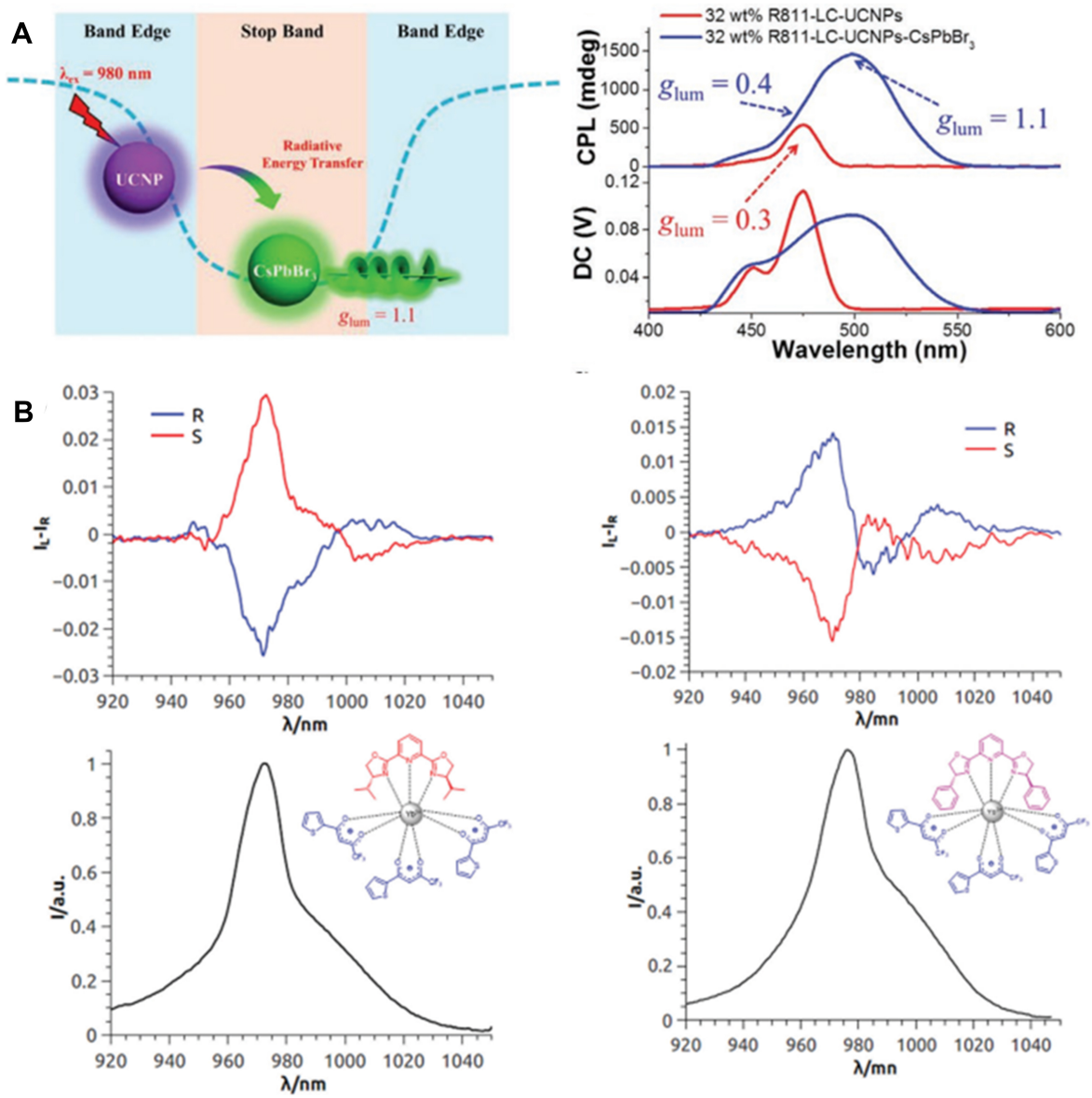

Figure 11. (A) Schematic representation of RET process from UCNPs to $CsPbBr_3$ PKNCs in N*LC (the emissions of $CsPbBr_3$ PKNCs and UCNPs were located at the center and the edge of the photonic bandgap, respectively, left) and UC-CPL spectra of $CsPbBr_3$ PKNCs/UCNPs in N*LC with di erent incident power of a 980 nm laser (right). Reproduced with permission from Ref.[77]. Copyright (2020) John Wiley and Sons. (B) NIR-CPL spectra (top) of both the enantiomers of $Yb(TTA)_3{}^{i}PrPybox$ (left) and $Yb(TTA)_3PhPybox$ (right) and total NIR emission (bottom). Reproduced with permission from Ref.[78]. Copyright (2019) Royal Society of Chemistry. RET: Radiative energy transfer; PKNCs: perovskite nanocrystals; UCNP: upconverting nanoparticles; TTA: 2-thenoyltrifluoroacetonate.

On the basis of $Yb(TTA)_3$, Zinna *et al.*[78] introduced additional chiral ligands ($^{i}PrPyBox$ or PhPyBox) to synthesize two groups of chiral $Yb(TTA)_3{}^{i}PrPyBox$ and $Yb(TTA)_3PhPyBox$ complexes [Figure 11B]. To measure the NIR-CPL of these complexes, the authors conducted modifications on spectrofluoropolarimeter apparatus using an Ag-O-Cs photomultiplier tube as the detector and a photoelastic modulator coupled with an uncoated Glan–Thompson polarizer for polarization discrimination. For $Yb(TTA)_3{}^{i}PrPyBox$, relatively sharp peaks at 972 nm ($^2F_{5/2} \rightarrow {}^2F_{7/2}$ transition of Yb^{3+}) appeared on their CPL spectra appeared with a g_{lum} of -0.025 and +0.029 for (R,R) and (S,S) enantiomers,

respectively. Similar results were also found for $Yb(TTA)_3PhPyBox$ enantiomers.

Thermally activated delayed fluorescence CPL

In principle, TADF enables an internal quantum efficiency of 100% by harvesting triplet (T1) excitons, which is fulfilled through the reverse intersystem crossing from the triplet (T1) to singlet (S1) state in a thermally activated process. Therefore, TADF has received widespread attention, especially in organic light-emitting diode displays. Recently, TADF-based CPL has also gained increasing interest in organic molecules[79]. In contrast, TADF-CPL in inorganic emitters is rare. Han *et al.*[80] synthesized octahedral Ag(I) clusters using chiral ligands named as L/D and PL/PD enantiomers [structures shown in Figure 12A]. In the case of PL/PD, Ag_6 cores in the Ag clusters of Ag_6PL_6 and Ag_6PD_6 are distorted and deviate from the regular octahedral Ag6 skeleton, and these clusters crystallize in the chiral monoclinic space group $P2_1$. Based on chiroptical spectra and DFT simulations, the chiroptical activity of the clusters is mainly attributed to the asymmetric Ag_6 core and the chiral interface between Ag and the coordinated C and N atoms. The PLQY of Ag_6PL_6/Ag_6PD_6 surpasses 95% at room temperature, which is a result of TADF confirmed by the temperature-dependent luminescence spectra and decays. Finally, these clusters display TADF-based CPL signals at 575 nm (excited at 370 nm) with a g_{lum} of ~ 4×10^{-3}.

Phosphorescence CPL

As for the origin of photoluminescence, phosphorescence is an important complementary mechanism to fluorescence. Phosphorescence is the emission from triplet-excited states and its lifetime is longer than fluorescence. Therefore, phosphorescence is appealing in optical sensors, information security, optoelectronic devices and biomedical agents.

Phosphorescence can be observed in lanthanide and Cr ions at room temperature. As demonstrated in Figure 12B Hao *et al.*[81] reported a simple method to obtain colorful CPL-active inorganic persistent lanthanide-based phosphor materials with a long afterglow, including a yellow-green $SrAl_2O_4$:Eu,Dy, purple $CaAl_2O_4$:Eu,Nd, blue-green $Sr_4Al_4O_{25}$:Eu,Dy, sky blue $Sr_2MgSi_2O_7$ and red Y_2O_2S:Eu,Mg,Ti. These commercial phosphor powders are mixed with D- (or L-) cysteine (Cys) in ethanol and subjected to ball-milling for several hours and then the D-/L-Cys-modified phosphors are collected. Using this simple process, these phosphors became CPL-active with a $|g_{lum}|$ of 10^{-3}-10^{-2}, of which a maximum value was observed in the $CaAl_2O_4$:Eu,Nd sample (2.10×10^{-2}). The CD and CPL activity of these inorganic phosphors was induced by chiral Cys molecules, which were absorbed *via* metal-sulfur bonds.

Compared with lanthanides ions, the observation of room-temperature phosphorescence on other luminescent materials is not straightforward. Xu *et al.*[52] demonstrated a three-component system with both fluorescence- and phosphorescence-based CPL of carbon dots (CDs) at room temperature [Figure 12C]. Cellulose nanocrystals are used to form chiral photonic films, in which poly(vinyl alcohol) (PVA) and luminescent CDs are integrated by a co-assembly process. Because of the PBG effect, CPL was observed when the fluorescence wavelength (460 nm, excited by 365 nm) of the CDs located within the bandgap. The employment of PVA seemed to restrict molecular motions and inhibit oxygen quenching to maintain triplet excitons, thus leading to phosphorescence afterglow (480-500 nm) lasting for 2 s, even after turning off the UV (260 nm) irradiation. However, there is an overlap between the fluorescence spectrum (with a peak located at 450-470 nm) and the room-temperature phosphorescence (RTP) spectrum (with a peak at 480-500 nm). In other words, the fluorescence bands are close to the RTP bands. Therefore, it is difficult to differentiate FL-based CPL from RTP-induced CPL on the as-used JASCO CPL-200 spectrophotometer. These authors designed an analytical device [shown in Figure 12C, middle] to measure circular polarized room-temperature phosphorescence (CPRTP), which is fulfilled by combining a fluorospectrophotometer and an L- (or R-) circularly polarized filter (CPF). The CPF was covered on the detector at the

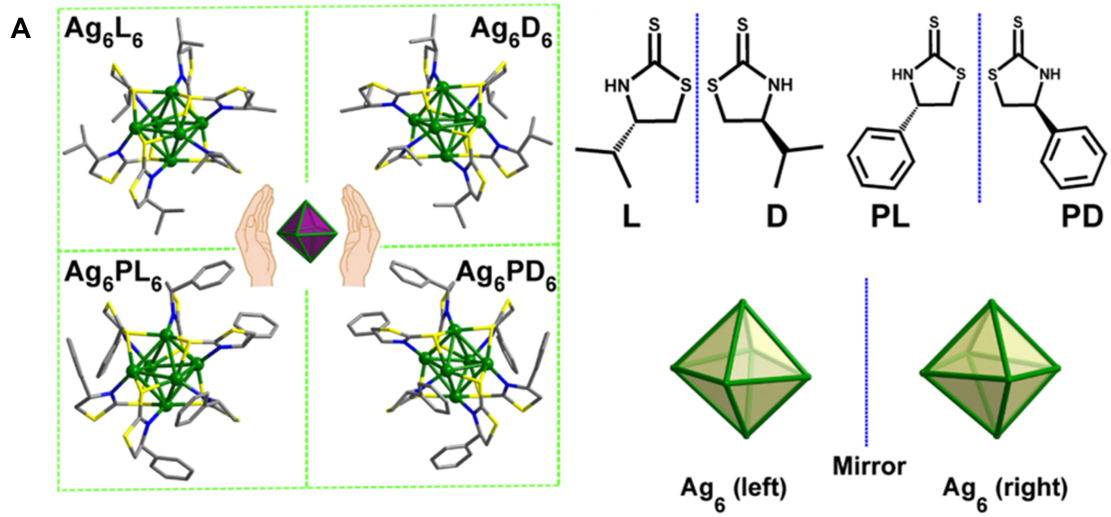
A
Ag_6L_6
Ag_6D_6
Ag_6PL_6
Ag_6PD_6
L
D
PL
PD
Ag_6 (left)
Mirror
Ag_6 (right)

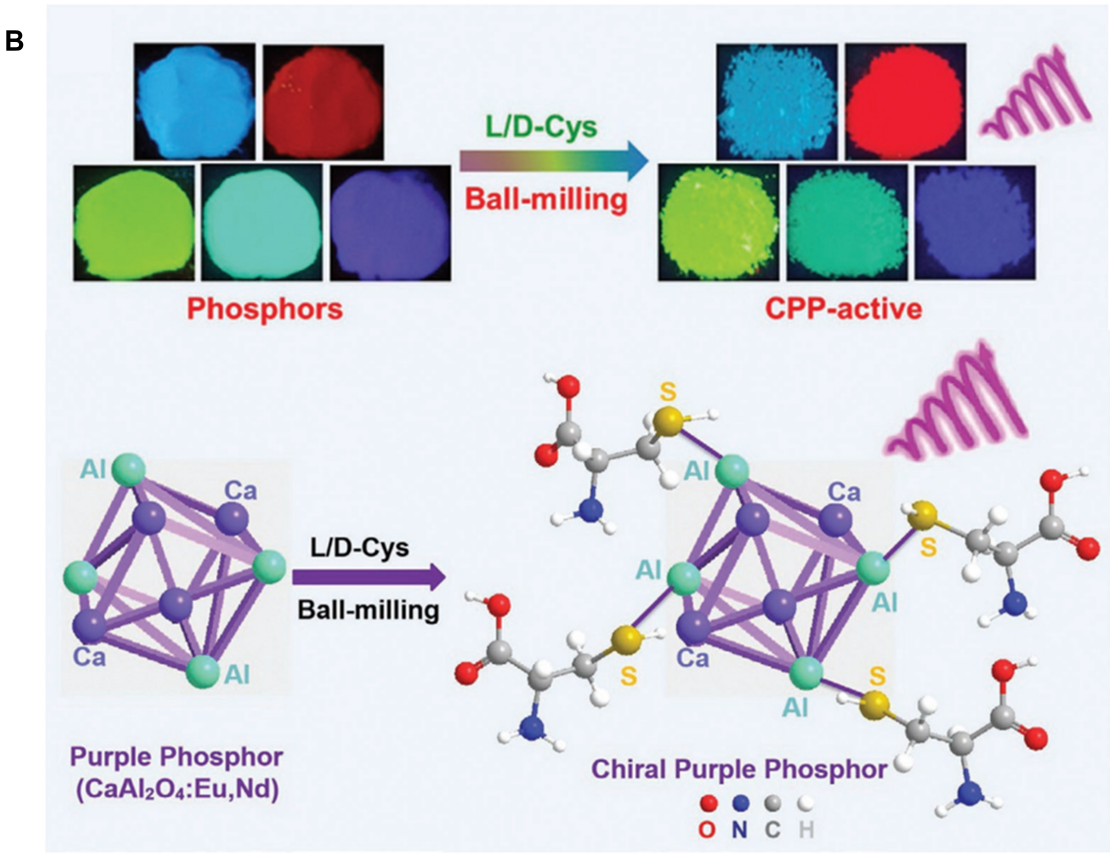
B
L/D-Cys
Ball-milling
Phosphors
CPP-active
Al
Ca
L/D-Cys
Ball-milling
Purple Phosphor
($CaAl_2O_4$:Eu,Nd)
Chiral Purple Phosphor
O N C H

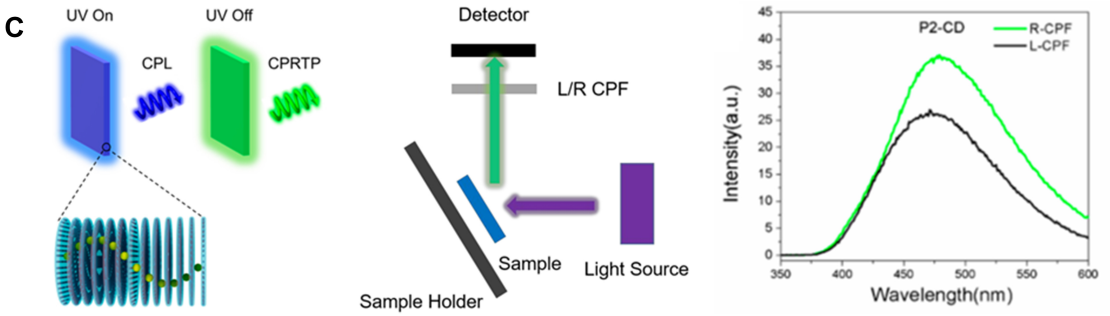
C
UV On
UV Off
CPL
CPRTP
Detector
L/R CPF
Sample
Light Source
Sample Holder
P2-CD
R-CPF
L-CPF
Intensity(a.u.)
Wavelength(nm)

Figure 12. (A) Structures of Ag_6L_6/D_6 and Ag_6PL_6/PD_6 enantiomers, L/D, PL/PD and octahedral Ag_6 framework in Ag_6L_6/D_6. Reproduced with permission from Ref.[80]. (B) Images of various lanthanide-containing phosphor materials before and after modification with L/D-Cys via ball milling (top) and schematic of $CaAl_2O_4$:Eu,Nd phosphor attached by chiral Cys molecules on the surface and the induction of the phosphorescence-based CPL (bottom). Reproduced with permission from Ref.[81]. Copyright (2021) John Wiley and Sons. (C) Schematic of hybrid chiral photonic showing dual CPL and CPRTP (left), an experimental setup for the measurement of CPRTP (middle) and phosphorescence emission spectra of hybrid chiral photonic films recorded with an L-CPF or R-CPF (right). Reproduced with permission from Ref.[52]. Copyright (2020) American Chemical Society. CPL: Circularly polarized luminescence; CPRTP: circular polarized room-temperature phosphorescence; CPF: circularly polarized filter.

phosphorescence measurement mode to record the CPRTP spectra. In principle, L-CPRTP would be blocked by the RCPF, while R-CPRTP would be blocked by the LCPF. On this basis, it was found that the CPRTP intensity recorded with LCPF was weaker than RCPF. By borrowing the definition of g_{lum}, a so-called g_{RTP} is defined as $g_{RTP} = [2\times(I_L-I_R)]/(I_L+I_R)$, where I_L and I_R are the intensity of RTP recorded under LCPF and RCPF, respectively. The highest absolute value of g_{RTP} could reach 0.461.

APPLICATIONS OF INORGANIC-ASSOCIATED CPL

With success in the synthesis of various inorganic-associated CPL-active systems, their potential applications are also explored. Here, we list several examples related to sensors, security, electroluminescent devices, optical storage and asymmetric synthesis.

Sensors

Fluorescence sensing is an important analysis technique with many merits, such as rapidness, sensitivity, nondestructiveness and the ability to obtain diverse information regarding molecular interactions and microenvironments. Since fluorescence is a prerequisite for CPL, the change in fluorescent properties leads to the variation of CPL signals. Therefore, the principles of fluorescence sensing may be borrowed to design CPL sensors. For example, Suo *et al.*[82] reported a AuAg bimetallic cluster-based CPL sensing method by virtue of the fluorescence quenching effect [Figure 13A]. In the presence of metal ions (Sr^{2+} and K^+), guanosine 5′-monophosphate can self-assemble into left- or right-handed helical nanofibers (g-fibers) with a width of 200 nm and a length of several micrometers. These g-fibers are used as chiral hosts to embed AuAg clusters stabilized with adenosine 5′-monophosphate. Consequently, helical nanostructured g-fiber-AuAg composites were obtained and showed CPL at ~ 475 nm under a 356 nm excitation, with a $|g_{lum}|$ of 1-3×10^{-2}. Because of the fluorescence quenching of AuAg NCs by L-Cys, g-fiber-AuAg NCs could be used as CPL sensors for the selective detection of L-Cys (in the range of 0.1 to 8 μmol L^{-1}) with a limit of detection down to 95.7 nM, which is comparable to other common fluorometric and electrochemical methods.

Anticounterfeiting

Luminescent nanomaterials are widely employed in anticounterfeiting applications. To improve the security level, it is highly desirable that a luminescent material can possess more features. CPL-active materials encode hidden chiral fingerprint information into luminescence, which is not easily decoded by common optical read-out instruments. As a result, CPL offers a novel advanced anticounterfeiting technique with high expertise in chirality.

Kitagawa *et al.*[83] firstly synthesized europium complexes with chiral (+/-)-3-(trifluoroacetyl)camphor (+/-tfc) ligands and then cast them on a glass substrate together with the achiral glass promoter tris(2,6-dimethoxyphenyl)phosphine oxide (tmpo) ligand [Figure 13B]. After solvent evaporation, two enantiomeric Eu(+tfc)-tmpo(2) and Eu (–tfc)-tmpo(2) transparent films with an extra-large $|g_{lum}|$ of 1.2 at a 594 nm emission (the magnetic dipole transition $^5D_0 \rightarrow {}^7F_1$ of Eu^{3+}) were produced. Furthermore, the authors demonstrated a CP light-based security device model to visualize the CPL image by a camera equipped with a linear polarizer, a rotatable λ/4 plate and a bandpass filter (594 nm). Eu(+tfc)-tmpo(2) was cast into a sun

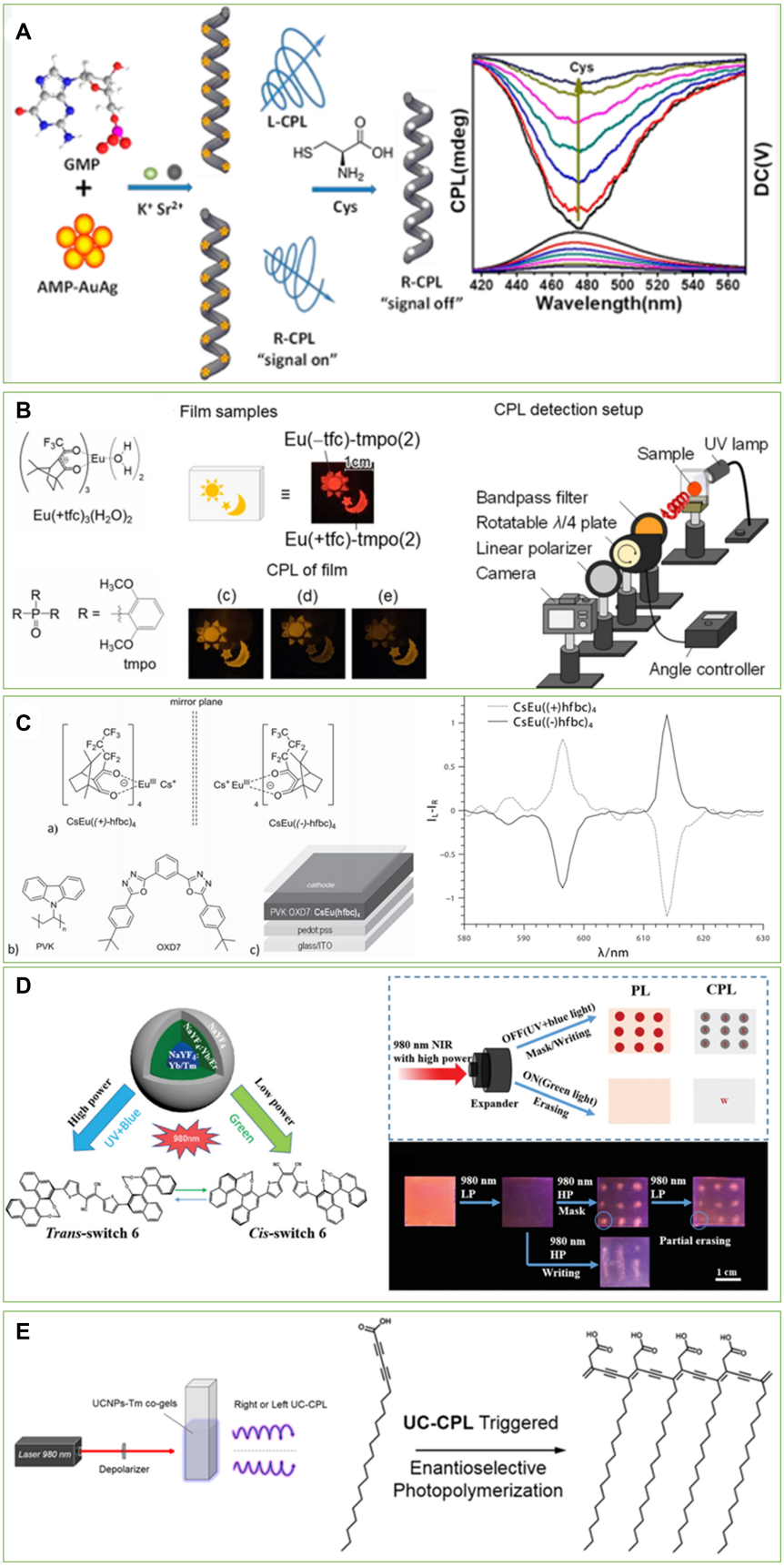
A
GMP
AMP-AuAg
K+ Sr2+
L-CPL
Cys
R-CPL
"signal off"
R-CPL
"signal on"
CPL(mdeg)
DC(V)
Wavelength(nm)
B
Film samples
Eu(+tfc)3(H2O)2
Eu(−tfc)-tmpo(2)
Eu(+tfc)-tmpo(2)
tmpo
CPL of film
CPL detection setup
Sample
UV lamp
Bandpass filter
Rotatable λ/4 plate
Linear polarizer
Camera
Angle controller
C
mirror plane
CsEu((+)-hfbc)4
CsEu((-)-hfbc)4
PVK
OXD7
cathode
pedot:pss
glass/ITO
λ/nm
D
High power
UV+Blue
Low power
Green
980nm
Trans-switch 6
Cis-switch 6
980 nm NIR with high power
Expander
OFF(UV+blue light)
Mask/Writing
ON(Green light)
Erasing
PL
CPL
980 nm LP
980 nm HP
Mask
Writing
Partial erasing
1 cm
E
UCNPs-Tm co-gels
Laser 980 nm
Depolarizer
Right or Left UC-CPL
UC-CPL Triggered
Enantioselective
Photopolymerization

Figure 13. Applications of inorganic-associated CPL-active systems. (A) CPL sensors of Cys. Reproduced with permission from Ref.[82]. Copyright (2020) American Chemical Society. (B) A security paint based on CPL-active Eu(III) lumino-glass. Reproduced with permission from Ref.[83]. (C) Electroluminescent device architecture containing chiral Eu(III) complexes and their circularly polarized electroluminescence (CPEL) spectra. Reproduced with permission from Ref.[84]. Copyright (2015) John Wiley and Sons. (D) Conceptual description of illuminating PL/CPL dual-mode rewritable optical storage and real images of PL/CPL dual-mode patterns. Reproduced with permission from Ref. [87]. Copyright (2020) Royal Society of Chemistry. (E) Schematic of enantioselective photopolymerization setup of HA. Reproduced with permission from Ref.[88]. Copyright (2019) American Chemical Society. PL: Photoluminescence; CPL: circularly polarized luminescenc.

pattern and Eu(–tfc)-tmpo(2) into a moon. Without the λ/4 plate, both the sun and moon are observed. By rotating the λ/4 plate 90° clockwise or anticlockwise using an angle controller, the photographs of the emission using L-CP light ("sun") and R-CP light ("moon"), respectively, are exhibited.

Electroluminescent devices

Electroluminescent devices, where an emissive layer is sandwiched between an anode and a cathode, are promising for artificial light sources. In these devices, the charge carriers (electrons and holes) are generated at the electrodes under an external voltage, transported to and then recombined at the emissive layer to produce electroluminescence. Various luminescent materials are used as the emissive layers to construct electroluminescent devices, such as organic, CD-based and perovskite-based light emitting diodes. Furthermore, these devices, which are capable of directly emitting CP light, are of significant interest for their promising potential in displays with high-resolution, 3D imaging ability, improved brightness and lower energy consumption.

Zinna *et al.*[84] used chiral europium complexes of $CsEu(hfbc)_4$ (hfbc = 3-heptafluoro-butylyrylcamphorate) with the highest available g_{lum} (g_{lum} = 1.38 at 595 nm) as circularly polarized emitters in electroluminescent devices [Figure 13C]. To reduce the emission from the matrix, the Eu(III) complexes were blended with a polyvinylcarbazole host and a soluble additive of 1,3-bis[2-(4-tert-butylphenyl)-1,3,4-oxadiazo-5-yl]benzene to form the emitting layer. To minimize the internal reflection of the emitted light on the back electrode, a Ba/Al cathode (50% transmittance at 612 nm) was employed. With these strategies, a good polarization degree of emission (as measured by the dissymmetry factor of g_{EL} in electroluminescence) is achieved, with g_{EL} values of ±0.75 and –0.09/+0.15 for the Eu $^5D_0 \rightarrow {}^7F_1$ (at 595 nm) and Eu $^5D_0 \rightarrow {}^7F_2$ transitions (at 612 nm), respectively. Furthermore, by optimizing the emissive layer formulations and fine-tuning the architectures of the devices, the absolute value of g_{EL} could even be increased to 1.0 (for Eu $^5D_0 \rightarrow {}^7F_1$ at 595 nm)[85].

Han *et al.*[86] reported two enantiomeric gold clusters $(Au_4L_4)_n/(Au_4D_4)_n$ consisting of a Au_4 core and a chiral ligand, (S)-/(R)-4-isopropylthiazolidine-2-thione [abbreviated as L and D, structures shown in Figure 12A]. Through an aggregation- and crystallization-induced emission process, these aggregated gold nanoclusters showed a strong green emission centered at 507 nm with a photoluminescence quantum yield of 41.4% and intense CPL signals with $|g_{lum}|$ of 7.0×10^{-3}. These nanoclusters were employed as the chiral emissive layer to fabricate electroluminescent devices. The as-obtained device exhibited obvious green CPEL signals (driven at a voltage of 10 V) with a maximum external quantum efficiency of 1.5% and a dissymmetry factor ($|g_{EL}|$) of $4\text{-}7\times10^{-3}$.

Optical storage

The usage of CP light for optical storage is attractive due to the orthogonal characteristics of the polarization and uncomplicated optical system structures. Juan *et al.*[87] proposed an optical storage model based on 980 nm NIR-light triggered reversible CPL switching. A cholesteric liquid crystal with a self-organized helical superstructure was used as the host to load lanthanide (Yb^{3+}, Er^{3+} or Tm^{3+})-doped $NaYF_4$-based UCNPs and a chiral fluorescent photoswitch of **6** [Figure 13D]. When the UCNPs are irradiated by 980 nm at a low

power (980-l), the 520 nm green emission ($Yb^{3+} \rightarrow Er^{3+}$ energy transfer process) dominated, while the 365 and 450 nm emissions ($Yb^{3+} \rightarrow Tm^{3+}$ energy transfer process) appeared at a high laser power density (980 h). Switch **6** showed a *trans* to *cis* photoisomerization under 520 nm light and the reverse isomerization upon irradiation at 365 or 450 nm. A strong emission peak at ~ 580 nm appeared for the *trans* state of switch **6** and greatly decreased for the *cis* state. Correspondingly, both the CPL signal and its absolute g_{lum} of ~ 580 nm decreased with low-power 980 nm NIR light, while partly recovering when exposed to high-power 980 nm light. Based on this switchable process controlled by laser power, a PL/CPL-encryption dual-mode rewritable optical storage device can be designed. The fluorescent dot array can be written on the cell using a photomask with a high-power laser and the information is erased under a low-power mode.

Asymmetric synthesis

CP light-induced asymmetric photochemical synthesis is an important type of absolute synthesis and even accounts for the homochirality origin on earth. Because of the unbalance between L- and R-CP emissions, CPL-active emitters are potential CP light sources to initiate enantioselective synthesis. Jin *et al.*[88] showed an up-conversion CPL to trigger the enantioselective polymerization of diacetylene [Figure 13E]. Achiral lanthanide-doped UCNPs ($NaYF_4$:Yb/Er or $NaYF_4$:Yb/Tm) were co-assembled with chiral lipid gelator L-/D-GAm to create helical nanotubes. After excitation with a 980 nm laser, the emission peaks of UCNPs-Tm are mainly located at 360 nm ($^1D_2 \rightarrow {}^3H_6$ transition), 476 nm ($^1G_4 \rightarrow {}^3H_6$) and 802 nm ($^3H_4 \rightarrow {}^3H_6$). Interestingly, the UV part of CPL from UCNPs-Tm could induce the polymerization of 2,4-heneicosadiynoic acid into polydiacetylene (PDA). PDA formed using L-GAm/UCNPs-Tm showed positive CD signals, while negative CD signals were found with D-GAm/UCNPs-Tm. Therefore, the molecular chirality of the gelator controlled the handedness of the UC-CPL from lanthanide ions and then subsequently regulated the enantioselective polymerization of diacetylene.

SUMMARY AND OUTLOOK

After a survey of the recent literature, it is without doubt that we have a toolbox to engineer multiple inorganic species (lanthanide ions, metal clusters, semiconductor NPs, carbon dots, perovskite NCs, nano-silica and so on) to undergo CPL, although they are not supposed to be chiral from our common sense. CPL in these inorganic materials is also found in various luminescence processes (e.g., up-conversion, TADF, phosphorescence and NIR emission) and is useful for many applications in sensing, optical storage, security and asymmetric synthesis. Because CPL is related to both chirality and luminescence, the achievements above prompt us to believe that two enantiomeric forms are allowed both in the structures and luminescence of inorganic substances and will open up new chirality-related horizons in inorganic chemistry and light science.

However, there are still many issues to be addressed to comprehend CPL in inorganics, including:

Reliable CPL data free from artifacts: CPL measurements are traditionally conducted on various homemade instruments and have recently been performed on some commercial CPL spectrophotometers. However, there are some artifacts possibly existing in as-measured CPL signals, which can be caused by many factors (e.g., instrumental limitations, linear dichroism effect and scattering/absorption phenomena). In particular, solid-state or anisotropic samples should be treated carefully. To this end, some experimental guides and data analysis methods can be found to obtain true CPL signals[89-93]. In addition, it is encouraging to give CD/PL spectra and some experimental details (e.g., sample concentrations and spectral test parameters) together with CPL data. It will be helpful to check the reliability and reproducibility of CPL signals.

Enhancement of g_{lum}: As shown in Table 1, the g_{lum} values of many kinds of inorganic-associated CPL are ~ 10^{-3} or lower, although some metal ions (e.g., lanthanide and chromium(III)) can potentially present high g_{lum} due to magnetically allowed but electric-dipole forbidden emissions. The small g_{lum} value means that the differences between LCP and RCP only account for 0.3% of the total emission. Hence, there is a significant potential to increase g_{lum}. Some enhancement strategies have been proposed, which are fulfilled by ingenious molecular design, energy transfer processes, plasmonic metal-assisted enhancement and assembly-/aggregation-induced CPL[19,94-97].

Evaluation indexes for CPL: Basically, CPL is based on luminescence and therefore the indexes for luminescence, such as quantum yield, brightness, excitation and emission wavelengths, should be taken into consideration together with g_{lum}. For example, Eu complexes showed a highest g_{lum} of 1.38 but with a very low emission quantum yield of less than 1.0%, which restricts their applications, especially in displays. The choice of excitation wavelength is also important in improving the CPL performance in some luminescent systems involved with energy transfer (e.g., metal complexes). Moreover, the relationships between g_{lum} and the luminescence parameters above are underexplored. Some researchers have suggested several indexes, such as a figure of merit (FM) (FM = $\Phi \times g_{lum}$, where Φ is the emission efficiency), asymmetric quantum efficiency (φ_a) ($\varphi_a = I_L/I_0$ or I_R/I_0, where I_0 is the incident light intensity) and a brightness indicator (BF) ($B_{CPL} = \varepsilon_\lambda \times \Phi \times g_{lum}/2$, where ε_λ is the molar coefficient measured at the excitation wavelength)[21,98,99]. Nevertheless, the application of the indexes above is underexplored for different purposes.

Multiple-component CPL-active systems: In many cases, the system is constructed as a binary-component mode, i.e., only one chiral entity and only a luminescent one. However, it is not easy to achieve an ideal CPL effect (e.g., high g_{lum}, strong emission and tunable emission bands) only by two components. Consequently, multiple components can be introduced to manipulate the optical and chiral properties.

Revealing the detailed mechanisms for CPL: Although we know how to synthesize CPL-active materials, the underlying mechanism is not well explained in many publications. Often, the chirality transfer/induction mechanisms proposed for CD activity are roughly extended to CPL activity, but it is unsuitable in some cases because CD and CPL belong to two different transition processes. In addition, the theories and simulation methods addressing luminescence in a chiral environment are currently inadequate.

Exploration of CPL-based applications: The applications described here are still in their infancy but are inspirational nonetheless. With success in materials synthesis, exploration of their real applications is an important follow-up work.

DECLARATIONS

Authors' contributions

Prepared and corrected the manuscript: Liu X, Jin RH

Availability of data and materials

Not applicable.

Financial support and sponsorship

The research was supported in part by the JSPS KAKENHI, grant number: JP16H06515 (Coordination Asymmetry) and by the JSPS KAKEHI Grantin-Aid for Scientific Research (B), 19H02767.

Conflicts of interest

Both authors declared that there are no conflicts of interest.

Ethical approval and consent to participate

Not applicable.

Consent for publication

Not applicable.

Copyright

REFERENCES

1. Guijarro A, Yus M. The origin of chirality in the molecules of life: a revision from awareness to the current theories and perspectives of this unsolved problem. Cambridge: Royal Society of Chemistry; 2009. DOI
2. Carreira EM, Yamamoto H. Comprehensive chirality. Elsevier: London; 2012. Available from: https://www.elsevier.com/books/comprehensive-chirality/yamamoto/978-0-08-095167-6. [Last accessed on 17 Mar 2022].
3. Stanciu CD, Hansteen F, Kimel AV, et al. All-optical magnetic recording with circularly polarized light. *Phys Rev Lett* 2007;99:047601. DOI PubMed
4. Kim S, Kim E. Performance analysis of stereoscopic three-dimensional projection display systems. *3D Res* 2010;1:1-16. DOI
5. Kunnen B, Macdonald C, Doronin A, Jacques S, Eccles M, Meglinski I. Application of circularly polarized light for non-invasive diagnosis of cancerous tissues and turbid tissue-like scattering media. *J Biophotonics* 2015;8:317-23. DOI PubMed
6. Krupová M, Kapitán J, Bouř P. Induced lanthanide circularly polarized luminescence as a probe of protein fibrils. *ACS Omega* 2019;4:1265-71. DOI PubMed PMC
7. Yang G, Zhang S, Hu J, Fujiki M, Zou G. The chirality induction and modulation of polymers by circularly polarized light. *Symmetry* 2019;11:474. DOI
8. Qu A, Sun M, Kim JY, et al. Stimulation of neural stem cell differentiation by circularly polarized light transduced by chiral nanoassemblies. *Nat Biomed Eng* 2021;5:103-13. DOI PubMed
9. Nishizawa N, Munekata H. Lateral-type spin-photonics devices: development and applications. *Micromachines (Basel)* 2021;12:644. DOI PubMed PMC
10. Zhan X, Xu FF, Zhou Z, Yan Y, Yao J, Zhao YS. 3D laser displays based on circularly polarized lasing from cholesteric liquid crystal arrays. *Adv Mater* 2021;33:e2104418. DOI PubMed
11. Jiang S, Xiong X, Hu Y, et al. High-efficiency generation of circularly polarized light via symmetry-induced anomalous reflection. *Phys Rev B* 2015:91. DOI
12. Zinna F, Pescitelli G, Di Bari L. Circularly polarized light at the mirror: caveats and opportunities. *Chirality* 2020;32:765-9. DOI PubMed
13. Ranjbar B, Gill P. Circular dichroism techniques: biomolecular and nanostructural analyses- a review. *Chem Biol Drug Des* 2009;74:101-20. DOI PubMed
14. MacKenzie LE, Pålsson LO, Parker D, Beeby A, Pal R. Rapid time-resolved circular polarization luminescence (CPL) emission spectroscopy. *Nat Commun* 2020;11:1676. DOI PubMed PMC
15. Riehl JP, Muller G. Circularly Polarized Luminescence Spectroscopy and Emission-Detected Circular Dichroism. In: Berova N, Polavarapu PL, Nakanishi K, Woody RW, editors. Comprehensive Chiroptical Spectroscopy. John Wiley & Sons, Inc.; 2011. p.65-90. DOI
16. Sánchez-Carnerero EM, Agarrabeitia AR, Moreno F, et al. circularly polarized luminescence from simple organic molecules. *Chemistry* 2015;21:13488-500. DOI PubMed PMC
17. Ma JL, Peng Q, Zhao CH. Circularly polarized luminescence switching in small organic molecules. *Chemistry* 2019;25:15441-54. DOI PubMed
18. Nitti A, Pasini D. Aggregation-induced circularly polarized luminescence: chiral organic materials for emerging optical technologies. *Adv Mater* 2020;32:e1908021. DOI PubMed
19. Sang Y, Han J, Zhao T, Duan P, Liu M. Circularly polarized luminescence in nanoassemblies: generation, amplification, and application. *Adv Mater* 2020;32:e1900110. DOI PubMed
20. Zhang DW, Li M, Chen CF. Recent advances in circularly polarized electroluminescence based on organic light-emitting diodes. *Chem Soc Rev* 2020;49:1331-43. DOI PubMed
21. Deng Y, Wang M, Zhuang Y, Liu S, Huang W, Zhao Q. Circularly polarized luminescence from organic micro-/nano-structures. *Light Sci Appl* 2021;10:76. DOI PubMed PMC
22. Gong Z, Zhu X, Zhou Z, et al. Frontiers in circularly polarized luminescence: molecular design, self-assembly, nanomaterials, and

applications. *Sci China Chem* 2021;64:2060-104. DOI
23. Jiang S, Kotov NA. Circular polarized light emission in chiral inorganic nanomaterials. *Adv Mater* 2022:e2108431. DOI PubMed
24. Sun M, Xu L, Qu A, et al. Site-selective photoinduced cleavage and profiling of DNA by chiral semiconductor nanoparticles. *Nat Chem* 2018;10:821-30. DOI PubMed
25. Vinegrad E, Hananel U, Markovich G, Cheshnovsky O. Determination of handedness in a single chiral nanocrystal via circularly polarized luminescence. *ACS Nano* 2019;13:601-8. DOI PubMed
26. Hananel U, Ben-Moshe A, Diamant H, Markovich G. Spontaneous and directed symmetry breaking in the formation of chiral nanocrystals. *Proc Natl Acad Sci U S A* 2019;116:11159-64. DOI PubMed PMC
27. Hao J, Li Y, Miao J, et al. Ligand-induced chirality in asymmetric CdSe/CdS nanostructures: a close look at chiral tadpoles. *ACS Nano* 2020;14:10346-58. DOI PubMed
28. Krishnadas KR, Sementa L, Medves M, et al. Chiral functionalization of an atomically precise noble metal cluster: insights into the origin of chirality and photoluminescence. *ACS Nano* 2020;14:9687-700. DOI PubMed
29. Ben-Moshe A, Govorov AO, Markovich G. Enantioselective synthesis of intrinsically chiral mercury sulfide nanocrystals. *Angew Chem Int Ed Engl* 2013;52:1275-9. DOI PubMed
30. Morrow SM, Bissette AJ, Fletcher SP. Transmission of chirality through space and across length scales. *Nat Nanotechnol* 2017;12:410-9. DOI PubMed
31. Kim H, Im SW, Kim RM, et al. Chirality control of inorganic materials and metals by peptides or amino acids. *Mater Adv* 2020;1:512-24. DOI
32. Dryzun C, Mastai Y, Shvalb A, Avnir D. Chiral silicate zeolites. *J Mater Chem* 2009;19:2062. DOI
33. Riehl JP, Richardson FS. Circularly polarized luminescence spectroscopy. *Chem Rev* 1986;86:1-16. DOI
34. Moran DM, Metcalf DH, Richardson FS. Chiroptical luminescence spectra of uranyl ion in cubic sodium tris(acetato)dioxouranate(1-) crystals. *Inorg Chem* 1992;31:819-25. DOI
35. Mukhina MV, Maslov VG, Baranov AV, et al. Intrinsic chirality of CdSe/ZnS quantum dots and quantum rods. *Nano Lett* 2015;15:2844-51. DOI PubMed
36. Duan Y, Han L, Zhang J, et al. Optically active nanostructured ZnO films. *Angew Chem Int Ed Engl* 2015;54:15170-5. DOI PubMed
37. Flack H. Chiral and achiral crystal structures. *HCA* ;86:905-21. DOI PubMed
38. Gautier R, Klingsporn JM, Van Duyne RP, Poeppelmeier KR. Optical activity from racemates. *Nat Mater* 2016;15:591-2. DOI PubMed
39. Zhao J, Zhang T, Dong XY, et al. Circularly polarized luminescence from achiral single crystals of hybrid manganese halides. *J Am Chem Soc* 2019;141:15755-60. DOI PubMed
40. Kumar J, Thomas KG, Liz-Marzán LM. Nanoscale chirality in metal and semiconductor nanoparticles. *Chem Commun (Camb)* 2016;52:12555-69. DOI PubMed PMC
41. Tohgha U, Deol KK, Porter AG, et al. Ligand induced circular dichroism and circularly polarized luminescence in CdSe quantum dots. *ACS Nano* 2013;7:11094-102. DOI PubMed PMC
42. Maoz BM, Chaikin Y, Tesler AB, et al. Amplification of chiroptical activity of chiral biomolecules by surface plasmons. *Nano Lett* 2013;13:1203-9. DOI PubMed
43. Ben-Moshe A, Maoz BM, Govorov AO, Markovich G. Chirality and chiroptical effects in inorganic nanocrystal systems with plasmon and exciton resonances. *Chem Soc Rev* 2013;42:7028-41. DOI PubMed
44. Cao Z, Gao H, Qiu M, et al. Chirality transfer from sub-nanometer biochemical molecules to sub-micrometer plasmonic metastructures: physiochemical mechanisms, biosensing, and bioimaging opportunities. *Adv Mater* 2020;32:e1907151. DOI PubMed
45. Lunkley JL, Shirotani D, Yamanari K, Kaizaki S, Muller G. Extraordinary circularly polarized luminescence activity exhibited by cesium tetrakis(3-heptafluoro-butylryl-(+)-camphorato) Eu(III) complexes in EtOH and CHCl3 solutions. *J Am Chem Soc* 2008;130:13814-5. DOI
46. Wong H, Lo W, Yim K, Law G. Chirality and chiroptics of lanthanide molecular and supramolecular assemblies. *Chem* 2019;5:3058-95. DOI
47. Staszak K, Wieszczycka K, Marturano V, Tylkowski B. Lanthanides complexes – Chiral sensing of biomolecules. *Coordination Chemistry Reviews* 2019;397:76-90. DOI
48. Mackenzie LE, Pal R. Circularly polarized lanthanide luminescence for advanced security inks. *Nat Rev Chem* 2021;5:109-24. DOI
49. Jiménez JR, Poncet M, Míguez-Lago S, et al. Bright long-lived circularly polarized luminescence in chiral chromium(III) complexes. *Angew Chem Int Ed Engl* 2021;60:10095-102. DOI PubMed
50. Poncet M, Benchohra A, Jiménez J, Piguet C. Chiral chromium(III) complexes as promising candidates for circularly polarized luminescence. *ChemPhotoChem* 2021;5:880-92. DOI
51. Ru Y, Ai L, Jia T, et al. Recent advances in chiral carbonized polymer dots: From synthesis and properties to applications. *Nano Today* 2020;34:100953. DOI
52. Xu M, Wu X, Yang Y, et al. Designing hybrid chiral photonic films with circularly polarized room-temperature phosphorescence. *ACS Nano* 2020;14:11130-9. DOI PubMed
53. Chekini M, Prince E, Zhao L, Mundoor H, Smalyukh II, Kumacheva E. Chiral carbon dots synthesized on cellulose nanocrystals. *Adv Optical Mater* 2020;8:1901911. DOI
54. Li A, Zheng D, Zhang M, Wu B, Zhu L. Chirality transfer in carbon dot-composited Sol-gel systems for excitation-dependent

circularly polarized luminescence. *Langmuir* 2020;36:8965-70. DOI PubMed

55. Ru Y, Sui L, Song H, et al. Rational design of multicolor-emitting chiral carbonized polymer dots for full-color and white circularly polarized luminescence. *Angew Chem Int Ed Engl* 2021;60:14091-9. DOI PubMed
56. Zhang M, Li K, Zang S. Progress in atomically precise coinage metal clusters with aggregation-induced emission and circularly polarized luminescence. *Adv Optical Mater* 2020;8:1902152. DOI
57. Wu H, He X, Yang B, Li CC, Zhao L. Assembly-induced strong circularly polarized luminescence of spirocyclic chiral silver(I) clusters. *Angew Chem Int Ed Engl* 2021;60:1535-9. DOI PubMed
58. Zhang MM, Dong XY, Wang ZY, et al. AIe triggers the circularly polarized luminescence of atomically precise enantiomeric copper(I) Alkynyl Clusters. *Angew Chem Int Ed Engl* 2020;59:10052-8. DOI PubMed
59. Shi L, Zhu L, Guo J, et al. Self-assembly of chiral gold clusters into crystalline nanocubes of exceptional optical activity. *Angew Chem Int Ed Engl* 2017;56:15397-401. DOI PubMed
60. Tao J, Li B, Lu Z, et al. Endowing zeolite lta superballs with the ability to manipulate light in multiple ways. *Angew Chem Int Ed Engl* 2020;59:19684-90. DOI PubMed
61. Bobrovsky A, Mochalov K, Oleinikov V, et al. Optically and electrically controlled circularly polarized emission from cholesteric liquid crystal materials doped with semiconductor quantum dots. *Adv Mater* 2012;24:6216-22. DOI PubMed
62. Yan J, Ota F, San Jose BA, Akagi K. Chiroptical resolution and thermal switching of chirality in conjugated polymer luminescence via selective reflection using a double-layered cell of chiral nematic liquid crystal. *Adv Funct Mater* 2017;27:1604529. DOI
63. Wang C, Chen K, Xu P, Yeung F, Kwok H, Li G. Fully chiral light emission from Cspbx $_3$ perovskite nanocrystals enabled by cholesteric superstructure stacks. *Adv Funct Mater* 2019;29:1903155. DOI
64. Cheng J, Hao J, Liu H, et al. Optically active CdSe-Dot/CdS-Rod nanocrystals with induced chirality and circularly polarized luminescence. *ACS Nano* 2018;12:5341-50. DOI PubMed
65. Dong Y, Zhang Y, Li X, Feng Y, Zhang H, Xu J. Chiral perovskites: promising materials toward next-generation optoelectronics. *Small* 2019;15:e1902237. DOI PubMed
66. Long G, Sabatini R, Saidaminov MI, et al. Chiral-perovskite optoelectronics. *Nat Rev Mater* 2020;5:423-39. DOI
67. Ma S, Ahn J, Moon J. Chiral perovskites for next-generation photonics: from chirality transfer to chiroptical activity. *Adv Mater* 2021;33:e2005760. DOI PubMed
68. Jin RH. Understanding silica from the viewpoint of asymmetry. *Chemistry* 2019;25:6270-83. DOI PubMed
69. Matsukizono H, Jin RH. High-temperature-resistant chiral silica generated on chiral crystalline templates at neutral pH and ambient conditions. *Angew Chem Int Ed Engl* 2012;51:5862-5. DOI PubMed
70. Harada T, Yanagita H, Ryu N, et al. Lanthanide ion-doped silica nanohelix: a helical inorganic network acts as a chiral source for metal ions. *Chem Commun (Camb)* 2021;57:4392-5. DOI PubMed
71. Sugimoto M, Liu XL, Tsunega S, et al. Circularly polarized luminescence from inorganic materials: encapsulating guest lanthanide oxides in chiral silica hosts. *Chemistry* 2018;24:6519-24. DOI PubMed
72. Tsunega S, Jin RH, Nakashima T, Kawai T. Transfer of chiral information from silica hosts to achiral luminescent guests: a simple approach to accessing circularly polarized luminescent systems. *Chempluschem* 2020;85:619-26. DOI PubMed
73. Liu P, Chen W, Okazaki Y, et al. Optically active perovskite Cspbbr$_3$ nanocrystals helically arranged on inorganic silica nanohelices. *Nano Lett* 2020;20:8453-60. DOI PubMed
74. Cai X, Du J, Zhang L, et al. Circularly polarized luminescence of single-handed helical tetraphenylethylene-silica nanotubes. *Chem Commun (Camb)* 2019;55:12176-9. DOI PubMed
75. Zhang W, Chang H, Ai J, Che S, Duan Y, Han L. Spontaneous chiral self-assembly of achiral AIEgens into AIEgen-silica hybrid nanotubes. *Chem Commun (Camb)* 2019;55:14438-41. DOI PubMed
76. Zhang S, Shi W, Rong S, Li S, Zhuang J, Wang X. Chirality evolution from Sub-1 nanometer nanowires to the macroscopic helical structure. *J Am Chem Soc* 2020;142:1375-81. DOI PubMed
77. Yang X, Zhou M, Wang Y, Duan P. Electric-field-regulated energy transfer in chiral liquid crystals for enhancing upconverted circularly polarized luminescence through steering the photonic bandgap. *Adv Mater* 2020;32:e2000820. DOI PubMed
78. Zinna F, Arrico L, Di Bari L. Near-infrared circularly polarized luminescence from chiral Yb(iii)-diketonates. *Chem Commun (Camb)* 2019;55:6607-9. DOI PubMed
79. Frédéric L, Desmarchelier A, Favereau L, Pieters G. Designs and applications of circularly polarized thermally activated delayed fluorescence molecules. *Adv Funct Mater* 2021;31:2010281. DOI
80. Han Z, Dong XY, Luo P, et al. Ultrastable atomically precise chiral silver clusters with more than 95% quantum efficiency. *Sci Adv* 2020;6:eaay0107. DOI PubMed PMC
81. Hao W, Li Y, Liu M. Endowing phosphor materials with long-afterglow circularly polarized phosphorescence via ball milling. *Adv Optical Mater* 2021;9:2100452. DOI
82. Suo Z, Hou X, Chen J, et al. Highly chiroptical detection with gold-silver bimetallic nanoclusters circularly polarized luminescence based on G-quartet nanofiber self-assembly. *J Phys Chem C* 2020;124:21094-102. DOI
83. Kitagawa Y, Wada S, Islam MDJ, et al. Chiral lanthanide lumino-glass for a circularly polarized light security device. *Commun Chem* 2020:3. DOI
84. Zinna F, Giovanella U, Di Bari L. Highly circularly polarized electroluminescence from a chiral europium complex. *Adv Mater* 2015;27:1791-5. DOI PubMed

85. Zinna F, Pasini M, Galeotti F, Botta C, Di Bari L, Giovanella U. Design of Lanthanide-based oleds with remarkable circularly polarized electroluminescence. *Adv Funct Mater* 2017;27:1603719. DOI
86. Han Z, Zhao X, Peng P, et al. Intercluster aurophilicity-driven aggregation lighting circularly polarized luminescence of chiral gold clusters. *Nano Res* 2020;13:3248-52. DOI
87. Juan A, Sun H, Qiao J, Guo J. Near-infrared light-controlled circularly polarized luminescence of self-organized emissive helical superstructures assisted by upconversion nanoparticles. *Chem Commun (Camb)* 2020;56:13649-52. DOI PubMed
88. Jin X, Sang Y, Shi Y, et al. Optically Active Upconverting nanoparticles with induced circularly polarized luminescence and enantioselectively triggered photopolymerization. *ACS Nano* 2019;13:2804-11. DOI PubMed
89. Longhi G, Castiglioni E, Koshoubu J, Mazzeo G, Abbate S. circularly polarized luminescence: a review of experimental and theoretical aspects. *Chirality* 2016;28:696-707. DOI PubMed
90. Chen W, Tian Z, Li Y, Jiang Y, Liu M, Duan P. Long-persistent circularly polarized phosphorescence from chiral organic ionic crystals. *Chemistry* 2018;24:17444-8. DOI PubMed
91. Tanaka H, Inoue Y, Mori T. Circularly polarized luminescence and circular dichroisms in small organic molecules: correlation between excitation and emission dissymmetry factors. *ChemPhotoChem* 2018;2:386-402. DOI
92. Castiglioni E, Abbate S, Lebon F, Longhi G. Ultraviolet, circular dichroism, fluorescence, and circularly polarized luminescence spectra of regioregular poly-[3-((S)-2-methylbutyl)-thiophene] in solution. *Chirality* 2012;24:725-30. DOI PubMed
93. Harada T, Kuroda R, Moriyama H. Solid-state circularly polarized luminescence measurements: theoretical analysis. *Chemical Physics Letters* 2012;530:126-31. DOI
94. Kumar J, Nakashima T, Tsumatori H, Kawai T. Circularly polarized luminescence in chiral aggregates: dependence of morphology on luminescence dissymmetry. *J Phys Chem Lett* 2014;5:316-21. DOI PubMed
95. Zhang C, Li S, Dong X, Zang S. Circularly polarized luminescence of agglomerate emitters. *Aggregate* 2021:2. DOI
96. Zhao S, Yu Y, Zhang B, et al. Metal-Enhanced circularly polarized luminescence of self-assembled Au@SiO_2 triangular nanoprisms and fluorophores in chiral cellulose nanocrystal films. *Adv Optical Mater* 2021;9:2100907. DOI
97. Greenfield JL, Wade J, Brandt JR, Shi X, Penfold TJ, Fuchter MJ. Pathways to increase the dissymmetry in the interaction of chiral light and chiral molecules. *Chem Sci* 2021;12:8589-602. DOI PubMed PMC
98. Yao L, Niu G, Li J, et al. Circularly polarized luminescence from chiral tetranuclear copper(I) iodide clusters. *J Phys Chem Lett* 2020;11:1255-60. DOI PubMed
99. Arrico L, Di Bari L, Zinna F. Quantifying the overall efficiency of circularly polarized emitters. *Chemistry* 2021;27:2920-34. DOI PubMed

Ren-Hua Jin

Ren-Hua Jin graduated from Jilin University (China) in 1982 and completed his PhD at Nankai University (China) in 1987. After that, he joined Beijing University of Chemical Technology as an assistant professor and then transferred to the University of Tokyo as a postdoctoral fellow. He worked at Miyazaki University as an associate professor (1994 ~ 1997). Then, he worked at the Kawamura Institute of Chemical Research as a leader for 14 years and moved to Kanagawa University as a full professor in April 2012. His current research interests lie in the architecture of water-soluble/amphiphilic polymers, the design of ceramic nanomaterials with shape- and/or chirality-control, and their applications in catalysis, separation, optical materials, sensing, etc.

Xinling Liu

Xinling Liu earned his bachelor's degree in chemistry from Ocean University of China in 2008. Then, he obtained his PhD degree in Physical Chemistry at Shanghai Institute of Ceramics, Chinese Academy of Sciences (SICCAS) in 2013. After postdoc research at Shanghai University and Kanagawa University, he joined the College of Chemistry and Materials Science at Shanghai Normal University in 2018 and became an associate professor. His current research interests lie in the synthesis of chiral inorganic nanomaterials and understanding their chiroptical properties (circular dichroism, circularly polarized luminescence), and the applications of Raman spectroscopy in chiral recognition.

AUTHOR INSTRUCTIONS

1. Submission Overview

Before you decide to publish with *Chemical Synthesis*, please read the following items carefully and make sure that you are well aware of Editorial Policies and the following requirements.

1.1 Topic Suitability

The topic of the manuscript must fit the scope of the journal. Please refer to Aims and Scope for more information.

1.2 Open Access and Copyright

The journal adopts Gold Open Access publishing model and distributes content under the Creative Commons Attribution 4.0 International License. Copyright is retained by authors. Please make sure that you are well aware of these policies.

1.3 Publication Fees

Chemical Synthesis is an open access journal. When a paper is accepted for publication, authors are required to pay Article Processing Charges (APCs) to cover its editorial and production costs. The APC for each submission is $600. There are no additional charges based on color, length, figures, or other elements. For more details, please refer to OAE Publication Fees.

1.4 Language Editing

All submissions are required to be presented clearly and cohesively in good English. Authors whose first language is not English are advised to have their manuscripts checked or edited by a native English speaker before submission to ensure the high quality of expression. A well-organized manuscript in good English would make the peer review even the whole editorial handling more smoothly and efficiently.
If needed, authors are recommended to consider the language editing services provided by Charlesworth to ensure that the manuscript is written in correct scientific English before submission. Authors who publish with OAE journals enjoy a special discount for the services of Charlesworth via the following two ways.

Submit your manuscripts directly at http://www.charlesworthauthorservices.com/~OAE;
Open the link http://www.charlesworthauthorservices.com/, and enter Promotion Code “OAE” when you submit.

1.5 Work Funded by the National Institutes of Health

If an accepted manuscript was funded by National Institutes of Health (NIH), the authors may inform Editors of the NIH funding number. The Editors are able to deposit the paper to the NIH Manuscript Submission System on behalf of the authors.

2. Submission Preparation

2.1 Cover Letter

A cover letter is required to be submitted accompanying each manuscript. It should be concise and explain why the study is significant, why it fits the scope of the journal, and why it would be attractive to readers, etc.
Here is a guideline of a cover letter for authors’ consideration:
In the first paragraph: include the title and type (e.g., Original Article, Review, Case Report, etc.) of the manuscript, a brief on the background of the study, the question the author sought out to answer and why;
In the second paragraph: concisely explain what was done, the main findings and why they are significant;
In the third paragraph: indicate why the manuscript fits the Aims and Scope of the journal, and why it would be attractive to readers;
In the fourth paragraph: confirm that the manuscript has not been published elsewhere and not under consideration of any other journal. All authors have approved the manuscript and agreed on its submission to the journal. Journal’s specific requirements have been met if any.
If the manuscript is contributed to a Special Issue, please also mention it in the cover letter.
If the manuscript was presented partly or entirely in a conference, the author should clearly state the background information of the event, including the conference name, time and place in the cover letter.

2.2 Types of Manuscripts

The journal publishes Research Article, Review Article, Short Communication, Feature Article, Commentary, Editorial, News, Research Highlight, Perspective, *etc*. For more details about paper type, please refer to the following table.

Manuscript Type	Definition	Abstract	Keywords	Main Text Structure
Research Article	A Research Article is a seminal and insightful research study and showcases that often involves modern techniques or methodologies. Authors should justify that their work are of novel findings.	The abstract should state briefly the purpose of the research, the principal results and major conclusions. No more than 250 words.	3-6 keywords.	The main content should include four sections: Introduction, Experimental, Results and discussion, and Conclusions.
Review Article	A Review Article should be an authoritative, well balanced and critical survey of recent progresses in an attractive or a fundamental chemical research field.	Unstructured abstract. No more than 250 words.	3-6 keywords.	The main text may consist of several sections with unfixed section titles. We suggest that the author include an "Introduction" section at the beginning, several sections with unfixed titles in the middle part, and a "Conclusion and outlook" section in the end. Corresponding authors are requested to provide a short biography (up to 200 words) and headshot for inclusion at the end of the published article.
Short Communication	Short Communications are for the urgent publication of a research which is of outstanding significance and interest to experts in the field and also to general chemistry readership. Authors should write in a clear and concise way to demonstrate the necessity of an urgent publication.	Unstructured abstract. No more than 150 words.	3-6 keywords.	The short Communication is a one body text with maximum 4 items (figures and tables) and 12 references.
Feature Article	A Feature Article is not a typical review. Feature article should highlight the author's contribution to a key field with a balanced discussion of related work from the field. A Feature Article should not, in principle, contain original research.	Unstructured abstract. No more than 250 words.	3-6 keywords.	The main text may consist of several sections with unfixed section titles. We suggest that the author include an "Introduction" section at the beginning, several sections with unfixed titles in the middle part, and a "Conclusion and outlook" section in the end.
Commentary	A Commentary is to provide comments on a newly published article or an alternative viewpoint on a certain topic.	Unstructured abstract. No more than 250 words.	3-6 keywords.	/
Editorial	An Editorial can be a comment about an important event in the world related or not to chemistry or a particular discovery in chemistry, needing a particular attention of chemistry community.	None required.	None required	/
News	A News comments an important event in the world related or not to chemistry, or a particular discovery in chemistry, needing a particular attention of chemistry community.	None required.	None required	/
Research Highlight	A Research Highlight article is peer-reviewed paper and highlights work recently published in the journal or in a recent issue of another journal.	None required.	3-6 keywords.	/
Perspective	A Perspective provides personal points of view on the state-of-the-art of a specific area of knowledge and its future prospects.	Unstructured abstract. No more than 150 words.	3-6 keywords.	/

2.3 Manuscript Structure

2.3.1 Front Matter

2.3.1.1 Title

The title of the manuscript should be concise, specific and relevant, with no more than 16 words if possible. When gene or protein names are included, the abbreviated name rather than full name should be used.

2.3.1.2 Authors and Affiliations

Authors' full names should be listed. The initials of middle names can be provided. Institutional addresses and email addresses for all authors should be listed. At least one author should be designated as corresponding author. In addition, corresponding authors are suggested to provide their Open Researcher and Contributor ID upon submission. Please note that any change to authorship is not allowed after manuscript acceptance.

2.3.1.3 Highlights

Highlights are mandatory because they can help increase the discoverability of your article through search engines. They consist of a short collection of bullet points that capture the novel results of your research as well as new methods that were used during the study (if any). They should be submitted in a separate editable file in the online submission system. Please use 'Highlights' in the file name and include 3 to 5 bullet points (maximum 85 characters per bullet point, including spaces).

2.3.1.4 Abstract

The abstract should be a single paragraph with word limitation and specific structure requirements (for more details please refer to Types of Manuscripts). It usually describes the main objective(s) of the study, explains how the study was done, including any model organisms used, without methodological detail, and summarizes the most important results and their significance. The abstract must be an objective representation of the study: it is not allowed to contain results which are not presented and substantiated in the manuscript, or exaggerate the main conclusions. Citations should not be included in the abstract.

2.3.1.5 Graphical Abstract

The graphical abstract is essential as this can catch first view of your publication by readers. We recommend you to submit an eye-catching figure. It should summarize the content of the article in a concise graphical form. It is recommended to use it because this can make online articles get more attention. The graphic abstract should be submitted as a separate document in the online submission system. Please provide an image with a minimum of 531 × 1,328 pixels (h × w) or proportionally more. The image should be readable at a size of 5 × 13 cm using a regular screen resolution of 96 dpi. Preferred file types: tiff, psd, AI, jpeg and eps files.

2.3.1.6 Keywords

Three to six keywords should be provided, which are specific to the article, yet reasonably common within the subject discipline.

2.3.2 Main Text

Manuscripts of different types are structured with different sections of content. Please refer to Types of Manuscripts to make sure which sections should be included in the manuscripts.

2.3.2.1 Introduction

The introduction should contain background that puts the manuscript into context, allow readers to understand why the study is important, include a brief review of key literature, and conclude with a brief statement of the overall aim of the work and a comment about whether that aim was achieved. Relevant controversies or disagreements in the field should be introduced as well.

2.3.2.2 Experimental

Experimental should contain sufficient details to allow others to fully replicate the study. New methods and protocols should be described in detail while well-established methods can be briefly described or appropriately cited. Experimental participants selected, the drugs and chemicals used, the statistical methods taken, and the computer software used should be identified precisely. Statistical terms, abbreviations, and all symbols used should be defined clearly. Protocol documents for clinical trials, observational studies, and other non-laboratory investigations may be uploaded as supplementary materials.

2.3.2.3 Results and Discussion

This section should contain the findings of the study and discuss the implications of the findings in context of existing research and highlight limitations of the study. Future research directions may also be mentioned. Results of statistical analysis should also be included either as text or as tables or figures if appropriate. Authors should emphasize and summarize only the most important observations. Data on all primary and secondary outcomes identified in the section Methods should also be provided. Extra or supplementary materials and technical details can be placed in supplementary documents.

2.3.2.4 Conclusions

It should state clearly the main conclusions and include the explanation of their relevance or importance to the field.

2.3.3 Back Matter

2.3.3.1 Acknowledgments

Anyone who contributed towards the article but does not meet the criteria for authorship, including those who provided professional writing services or materials, should be acknowledged. Authors should obtain permission to acknowledge from all those mentioned in the Acknowledgments section. This section is not added if the author does not have anyone to acknowledge.

2.3.3.2 Authors' Contributions

Each author is expected to have made substantial contributions to the conception or design of the work, or the acquisition, analysis, or interpretation of data, or the creation of new software used in the work, or have drafted the work or substantively revised it.

Please use Surname and Initial of Forename to refer to an author's contribution. For example: made substantial contributions to conception and design of the study and performed data analysis and interpretation: Salas H, Castaneda WV; performed data acquisition, as well as provided administrative, technical, and material support: Castillo N, Young V.

If an article is single-authored, please include "The author contributed solely to the article." in this section.

2.3.3.3 Availability of Data and Materials

In order to maintain the integrity, transparency and reproducibility of research records, authors should include this section in their manuscripts, detailing where the data supporting their findings can be found. Data can be deposited into data repositories or published as supplementary information in the journal. Authors who cannot share their data should state that the data will not be shared and explain it. If a manuscript does not involve such issue, please state "Not applicable." in this section.

2.3.3.4 Financial Support and Sponsorship

All sources of funding for the study reported should be declared. The role of the funding body in the experiment design, collection, analysis and interpretation of data, and writing of the manuscript should be declared. Any relevant grant numbers and the link of funder's website should be provided if any. If the study is not involved with this issue, state "None." in this section.

2.3.3.5 Conflicts of Interest

Authors must declare any potential conflicts of interest that may be perceived as inappropriately influencing the representation or interpretation of reported research results. If there are no conflicts of interest, please state "All authors declared that there are no conflicts of interest." in this section. Some authors may be bound by confidentiality agreements. In such cases, in place of itemized disclosures, we will require authors to state "All authors declare that they are bound by confidentiality agreements that prevent them from disclosing their conflicts of interest in this work.". If authors are unsure whether conflicts of interest exist, please refer to the "Conflicts of Interest" of *Chemical Synthesis* Editorial Policies for a full explanation.

2.3.3.6 Ethical Approval and Consent to Participate

Research involving human subjects, human material or human data must be performed in accordance with the Declaration of Helsinki and approved by an appropriate ethics committee. An informed consent to participate in the study should also be obtained from participants, or their parents or legal guardians for children under 16. A statement detailing the name of the ethics committee (including the reference number where appropriate) and the informed consent obtained must appear in the manuscripts reporting such research.

Studies involving animals and cell lines must include a statement on ethical approval. More information is available at Editorial Policies.

If the manuscript does not involve such issue, please state "Not applicable." in this section.

2.3.3.7 Consent for Publication

Manuscripts containing individual details, images or videos, must obtain consent for publication from that person, or in the case of children, their parents or legal guardians. If the person has died, consent for publication must be obtained from the next of kin of the participant. Manuscripts must include a statement that a written informed consent for publication was obtained. Authors do not have to submit such content accompanying the manuscript. However, these documents must be available if requested. If the manuscript does not involve this issue, state "Not applicable." in this section.

2.3.3.8 Copyright

Authors retain copyright of their works through a Creative Commons Attribution 4.0 International License that clearly states how readers can copy, distribute, and use their attributed research, free of charge. A declaration "© The Author(s)

2022." will be added to each article. Authors are required to sign License to Publish before formal publication.

2.3.3.9 References

References should be numbered in order of appearance at the end of manuscripts. In the text, reference numbers should be placed in square brackets and the corresponding references are cited thereafter. If the number of authors is less than or equal to six, we require to list all authors' names. If the number of authors is more than six, only the first three authors' names are required to be listed in the references, other authors' names should be omitted and replaced with "et al.". Abbreviations of the journals should be provided on the basis of Index Medicus. Information from manuscripts accepted but not published should be cited in the text as "Unpublished material" with written permission from the source.

References should be described as follows, depending on the types of works:

Types	Examples
Journal articles by individual authors	Weaver DL, Ashikaga T, Krag DN, et al. Effect of occult metastases on survival in node-negative breast cancer. *N Engl J Med* 2011;364:412-21. [PMID: 21247310 DOI: 10.1056/NEJMoa1008108]
Organization as author	Diabetes Prevention Program Research Group. Hypertension, insulin, and proinsulin in participants with impaired glucose tolerance. *Hypertension* 2002;40:679-86. [PMID: 12411462]
Both personal authors and organization as author	Vallancien G, Emberton M, Harving N, van Moorselaar RJ; Alf-One Study Group. Sexual dysfunction in 1,274 European men suffering from lower urinary tract symptoms. *J Urol* 2003;169:2257-61. [PMID: 12771764 DOI: 10.1097/01.ju.0000067940.76090.73]
Journal articles not in English	Zhang X, Xiong H, Ji TY, Zhang YH, Wang Y. Case report of anti-N-methyl-D-aspartate receptor encephalitis in child. *J Appl Clin Pediatr* 2012;27:1903-7. (in Chinese)
Journal articles ahead of print	Odibo AO. Falling stillbirth and neonatal mortality rates in twin gestation: not a reason for complacency. BJOG 2018; Epub ahead of print [PMID: 30461178 DOI: 10.1111/1471-0528.15541]
Books	Sherlock S, Dooley J. Diseases of the liver and billiary system. 9th ed. Oxford: Blackwell Sci Pub; 1993. pp. 258-96.
Book chapters	Meltzer PS, Kallioniemi A, Trent JM. Chromosome alterations in human solid tumors. In: Vogelstein B, Kinzler KW, editors. The genetic basis of human cancer. New York: McGraw-Hill; 2002. pp. 93-113.
Online resource	FDA News Release. FDA approval brings first gene therapy to the United States. Available from: https://www.fda.gov/NewsEvents/Newsroom/PressAnnouncements/ucm574058.htm. [Last accessed on 30 Oct 2017]
Conference proceedings	Harnden P, Joffe JK, Jones WG, editors. Germ cell tumours V. Proceedings of the 5th Germ Cell Tumour Conference; 2001 Sep 13-15; Leeds, UK. New York: Springer; 2002.
Conference paper	Christensen S, Oppacher F. An analysis of Koza's computational effort statistic for genetic programming. In: Foster JA, Lutton E, Miller J, Ryan C, Tettamanzi AG, editors. Genetic programming. EuroGP 2002: Proceedings of the 5th European Conference on Genetic Programming; 2002 Apr 3-5; Kinsdale, Ireland. Berlin: Springer; 2002. pp. 182-91.
Unpublished material	Tian D, Araki H, Stahl E, Bergelson J, Kreitman M. Signature of balancing selection in Arabidopsis. *Proc Natl Acad Sci U S A*. Forthcoming 2002.

For other types of references, please refer to U.S. National Library of Medicine.
The journal also recommends that authors prepare references with a bibliography software package, such as EndNote to avoid typing mistakes and duplicated references.

2.3.3.10 Supplementary Materials

Additional data and information can be uploaded as Supplementary Materials to accompany the manuscripts. The supplementary materials will also be available to the referees as part of the peer-review process. Any file format is acceptable, such as data sheet (word, excel, csv, cdx, fasta, pdf or zip files), presentation (PowerPoint, pdf or zip files), image (cdx, eps, jpeg, pdf, png or tiff), table (word, excel, csv or pdf), audio (mp3, wav or wma) or video (avi, divx, flv, mov, mp4, mpeg, mpg or wmv). All information should be clearly presented. Supplementary materials should be cited in the main text in numeric order (e.g., Supplementary Figure 1, Supplementary Figure 2, Supplementary Table 1, Supplementary Table 2, etc.). The style of supplementary figures or tables complies with the same requirements on figures or tables in main text. Videos and audios should be prepared in English, and limited to a size of 500 MB or a duration of 3 minutes.

2.4 Manuscript Format

2.4.1 File Format

Manuscript files can be in DOC and DOCX formats and should not be locked or protected.

2.4.2 Length

There are no restrictions on paper length, number of figures, or amount of supporting documents. Authors are encouraged to present and discuss their findings concisely.

2.4.3 Language

Manuscripts must be written in English.

2.4.4 Multimedia Files

The journal supports manuscripts with multimedia files. The requirements are listed as follows:
Videos or audio files are only acceptable in English. The presentation and introduction should be easy to understand. The frames should be clear, and the speech speed should be moderate.
A brief overview of the video or audio files should be given in the manuscript text.
The video or audio files should be limited to a size of up to 500 MB.
Please use professional software to produce high-quality video files, to facilitate acceptance and publication along with the submitted article. Upload the videos in mp4, wmv, or rm format (preferably mp4) and audio files in mp3 or wav format.

2.4.5 Figures

Figures should be cited in numeric order (e.g., Figure 1, Figure 2) and placed after the paragraph where it is first cited;
Figures can be submitted in format of tiff, psd, AI or jpeg, with resolution of 300-600 dpi;
Figure caption is placed under the Figure;
Diagrams with describing words (including, flow chart, coordinate diagram, bar chart, line chart, and scatter diagram, *etc.*) should be editable in word, excel or powerpoint format. Non-English information should be avoided;
Labels, numbers, letters, arrows, and symbols in figure should be clear, of uniform size, and contrast with the background;
Symbols, arrows, numbers, or letters used to identify parts of the illustrations must be identified and explained in the legend;
Internal scale (magnification) should be explained and the staining method in photomicrographs should be identified;
All non-standard abbreviations should be explained in the legend;
Permission for use of copyrighted materials from other sources, including re-published, adapted, modified, or partial figures and images from the internet, must be obtained. It is authors' responsibility to acquire the licenses, to follow any citation instruction requested by third-party rights holders, and cover any supplementary charges.

2.4.6 Tables

Tables should be cited in numeric order and placed after the paragraph where it is first cited;
The table caption should be placed above the table and labeled sequentially (e.g., Table 1, Table 2);
Tables should be provided in editable form like DOC or DOCX format (picture is not allowed);
Abbreviations and symbols used in table should be explained in footnote;
Explanatory matter should also be placed in footnotes;
Permission for use of copyrighted materials from other sources, including re-published, adapted, modified, or partial tables from the internet, must be obtained. It is authors' responsibility to acquire the licenses, to follow any citation instruction requested by third-party rights holders, and cover any supplementary charges.

2.4.7 Abbreviations

Abbreviations should be defined upon first appearance in the abstract, main text, and in figure or table captions and used consistently thereafter. Non-standard abbreviations are not allowed unless they appear at least three times in the text. Commonly-used abbreviations, such as DNA, RNA, ATP, *etc*., can be used directly without definition. Abbreviations in titles and keywords should be avoided, except for the ones which are widely used.

2.4.8 Italics

General italic words like *vs*., *et al., etc*., *in vivo*, *in vitro*; *t* test, *F* test, *U* test; related coefficient as *r*, sample number as *n*, and probability as *P*; names of genses; names of bacteria and biology species in Latin.

2.4.9 Units

SI Units should be used. Imperial, US customary and other units should be converted to SI units whenever possible. There is a space between the number and the unit (i.e., 23 mL). Hour, minute, second should be written as h, min, s.

2.4.10 Numbers

Numbers appearing at the beginning of sentences should be expressed in English. When there are two or more numbers in a paragraph, they should be expressed as Arabic numerals; when there is only one number in a paragraph, number < 10 should be expressed in English and number > 10 should be expressed as Arabic numerals. 12345678 should be written as 12,345,678.

2.4.11 Equations

Equations should be editable and not appear in a picture format. Authors are advised to use either the Microsoft Equation Editor or the MathType for display and inline equations.

2.5 Submission Link

Submit an article via https://oaemesas.com/login?JournalId=cs.

www.oaepublish.com

Chemical Synthesis
(*CS*)
Los Angeles Office
245 E Main Street ste122, Alhambra,
CA 91801, USA
E-mail: editorialoffice@chesynjournal.com
Website: www.chesynjournal.com